This is the Pre-Published Version.
This is the peer reviewed version of the following article: Xie, C., Mak, C., Tao, X., & Yan, F. (2017). Photodetectors Based on Two-Dimensional Layered Materials Beyond Graphene. Advanced Functional Materials, 27(19), 1603886, which has been published in final form at https://doi.org/10.1002/adfm.201603886. This article may be used for non-commercial purposes in accordance with Wiley Terms and Conditions for Use of Self-Archived Versions.

Photodetectors Based on Two-Dimensional Layered Materials Beyond Graphene

Chao Xie, Chunhin Mak, Xiaoming Tao, and Feng Yan*

Dr. C. Xie, C. H. Mak, Prof. F. YanDepartment of Applied Physics

The Hong Kong Polytechnic UniversityHong Kong, China

E-mail: apafyan@polyu.edu.hk

Prof. X. M. Tao Institute of Textiles & Clothing

The Hong Kong Polytechnic UniversityHong Kong, China

Abstract

Following a significant number of graphene studies, other two-dimensional (2D) layered materials have attracted more and more interest for their unique structures and distinct physical properties, which has opened a window for realizing novel electronic or optoelectronic devices. Here, we present a comprehensive review on the applications of 2D-layered semiconductors as photodetectors, including photoconductors, phototransistors, and photodiodes, reported in the past five years. The device designs, mechanisms, and performances of the photodetectors are introduced and discussed systematically. Emerging techniques to improve device performances by enhancing light-matter interactions are addressed as well. Finally, we deliver a summary and outlook to provide a guideline of the future development of this rapidly growing field.

1. Introduction

Two-dimensional (2D) layered materials refer to a class of mate- rials artificially derived from layered van der Waals solids,[1,2] in which the atoms are held together by tight covalent or ionic bonds along 2D (in-plane) directions to form atomic layers, while the atomic layers are bonded together by weak van der Waals interactions along the third-dimensional (out-of-plane) direction.[3,4] Such weak van der Waals interactions between neighboring layers make it possible to cleave the layered mate- rials into individual freestanding few-atom thick—or even single-atom thick—layers via mechanical[5,6] or liquid phase exfoliation[7,8] techniques. Discovered in 2004, graphene, composed of a single layer of carbon atoms bonded together in a hexagonal honeycomb lattice, is the most famous 2D layered material[9] and has plenty of appealing electronic, optical, mechanical, and thermal properties.[10–12] For example, graphene is gapless and semi-metallic, allowing it to interact with light over a broad bandwidth from terahertz (THz) to ultra-violet (UV) wavelengths[13,14] and rendering it a promising material for various photodetectors over a wide spectral range.

However, despite its high absorption coefficient,[15] single-layer graphene can absorb only 2.3% of incident visible and infrared (IR) light due to its thinness, [16,17] which is undesirable for high performance photodetectors that require strong light absorption. Graphene's gaplessness also leads to short photocarrierlifetime in pure

This article may not be enhanced, enriched or otherwise transformed into a derivative work, without express permission from Wiley or by statutory rights under applicable legislation. Copyright notices must not be removed, obscured or modified. The article must be linked to Wiley's version of record on Wiley Online Library and any embedding, framing or otherwise making available the article or pages thereof by third parties from platforms, services and websites other than Wiley Online Library must be prohibited.

graphene, which is unfavorable for efficient photocurrent generation. [18–20] In addition to graphene, this family of materials contains an extremely large range of other 2D-layered materials that have recently attracted much research interest.[1-8] Similar to graphene, being atomically thin, these materials exhibit a wide range of unique electrical, optical, thermal, and mechanical properties that can never be seen in their three-dimensional (3D) bulk counterparts due to the dimensionality confinement effect and modulation in their band structures.[21,22] These 2D-layered materials can be metals, semiconductors, insulators, superconductors, topological insulators, or paramagnetic, diamagnetic, ferromagnetic, or anti-ferromagnetic, etc., depending on their composition and phases.[23,24] Among these materials, particular attention has been paid to 2D layered semiconductors thanks to their unique electronic[2,24–26] and optoelectronic properties,[27,28] which arise from their appreciable bandgaps ranging from IR to UV and throughout the visible range.

The optical and optoelectronic properties of 2D layered semiconductors are strongly dependent on their number of layers due to the quantum confinement effects in the out-of-plane direction and changes in symmetry.[29,30] This layer-dependent modulation of physical properties, such as bandgap structure, is particularly evident in the semiconducting transition metal dichalcogenides (TMDs)[2,7,29,31,32] and few-layer black phosphorus (BP).[33,34] Another effect induced by vertical quantum confinement is the increased absorption efficiency, which results from the strongly bound excitons due to the reduced thick- ness.[29,35,36] The atomic thickness of a 2D layered semiconductor also leads to high transparency[37] and good mechanical flexibility,[38] properties of particular interest for novel device applications such as flexible, wearable, or portable electronics. Despite their high transparency, 2D layered semiconductors can strongly interact with incident light, leading to enhanced photon absorption and electron–hole creation due to the existence of Van Hove singularities in their electronic density of states.[39] It has also been reported that 2D layered materials possess extraordinary elastic modulus and large strain (>10%) before rupture,[40–43] which allow for tuning their electronic and optical properties via strain engineering and the implementation of novel device architectures such as wearable, bendable devices and devices with novel functionalities. Moreover, the van der Waals inter- actions between neighboring layers without surface dangling bonds enable the integration of materials with properties beyond the limitation of lattice matching [44,45] or their direct growth on a variety of substrates. [46,47] This paves the way for designing various functional heterostructures with fundamentally different properties and understanding the underlying mechanisms. Further band engineering of these heterostructures is achievable due to the diversity of 2D layered materials with different bandgaps and work functions. In addition, the ultimate thickness of 2D layered materials offers us the ability to tune their carrier densities, band alignments, and polarities via electrostatic [25,48,49] or chemical [50–52] doping, providing an alternative way to construct functional heterostructures. The wide range of tunable material properties, along with the possibilities for creating various functional heterostructures, render 2D-layered semiconductors promising candidates for future high-performance optoelectronic applications, including various photodetectors

covering a wide spectral range from IR to UV wavelengths.

Photodetectors that can convert light signals into electrical signals are significant in the development of a multitude of innovative technologies in modern society from a practical perspective. These technologies include video and biomedical imaging, optical communication, environment monitoring, military, security checks, night vision, scientific research, and industrial processing control, among others.[15–17,37] Currently, high-performance photodetectors made from crystalline silicon (Si) with a detection range at visible and near- infrared (NIR) dominate the photodetection market, while longer-wavelength photodetectors beyond the detection limit of Si-based products are primarily constructed with materials such as InGaAs and related heterostructures. However, these detectors usually suffer from severe drawbacks, including thick material usage, expensive fabrication processes, strictly controlled fabrication conditions, and rigorous operation demands. These materials in bulk form are also very brittle, making the detectors unsuitable for some novel device concepts, such as transparent, flexible, and bendable applications. Therefore, there is an increasing demand for new materials that can provide high absorption efficiencies in broadband wavelengths, high transparency and flexibility, and can be processed using cost-effective techniques with simplified device geometries to overcome the limitation of bulk Si for photo- detection. The emergence of 2D layered semiconductors with appealing properties such as high transparency, strong light- matter interactions, good flexibility, ease of processing, etc., complements the shortages of current Si technologies and affords great promise towards the realization of high-performance photodetectors.

In this paper, we comprehensively review the photodetection applications of 2D layered semiconductors beyond graphene in recent years, as depicted in **Figure 1**. Photodetectors based on graphene have already been reviewed in several papers and are thus not covered in detail in this paper. [15–17] We first give a brief introduction of the most commonly used synthetic methods for preparing 2D layered materials along with the basic sensing mechanisms and important performance parameters in photodetection. We then review photoconductors and phototransistors based on a variety of2D layered semiconductors and their hybrids. Next, photodiodes, another type of photodetector based on these 2D layered semiconductors, and their artificial heterostructures are discussed. Some emerging techniques for light-matter inter- action enhancement to improve device performance are also addressed. Finally, the existing techniques are summarized and outlooks are provided to shed light on the future development of this research area.

2.Device Fabrication and Physics

2.1. Synthesis Methods for 2D Layered Materials

The preparation of high-quality 2D layered materials with scalable and cost-effective approaches is of significant importance for the realization of high-performance photodetectors based on 2D layered materials. Recently, many

methods have been developed for synthesizing 2D layered materials, which can be generally categorized into two types: top-down methods and bottom-up methods.[21,22] Top-down methods, including techniques such as mechanical exfoliation, liquid phase exfoliation, and so forth, refer to the synthesis of 2D layered materials by breaking apart a single or few atomic layers from the bulk layered materials with the aid of external energy (mechanical or ultrasound energy). In contrast, bottom-up methods are those where atoms or molecules are assembled on a substrate via thermal and/or chemical reactions for the synthesis of 2D layered materials. Processes such as chemical vapor deposition, van der Waals epitaxial growth, and hydrothermal synthesis fall into this category. In this section, a brief description of the most commonly used synthetic methods for the production of 2D layered materials will be presented, and the advantages and limitations of each approach will be discussed. For a more detailed description of the preparation of 2D layered materials, interested readers should refer to other related review papers. [21,22,26,46,53]

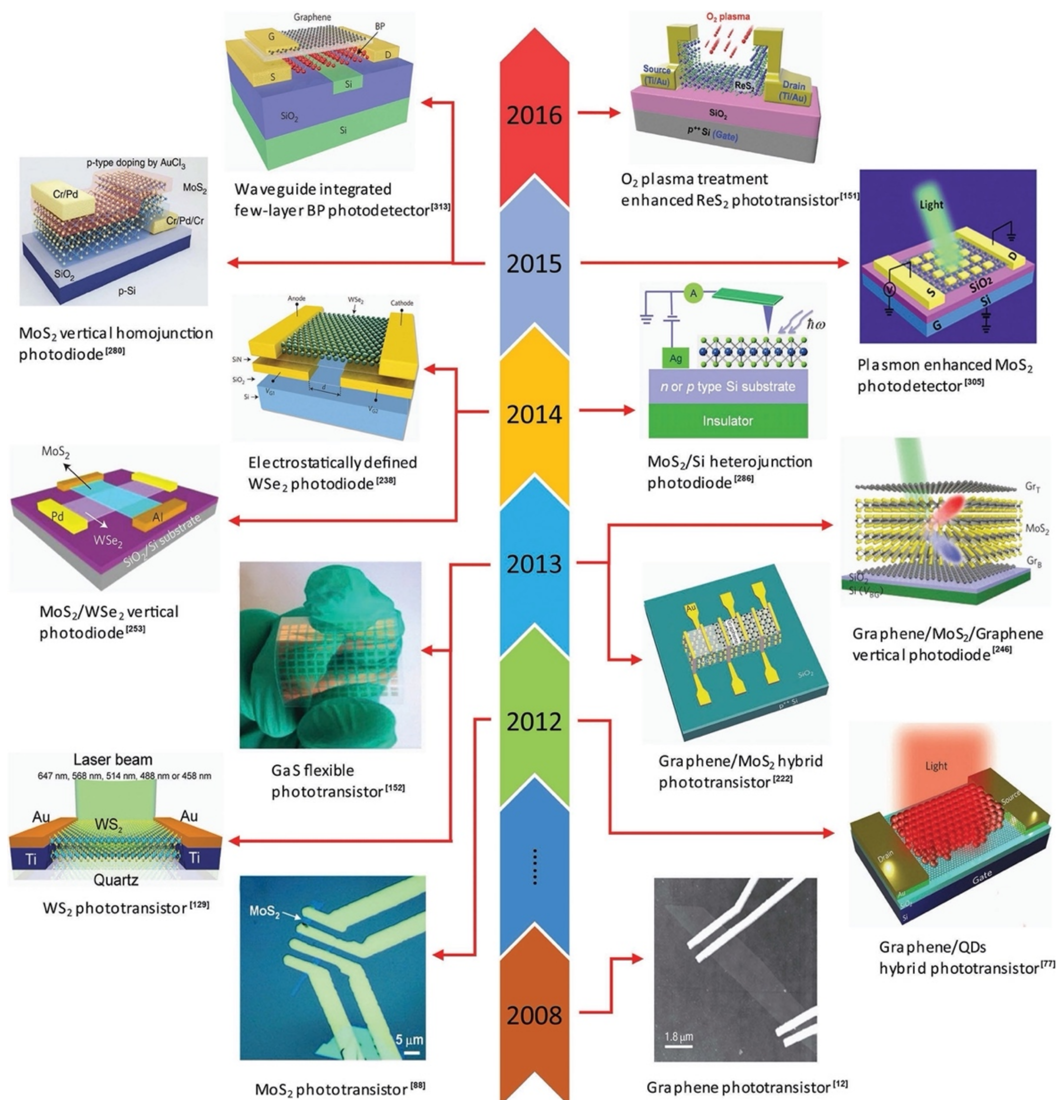

Figure 1. Timeline showing the development of the applications of graphene and other 2D layered semiconductors in photodetectors based on different principles. Reproduced with permission.[12,77,88,129,151,152,222,238,246,253,280,286,305,313] Copyright 2008, 2012, 2013, 2014, 2015, Nature Publishing Group. Copyright 2012, 2013, American Chemical Society.

Copyright 2013, 2015, 2016, Wiley-VCH.

2.1.1. *Mechanical Exfoliation*

The mechanical exfoliation method, invented by A. Geim and K. Novoselov to cleave graphene from highly oriented pyrolytic graphite in 2004, is a traditional technique for obtaining atomical and few-layer thick flakes of 2D layered inorganic materials.[9] Following the isolation of graphene, this approach has been successful for obtaining single or few layers of other non-carbonaceous 2D layered materials, such as TMDs (MoS_2,[2] $MoSe_2$,[54] WS_2,[55] WSe_2,[56] etc.), h-BN[57] (hexagonal boron nitride) and few-layer BP.[25] In a typical process, Scotch tape is used to repeatedly stick and peel apart layered solid flakes into thinner layers until single- or few-layer flakes are attained on the tape. The flakes are washed with acetone and transferred onto an oxidized Si substrate. The number of layers in the exfoliated flakes can be determined by optical microscopy, atomic force microscopy (AFM) height profiles, scanning tunneling microscopy (STM), and high-resolution transmission electron microscopy (HRTEM). The obtained 2D flakes, which maintain the crystal structure of the bulk form, can remain stable in ambient conditions for days to months. Mechanical exfoliation is a low cost and convenient method for 2D layered materials production and is highly suitable for fundamental research where 2D flakes with structural integrity, high crystallinity, minimal defects are desired. However, scalable production is highly challenging due to the low throughput from this process. In addition, this method lacks controllability in uniformity, size, and thickness of the peeled flakes, and thus does not meet the requirements for practical applications.

2.1.2. Liquid Phase Exfoliation

An alternative method to obtain single- or few-layer 2D materials is based on liquid-phase exfoliation, which can be divided into solvent exfoliation and chemical exfoliation. Solvent exfoliation generally involves the processes in which bulk layered crystals or powders are dispersed in a suitable organic solvent and sonication is employed as a source of external energy to cleave the bulk materials into atomically thin sheets. Afterwards, the resultant dispersion is centrifuged to separate large crystals; critical parameters that dictate the quality of the dispersion are sonication time and centrifugation rate. Also, the selection of an appropriate solvent is another key factor, and it has been suggested that solvents with surface tension similar to the surface energy of 2D layered materials can not only minimize the energetic cost of exfoliation but also facilitate the sheet separation.[21,46] A variety of 2D layered materials such as MoS_2, WS_2, $MoSe_2$, $MoTe_2$, $NbSe_2$, $TaSe_2$, $NiTe_2$, VS_2, and h-BN have been successfully synthesized using this method in some common solvents, including NMP (*N*-methyl-2-pyrrolidone), DMF (dimethylformamide), DMSO (dimethyl sulfoxide), IPA (isopropyl alcohol), cyclohexyl-pyrrolidinone, Ndodecyl-pyrrolidone, NVP.[8,58–62] Usually, this method yields single- and few- layer 2D nanosheets with micrometer dimensions dispersed homogeneously in a solvent. A density gradient ultracentrifugation method can be used to separate single layers from few- layers, which has proved to be an effective means of separating single-layer

graphene oxide from the solution.[63]

However, despite the low-cost, large-scale production ability of this method, it faces drawbacks such as poor uniformity in layer thickness and low yields of large flakes and single-layers, which are highly desired for electronic and optoelectronic applications. To address this issue, a chemical exfoliation method has been developed. In a typical process, the interlayers of a bulk layered material are intercalated with small ions such as lithium ions, which break the interlayer van der Waals bonding with external agitation and separate the layers. [21,54] A suspension of single layers is readily obtained after washing with a suitable solvent to remove excess lithium and other organic residues. This method has been successfully applied for obtaining single layers of 2D TMDs, such as MoS [7,64] and WS_2.[65] Lithium-based intercalation exfoliation is a highly desirable and versatile process that facilitates the low cost and large scale production of single layers of 2D materials. However, some challenges still exist, such as homogeneous dispersion of 2D single layers and precise control of the layer size. Moreover, residual lithium ions physically absorbed at the surface of the single layers are inevitably incorporated in a lithium-based intercalation process, which deteriorate the electrical and thermal properties of the final products. Another reported drawback is the phase transition in MoS_2 caused by the lithium intercalation, which can be reversed by performing an additional thermal annealing process.[7]

Furthermore, with the aid of electrochemical systems, Zhang's group has developed an electrochemical lithium-based intercalation and exfoliation method.[66,67] Briefly, they used a bulk layered crystal as cathode and a lithium foil anode in a lithium ion battery setup. During the discharge process, lithium ions are intercalated into the interlayers of the crystal. The lithium reacts with water or ethanol to generate H_2 gas, which facilitates the separation of adjacent layers. Finally, nanosheets hundreds of nanometers in size, homogeneously dispersed in a solvent, are obtained under vigorous agitation by sonication. Various 2D layered materials, including MoS_2, WS_2, TiS_2, TaS_2, ZrS_2, $NbSe_2$, WSe_2, Sb_2Se_3, Bi_2Te_3, h-BN, and graphene single-layers have been successfully prepared by this method. [66,67] Compared with common lithium intercalation, this method can provide good control over the degree of lithium intercalation by monitoring the discharge curve. This means the amount of inserted lithium can be optimized to avoid insufficient or excessive lithium intercalation.

2.1.3. Chemical Vapor Deposition

The chemical vapor deposition (CVD) technique has been extensively employed to synthesize large-area homogeneous 2D TMDs with controllable thickness and excellent proper-ties. Compared with the above discussed top-down methods, this bottom-up method has many distinct advantages. In addition to the scalable size and controllable thickness of the final products, the growth instruments are inexpensive and versatile. Moreover, the preparation process is compatible with current semiconductor technology. As an example, we describe the growth of 2D MoS_2 to introduce the synthesis of 2D TMDs via the CVD method. The most commonly used CVD method involves MoO_3 and sulfur powders as starting

materials to deposit single- or few-layer MoS_2 on an SiO_2/Si substrate. [47,68] At high temperature under an inert atmosphere, MoO_3 powders are reduced by the sulfur vapor to form volatile suboxide MoO_{3-x}, which diffuses to the substrate and reacts with sulfurvapor to grow MoS_2 layers with lateral sizes up to 2 mm. The substrate can also be pretreated with graphene-like molecules, such as reduced graphene oxide (rGO), perylene-3,4,9,10-tetracarboxylic acid tetrapotassium salt (PTAS), and per- ylene-3,4,9,10-tetracarboxylic dianhydride (PTCDA) to promote the layer growth of MoS_2.[47] This method has also been appliedto the growth of MoS_2 or WS_2 layers on other insulating substrates including quartz and sapphire.[69] In addition, wafer-scale MoS_2 thin layers have been synthesized using MoO_3 thin films pre-deposited on a sapphire substrate as a starting material. This is followed by a two-step thermal process, where reduction of MoO_3 occurs in a H_2/Ar environment and further sulfurization in a sulfur-rich environment at elevated temperature yields MoS_2 layers.[70] In the second method, pre-deposited Mo thin layers on a SiO_2/Si substrate have been employed toreact with sulfur vapor, which gives rise to large-area single- or few-layer MoS [71] This process is highly scalable because thesize and thickness of the resultant MoS_2 layers can be directly determined by the size and thickness of the starting Mo films.In addition, Liu et al. reported that the thermal decomposition of $(NH_4)_2MoS_4$ layers dip-coated on various insulting substratesin the presence of sulfur vapor via a two-step annealing process can produce large-area MoS_2 layers, providing an alternative strategy for synthesizing MoS_2 with scalable size.[72]

The direct growth of MoS_2 layers on insulting substratescan afford the distinct advantage of skipping the film transfer step that is needed for CVD-growth graphene. Thus, somedrawbacks usually associated with this step, such as chemical residues, possible physical film damage, and wrinkle formationcan be avoided. Also, MoS_2 films produced by these methods are transferable to arbitrary substrates with the help of PMMA (poly (methyl methacrylate)) and NaOH.[22]

Recently, four-inch wafer-scale films of monolayer MoS_2 and WS_2 with excellent spatial homogeneity and coverage have been successfully grown on SiO_2/Si substrates using a metal- organic CVD technique.[73] In this approach, $Mo(CO)_6$, $W(CO)_6$, $(C_2H_5)_2$, and H_2 are employed as gas-phase precursors, and argon is used as the carrier gas. The resultant MoS_2 layers showgood electrical properties such as a high electron mobility of 30 $cm^2V^{-1}s^{-1}$, which is comparable to the mechanically-exfoliated monolayer MoS_2. Also, the wafer-scale batch fabrication of monolayer MoS_2 field effect transistors (FETs) has achieveda device yield of 99% with the use of these MoS_2 films. These results are promising and show potential towards the realization of wafer-scale electronics and optoelectronics based on 2DTMDs.

2.2. Sensing Mechanisms

A photodetector is an optoelectronic device that can convert absorbed optical energy into electrical signal, such as photocurrent or photovoltage. Several sensing mechanisms have been reported, including photoconductive effect, photogating effect, photovoltaic effect, photothermoelectric effect, and bolometric effect.

Based on the sensing mechanism, photodetectors can be divided into two categories: photon (or quantum) detectors (including photoconductors/phototransistors and photodiodes) and thermal detectors. In the following section, we introduce the mechanisms for photodetectors based on 2D layered semiconductors

2.2.1. Photoconductive Effect

The photoconductive effect involves a process in which photon absorption by a semiconductor generates excess free carriers and results in an increase in conductivity. [74,75] A typical photoconductor consists of a semiconductor as a channel, with two ohmic contacts affixed to opposite ends of the channel that serve as source/drain electrodes. In darkness, the channel allows only a small source-drain current to flow (dark current, I_d) under a bias applied between the electrodes (V_{DS}). Under illumination, photons with energy larger than the bandgap of the semiconductor are absorbed, which leads to the generation of electron–hole pairs (or excitons depending on the material). The photoexcited electron-hole pairs are then separated by the V_{DS}, and the free electrons and holes drift oppositely towards the source/drain electrodes. This process leads to a net increase (photocurrent, I_{ph}) in the channel current. It is noteworthy that carrier recombination usually takes place at the surface and bulk of the semiconductor, which leads to a decrease in photocurrent. Normally, a strong V_{DS} is desired to facilitate electron-hole pair separation and consequently carrier transportation. The lifetime of the photocarriers has a significant effect on the photoconductive gain (G) and the response speed. A photoconductor can have gain larger than unity. Under a moderate V_{DS}, the majority of carriers (assumed to be electrons) have a much higher mobility and consequently a much shorter transit time than that of the minority carriers (holes). Thus, the photoexcited electrons can drift across the channel much more quickly than the photoexcited holes. To maintain charge neutrality, more electrons are supplied from the other electrode and circulate many times in the channel during the lifetime of holes. The gain depends upon the ratio of lifetime of holes ($\tau_{lifetime}$) to the electron transit time ($\tau_{transit}$) and is expressed as $G=\frac{\tau_{lifetime}}{\tau_{transit}}$. In order to obtain a high gain, the electron transit time has to be short, while the lifetime of holes should be long. On the other hand, the response time, which is related to the carrier recombination processes, is also determined by the lifetime of holes. This means that high gain will reduce the response speed. Therefore, a trade off has to be made between gain and response speed to get a reasonable overall performance of a photoconductor.

τ

2.2.2. Photogating Effect

The photogating effect can be regarded as a special case of the photoconductive effect. Under illumination, electron-hole pairs are generated in the semiconductor, and subsequently one of the two carrier types (electrons or holes) is trapped in the localized states located at defects and/or at surface adsorbates.[76] Another case of electron–hole generation takes place in the surface adsorbates or charge traps adjacent to the semiconductor serving as a conducting channel.[77,78]

Consequently, one type of carrier is transferred to the channel, leaving oppositely-charged carriers trapped in the surface adsorbates or traps. These trapped carriers act as local gates and effectively modulate the conductance of the semiconductor due to electrostatic interactions. The carriers in the semiconductor can recirculate many times during the lifetime of the trapped carriers, leading to a high gain. Notably, this effect is particularly pronounced in nanostructured materials with large surface-area-to-volume ratios, such as colloidal quantum dots, nanowires, and 2D layered materials. Although photodetectors with a photogating effect can have a higher gain than photoconductors, they usually suffer from slower response speed. Sometimes, the two effects can take place in the same device and contribute to the photocurrent simultaneously.

2.2.3. Photovoltaic Effect

The photovoltaic effect relies on a built-in electric field to separate the photogenerated electron–hole pairs and propel electrons and holes towards opposite directions.[79] The built-in electric field is normally produced at a junction (a depleted semiconductor region), where there is a significant difference in the work functions between materials. Photodetectors that opeate via the photovoltaic effect are usually called photodiodes. Generally, the photodiode family contains p-type/n-type (PN) photodiodes formed by two semiconductors with opposite doping type and Schottky barrier photodiodes formed at the interface between a semiconductor and a metal. A PIN photodiode is one example of a PN photodiode, where "I" represents an intrinsic semiconductor layer inserted between the PN junction. A photodiode usually displays an asymmetric current–voltage characteristic (rectifying behavior) in the dark, while the device can function at two modes under illumination, i.e., the photovoltaic mode (at zero bias) and the photo-conductive mode (under reverse bias). In photovoltaic mode, the photogenerated electron–hole pairs are separated by the built-in electric field and electrons and holes are collected at opposite electrodes, which generates a considerable photocurrent (short-circuit current, I_{SC}). The electrical output can also be a photovoltage (open-circuit voltage, V_{OC}), which is obtained by keeping the circuit open. A photodiode working in this mode has the lowest dark current, thus leading to an improved detectivity, as well as maximized linearity and sensitivity. In photoconductive mode, the external electric field with a moderate biasing voltage has the same direction as the built-in one, which increases the separation efficiency of the electron–hole pairs, as well as the response speed due to reduced carrier transit time and lowered diode capacitance. In practice, a photodiode in photovoltaic mode is well suited for precision applications, while a photodiode in photoconductive mode is better suited for high-speed applications. Normally, a photodiode has a maximum gain of unity, much smaller than a photodetector operating via the photoconductive or photogating effect. However, too-large reverse bias can cause avalanche multiplication or breakdown of a photodiode (avalanche photodiode, APD), where photogenerated electrons with enough energy initiate impact ionization, providing large internal current gain.

2.2.4. Photo-Thermoelectric Effect

The photo-thermoelectric effect occurs when non-uniform light-induced heating on two dissimilar conductors or semiconductors leads to a temperature gradient, causing a temperature difference (ΔT) between the two substances. This temperature difference can result in a voltage difference, namely the photo-thermoelectric voltage (V_{PTE}), through the Seebeck effect (or thermoelectric effect). The photo-thermoelectric voltage V_{PTE} can be expressed as [80,81]

$$V_{PTE} = (S1 - S2)\Delta T \quad (1)$$

where S_1, S_2 are the Seebeck coefficients of the two substances. The photo-thermoelectric voltage can produce a current through the circuit at zero applied bias. Note that the photo-thermoelectric effect cannot be found in a uniform semiconductor because negligible temperature gradients can be achieved. Normally, the temperature gradient can be obtained by localized illuminating of a measured device, or by globally illuminating a device with distinct absorption coefficients in different parts.

2.2.5. Bolometric Effect

The bolometric effect is based on the resistance change of a material induced by uniform heating under illumination.[82] Two factors, the conductance variation of a material with temperature (dG/dT) and the homogeneous temperature increase (ΔT) induced by the heating, determine the magnitude of this effect. Bolometers have been widely used in astronomy, where sensitive detection of mid- and far-IR as well as THz is much desired.[83] The bolometric effect has also been observed in graphene-based photodetectors, where carriers can easily be heated due to weak carrier-phonon coupling, [84,85] and in photo- detectors based on few-layer BP with≈100 nm thickness.[86]

2.3. Photodetector Performance Parameters

In general, several important parameters are used to compare the detection performance of photodetectors that operate under different mechanisms and are constructed from different mate- rials and geometries. In the following section, we will give a brief introduction to these parameters.

Responsivity (R): The responsivity R of a photodetector is defined as the ratio of the output photocurrent or photovoltage to the input optical power on the active region of the device, which is usually expressed as

$$R = \frac{\text{Photocurrent A or photovoltage (V)}}{\text{Input optical power (W)}} = \frac{I_{ph} \text{ or } V_{ph}}{P_{in}} \quad (2)$$

where I_{ph} is the photocurrent, V_{ph} is the photovoltage, and P_{in} is the input optical power. This parameter is used to indicate the available output photocurrent or photovoltage of the photodetector for a given incident optical power at a certain wavelength.

External Quantum Efficiency (EQE): The external quantum efficiency EQE is the ratio between the number of electron-hole pairs with contribution to the photocurrent and the number of incident photons. It can be expressed as

$$EQE = \frac{I_{ph}/e}{P_{in}/h\nu} = R\frac{hc}{e\lambda} \quad (3)$$

where e is the elementary charge, h is Planck's constant, ν is the frequency of incident light, c is the speed of incident light, and λ is the wavelength of incident light. To achieve a large *EQE* in a photodetector, the optical absorption of the active layer should be high, while the carrier recombination and trapping before being collected should be minimized.

Internal Quantum Efficiency (*IQE*): Similarly, the internal quantum efficiency *IQE* is the ratio between the number of electron-hole pairs with contribution to the photocurrent and the number of absorbed photons by the detector. The number of absorbed photons can be determined by deducting the photon losses, including those due to transmission and reflection, from the total number of incident photons. The optical interference effects should especially be taken into account in photodetectors with an ultrathin active layer.

Speed and Bandwidth (Δf): The response speed determines the ability of a photodetector to follow a rapid modulated optical signal. In the time domain, the rise time t_r and the fall time t_f are typically used to characterize the response speed of a photodetector. In some examples from the literature, the rise time t_r and the (fall time t_f) is defined as the time interval required for the the response to rise (decay) from 10% (90%) to 90% (10%) of its peak value. A photodetector with a fast response speed is highly desirable in certain areas, such as optical communication, video imaging, etc.

Generally, the overall response speed of a photodetector is determined by its bandwidth Δf, including the intrinsic bandwidth and radio frequency (RC) circuit-limited bandwidth. The bandwidth of a photodetector is defined as the difference between the upper (f_2) and lower (f_1) light modulation frequencies, where the detector has uniform response in this range and no response outside of this range, expressed as $\Delta f = f_2 - f_1$. Another widely used parameter in the frequency domain is 3-dB bandwidth (f_{3dB}), which is the frequency at which the response drops to -3 dB (50%) of its peak value and is related to Δf by $f = 0.886\Delta f$. The f_{3dB} of a photodetector and its corresponding t_r are related as follows:[87]

$$t_r = \frac{0.35}{f_{3dB}} \quad (4)$$

Signal *to Noise Ratio (SNR)*: Low noise is a significant factor for a photodetector because it ultimately determines the lowest detectable signal strength. Noise always exists in a photodetection process, which limits the detection of small amounts of radiation energy by producing a random fluctuation in the output of the device. The SNR of a photodetector is expressed as

$$SNR = \frac{\text{Signal power}}{\text{Noise power}} \quad (5)$$

The *SNR* must be larger than 1 so that the signal power can be distinguished from the noise.

Noise Equivalent Power (*NEP*): Noise equivalent power *NEP* is the minimum

impinging optical power required to achieve an *SNR* of 1 in a 1 Hz bandwidth. The *NEP* is defined as

$$NEP = \frac{P_1}{\sqrt{\Delta f}} \tag{6}$$

where P_1 is the incident optical power that produces *SNR* = 1.

The *NEP* can be written in some cases as

$$NEP = \frac{\overline{i_n^2}^{1/2}}{R} \tag{7}$$

where $\overline{i_n^2}^{1/2}$ is the mean-square noise current measured at the bandwidth of 1 Hz in darkness (in A Hz$^{-1/2}$). For a photodetector that has an output voltage signal, the $NEP = \frac{\overline{v_n^2}^{1/2}}{R}$, where $\overline{v_n^2}^{1/2}$ is the mean-square noise voltage measured at the bandwidth of 1 Hz in darkness (in V Hz$^{-1/2}$).

Detectivity (*D**): The detectivity *D** is a useful parameter for comparing the detection performance of photodetectors with different materials and geometries, and is defined as

$$D^* = \frac{(A\Delta f)^{1/2}}{NEP} \tag{8}$$

where *A* is the device area and *f* is its bandwidth. Since the total device noise is normally proportional to the square rootof the area, the *D** is independent of the area. This parameter depends on sensitivity, spectral response, and noise of the device. If the shot noise from dark current dominates the total noise of a photodetector, the *D** can be written as

$$D^* \approx \frac{A^{1/2}R}{(2eI_d)^{1/2}} \tag{9}$$

Where I_d is the dark current.

3. Photoconductors/Phototransistors Based on 2D Layered Semiconductors

A photoconductor/phototransistor is the simplest type of photo- detector, usually operating with the photoconductive effect, photogating effect, or two effects combined. A photoconductor can provide a high photocurrent gain at the expense of reduced response speed. In particular, by exploiting the inherent amplification function, a phototransistor can obtain an even higher gain. The electronic band structure of a semiconductor greatly influences its optical absorption, which in turn affects its opto- electronic properties. Due to the atomic thickness and large surface area, photodetectors based on 2D layered semiconductors are expected to demonstrate some novel phenomena and achieve superior performance compared to their bulk or thin- film counterparts. In this section, we review the achievements involving photoconductors/phototransistors based on 2D layered semiconductors.

3.1 Transition Metal Dichalcogenides (TMDs)

TMDs represent a class of layered materials with generalized formula MX_2, where

M is a transition metal from group 4–7 and X is a chalcogen atom such as S, Se, or Te.[22,24] Each layer of TMDs is composed of one layer of hexagonally packed metal atoms with two atomic layers of chalcogen atoms covalently bonded on either side. Similar to graphene, several layers are bonded together by weak van der Waals interactions to form a bulk crystal. This weak interaction along the out-of-plane direction allows the bulk crystals to be isolated down to single layers, which offers the opportunity for fundamental research and proof-of-concept device fabrication based on 2D TMDs. Single- or few-layer semiconducting TMDs hold unique optical and opto-electronic properties that do not exist in their bulk counterparts, which renders them attractive for high-performance photodetection applications. The key parameters of the photoconductors/phototransistors based on TMDs are summarized in **Table 1**.

Table 1. Performance of photoconductors/phototransistors based on 2D TMDs. ML: Multilayer, CVD: Chemical vapor deposition, FL: Few-layer.

	Active layer	Spectral range	Responsivity [AW^{-1}]	Response times [ms]	Detectivity [Jones]	Ref.
MoS_2	Mechanically exfoliated 1L	Visible	7.5×10^{-3}	50	–	[88]
	Mechanically exfoliated 1L	Visible	880	600	–	[89]
	Mechanically exfoliated ML	UV-visible-NIR	0.12	–	$\approx 10^{11}$	[91]
	CVD-grown 1L (in vacuum)	Visible	2.2×10^{3}	2.2×10^{5}	–	[95]
	CVD-grown 1L	Visible	1.1×10^{-3}	$> 10^{3}$	–	[98]
	CVD-grown FL	Visible	0.57	7×10^{-2}	$\approx 10^{10}$	[99]
	Liquid exfoliated FL	UV-visible-NIR	3.6×10^{-5}	60	–	[100]
	Magnetron sputtered 5L	Visible-NIR	1.8	–	5×10^{8}	[102]
	Solution-synthesized 2–4L	UV-visible	6.3×10^{-5}	20	4.2×10^{8}	[103]
	Self-limiting grown FL (after laser micromachining)	Visible	0.55	0.2	–	[104]
	lly exfoliated ML (local bottom gated)	Visible	342.6	$> 10^{3}$	–	[105]
	e Mechanically exfoliated 1–2L (HfO_2 encapsulation)	Visible	10^{4}	10	7.7×10^{11}	[106]
	Mechanically	Visible-NIR	2570	1.8	2.2×10^{12}	[107]

	exfoliated FL (enhanced by ferroelectrics)					
	Mechanically exfoliated 10L (MESFET structure)	Visible	5000	2	–	[108]
	APTES doped FL	Visible	5.75×10^{3}	–	4.47×10^{9}	[111]
$MoSe_2$	Mechanically exfoliated FL	Visible	97.1	15	–	[120]
	CVD-grown 1L	Visible	2.15×10^{-4}	25	–	[124]
	CVD-grown 1L	Visible	1.3×10^{-2}	60	–	[125]
	CVD-grown ML	Visible	93.7	400	–	[126]
WS_2	CVD-grown FL	Visible	9.2×10^{-5}	5.3	–	[129]
	echanically exfoliated ML n NH_3 atmosphere)	Visible	884	$>10^{3}$	–	[130]
	CVD-grown 1L (in vacuum)	Visible	1.88×10^{-2}	$<10^{3}$	–	[131]
	PLD-grown ML (in vacuum)	UV-visible-NIR	0.70	9.9×10^{3}	2.7×10^{9}	[132]
	Magnetron Sputtered ML	UV-visible	53.3	–	1.22×10^{11}	[133]
WSe_2	OTS-doped FL	Visible	1.45×10^{4}	–	5.3×10^{10}	[111]
	CVD-grown 1L	Visible-NIR	1.8×10^{5}	5×10^{3}	$>10^{14}$	[134]
	Mechanically exfoliated 3L	Visible	7	1×10^{-2}	–	[135]
	CVD-grown 1L	Visible	1.1	$>10^{3}$	–	[136]
	PPh_3-doped FL on hBN	Visible	1.27×10^{6}	2.8	–	[137]
$MoTe_2$	Mechanically exfoliated FL	Visible	2560	–	–	[141]
HfS_2	Mechanically exfoliated FL	Visible	890	38	1.3×10^{10}	[142]
$ReSe_2$	echanically exfoliated 1L environment)	Visible	95	68	–	[144]
	Mechanically exfoliated 1L (Mo-doped, in NH_3 environment)	Visible	55.5	96	–	[145]
ReS_2	CVD-grown FL	Visible	16.14	$>10^{5}$	–	[146]
	Mechanically exfoliated FL	Visible	$>10^{3}$	98	–	[147]

	CVD-grown 2L	Visible	604	2	4.44×10^{10}	[148]
	Mechanically exfoliated FL	Visible	8.86×10^{4}	$>10^{5}$	1.18×10^{12}	[149]
	PPh_3 and APTES co-doped FL	Visible-NIR	1.18×10^{6}	30	–	[150]
	Mechanically exfoliated ML (treated by O_2 plasma)	Visible	2.5×10^{7}	670	–	[151]

3.1.1 Molybdenum Disulphide (MoS_2)

Single-layer MoS_2 possesses striking properties such as a direct bandgap of ≈1.8 eV,[2,29] large carrier mobility above 200 $cm^2 V^{-1} s^{-1}$[7,29,32], a high-current ON/OFF ratio of up to 1×10^8,[2] strong photoluminescence (PL),[7,32] good chemical stability and mechanical flexibility, ease of processing, and so on.[24,28,29,38] These appealing features make single- or few-layer MoS_2 the most extensively studied 2D layered semiconductor with great potential in photodetection. A phototransistor based on a mechanically-exfoliated single-layer MoS_2 nanosheet with a typical FET configuration was first reported by Yin et al.[88] (Inset in **Figure 2**a). As shown in Figure 2a, the phototransistor exhibits a distinct response with a cut-off wavelength at 670 nm, which agrees well with the bandgap of the single-layer MoS_2 (≈ 1.8 eV). This device achieved a maximum responsivity of ≈7.5 mAW^{-1} in the electron accumulation region, which can be further tailored by drain and gate voltages, along with a fast response speed within 50 ms. Later, Lopez-Sanchez et al. demonstrated a similar phototransistor made from exfoliated single-layer MoS_2 with a greatly enhanced responsivity up to 880 A W^{-1} in the electron depletion region (Figure 2b) and a response cut-off wavelength at 680 nm.[89] This significant improvement is explained by the improved carrier mobility and contact quality, as well as the positioning technique. Importantly, this device possesses a remarkably low *NEP* of down to 1.5×10^{-15} W $Hz^{-1/2}$, associated with its reduced dark current at the depletion region, due to the 1.8 eV bandgap that suppresses the thermally activated carriers and the efficient electrostatic tunability in the atomically thick layer. However, the response time of the device is slow (on the order of several seconds), which is influenced dramatically by the surroundings of MoS_2. With the help of a short gate pulse to discharge trapped charge carriers, the response times can be reduced to less than 0.6 s. In contrast to the first-reported MoS_2 phototransistor,[88] the photocurrent displays a sublinear dependence on light intensity. This behavior, combined with the tunable response speed influenced by the surroundings of MoS_2, confirms that charge trapping in MoS_2 and/or at the MoS_2/SiO_2 interface plays a major role in the sensing process.

The layer number of MoS_2 has a significant influence on its band structure, consequently affecting the photodetection performance.[29,30] Lee and co-workers have fabricated transparent top-gate phototransistors based on exfoliated single-, double-, and triple-layer MoS_2.[90] Their studies show that the optical bandgap for the single-layer MoS_2 is ≈1.82 eV, while the values reduce to ≈1.65 and ≈1.35 eV

for the double- and triple-layer counter- parts, respectively, as shown in Figure 2c. As a result, triple-layer MoS_2 shows good detection performance for red light, while single- and double-layer MoS_2 are more suitable for green light detection. This bandgap reduction therefore allows multilayer MoS_2 to detect light with an extended wavelength range up to NIR.[91] Although benefitting from higher light absorption due to increased thickness, the phototransistor based on multilayer MoS_2 exhibits an inferior responsivity of ≈ 100 mA W^{-1}, which might be associated with the direct bandgap of multilayer MoS_2.[92,93] Another work by Khan et al. also demonstrated that the responsivity and response speed are highly dependent on the layer number of MoS_2 as well as the environment.[94]

Two-dimensional MoS_2 prepared with different methods usually have distinct qualities that are crucial to photodetector performance. A phototransistor based on CVD-grown monolayer MoS_2 reported by Zhang et al. [95] showed a maximum responsivity as high as 2200 A W^{-1} in vacuum, which was reduced to 780 A W^{-1} in air. Taking into account the large surface-to-volume ratio of MoS_2, adsorbates found at the surface of MoS_2 and/or at the MoS_2/substrate interface from ambient air can act as p-type dopants with additional Coulomb potentials, [96,97] causing increased carrier scattering and decreased electron mobility and responsivity in air. The adsorbates could also affect the photoresponse by serving as recombination centers for photocarriers, leading to a decreased responsivity, yet faster photocurrent relaxation. The defects and charge impurity states inside the bandgap of MoS_2, which act as trap centers for photocarriers, are considered to be responsible for the observed persistent photoconductance. In another study, Perea-López and colleagues also built a photodetector based on CVD-grown monolayer MoS_2 with a much lower responsivity of only 1.1 mA W^{-1}.[98] The huge variation in responsivities presented in the two studies highlight the important roles of contact resistance and active contact region in high-performance photodetectors. CVD-grown few-layer MoS_2 has also been exploited as a photodetector for use in harsh environments.[99] The device exhibits an obvious photocurrent/ dark current ratio of ≈ 10, even at 200 °C. MoS_2 nanosheets prepared from other methods, such as liquid exfoliation, [100,101] magnetron sputtering,[102] and solution synthesis [103] have also been employed in photodetectors. However, these devices usually exhibit inferior responsivities to their counterparts based on mechanically-exfoliated or CVD-grown MoS_2.

Both photoconductive and photogating effects were found to contribute to the photocurrent in single and bilayer MoS_2 photodetectors.[92] The two effects exhibit largely different response times, which offers the possibility to identify them in the photocurrent generation processes. The photogating effect is a slow process and shows an obvious dependence on the gate voltage, which likely arises from long-lived charge trap states at the interface of the MoS_2 and SiO_2 surface hydrated by water molecules. From the dynamics of the photocurrent measurement, the density of these trap states is estimated to be ≈ 10^{15} cm^{-2}. In contrast, the photoconductive effect is a fast process with negligible gate voltage dependence, which is attributed to both shallow trap states and mid-gap states as a result of structural defects in

MoS_2 or disorder. By modulating the incident light illumination at a faster frequency than the photogating effect, the photoconductive response of the device can be studied by a lock-in technique. A model based on mid-gap states and hole-trap states is proposed to fit the obtained experimental data, from which the density of hole-trap states is determined to be $\approx 5\times10^{10}$ cm^{-2}.

Recently, several strategies have been developed with the aim of enhancing the performance of MoS_2 photodetectors. [104–111] Lu et al. demonstrated a facile and effective focused laser thinning method to achieve micropatterning and localized modification of multilayer MoS_2 films.[104] Due to surface oxidation or oxygen doping introduced, a photodetector based on modified MoS_2 shows a promoted photoresponse with a responsivity increase of several fold. The photoresponse of a multi- layer MoS_2 phototransistor can be greatly enhanced by using a local bottom-gate structure, as recently reported by Kwon et al. [105] With this unique design, the device shows significantly improved photocurrent compared to those of previously reported global-gated multilayer MoS_2 phototransistors.[90,91] The accumulation of photoexcited holes due to the large tunnel barrier imposed by the gate at ungated channel regions reduces the potential barrier for electrons, resulting in increased thermionic current in the electron depletion region. On the other hand, improved photocurrent in the electron accumulation region is associated with a decreased tunnel barrier for photoexcited holes and suppressed dark current due to the series resistance in the ungated regions. As a result, the responsivity increases drastically—by three orders of magnitude-to 342.6 A W^{-1}. Afterwards, Kufer and co-workers found that encapsulation with atomic-layer-deposited (ALD) HfO_2 can significantly enhance both the electronic and optoelectronic performance of monolayer or few-layer MoS_2 phototransistors.[106] The encapsulated MoS_2 exhibits enhanced n-type doping with vanishing hysteresis behavior in transfer curves. This is due to reduced surface adsorbates that serve as charge-trapping centers and additional electrons induced by positively fixed charges inside the top-oxide layer, as well as improved carrier mobility originating from the removal of extrinsic charged impurities and the quenching of homopolar phonon modes. The improved carrier mobility, combined with lowered contact resistance, thus gives rise to a much-improved responsivity (Figure 2d) and response speed, which can be effectively tuned by the gate voltage. The responsivity ranges from ≈ 10 to $\approx 10^4$ AW^{-1} and response times are in the range of ≈ 10 ms to10 s. Meanwhile, Wang et al. reported performance enhancement in a multilayer MoS_2 phototransistor driven by a ferroelectric P(VDF-TrFE) gate dielectric.[107] The stable remnant polarization of P(VDF)-TrFE provides an ultrahigh local electrostatic field in the channel; this ensures MoS_2 is fully depleted and leads to an ultralow dark current. Based on this design, the device demonstrates a significantly increased responsivity up to 2750 A W^{-1} and a high detectivity of $\approx 2.2\times10^{12}$ Jones. The response speed is also improved with rise and decay times of ≈ 1.8 and ≈ 2 ms, respectively, due to the encapsulation or passivation of the surface trap states on MoS_2 by the fluorine or hydrogen atoms from polarized P(VDF-TrFE). More importantly, the authors found that the detection range of the ferroelectric-driven phototransistor extended from ≈ 900 nm up to ≈ 1550 nm (Figure 2e), which is

associated with the change in the MoS_2 bandgap[112,113] and defects in MoS_2 flakes, both induced by the external electrostatic field. Recently, Lee and colleagues demonstrated that the influence of interface traps or an on-state gate voltage on carrier transport behavior in few-layer MoS_2 can be minimized by employing a metal-semiconductor field-effect transistor (MESFET) structure, where the NiO_X contact can form a van der Waals Schottky junction with MoS_2.[108] This type of structure enables high carrier mobilities of 500-1200 cm^2 V^{-1} s^{-1} at low threshold voltages due to a reduced charge scattering effect. Thanks to the high carrier mobility, the device reaches a high responsivity of up to 5000 A W^{-1} in the transistor ON state and fast response times of 2 ms (Figure 2f). This response time is superior to those of a MoS_2 phototransistor with metal-insulator- semiconductor FET (MISFET) configuration, which are ＞250 ms. Electron doping of single- and few-layer MoS_2 by surface functionalization of Cs_2Co_3 or an amino-propyltriethoxysilane (APTES) monolayer has also been proven to be an efficient way to improve the performance of MoS_2-based phototransistors.[110,111] Usually, these sur- face functionalizations lead to an enhancement in photocurrent of several folds to tenfold, which is attributed to two phenomena. Firstly, electron doping induces the formation of negative trions, i.e., quasiparticles comprised of two electrons and one hole, in MoS_2 under illumination. This can significantly reduce the recombination of photo-excited electron–hole pairs or excitons. On the other hand, surface functionalization can effectively increase carrier mobility in MoS_2 due to suppressed impurity scattering, which is desirable for fast photocarrier transportation. As a consequence, a high responsivity of up to 5.75×10^3 A W^{-1} and a detectivity close to 10^{10} Jones have been demonstrated in a APTES-doped MoS_2 phototransistor.[111]

Photodetectors with broad response bandwidth are highly desired for some applications. By using the ultrafast two-pulse photovoltage correlation (TPPC) technique, Wang et al. showed that the intrinsic response times of monolayer MoS_2 can be as short as 3 ps, enabling wide photodetection bandwidths of up to 300 GHz.[114] The fast response speed is explained by the short lifetime of the

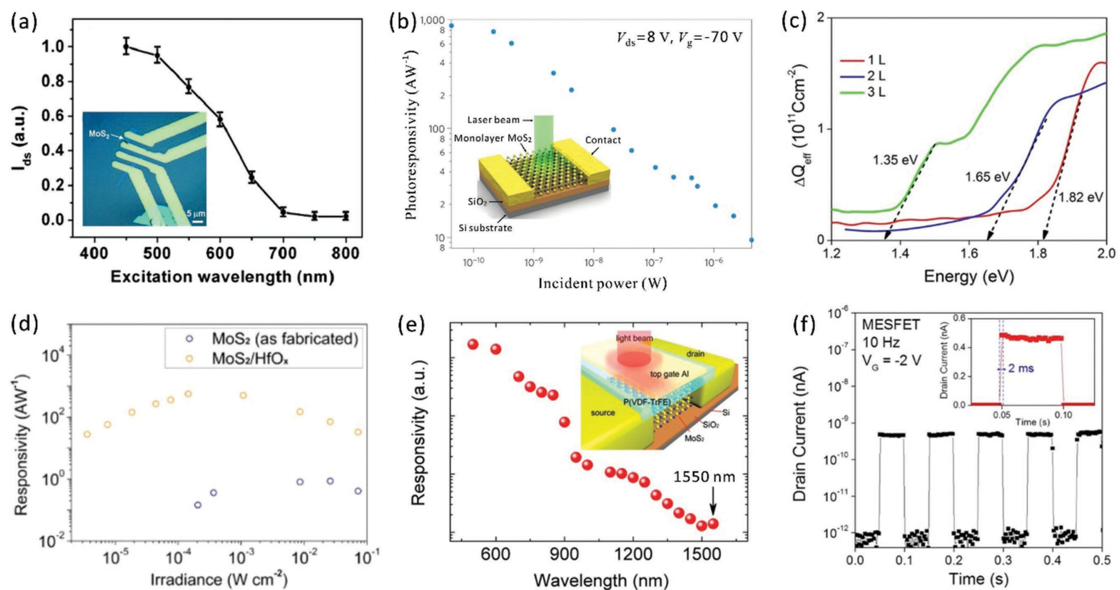

photoexcited carriers due to the dominant defect-assisted recombination.

Figure 2. a) Drain current (I_{ds}) of a single-layer MoS_2 phototransistor as a function of excitation wavelength of the illumination source at a constant optical intensity. Inset shows an optical image of a typical device made of single-layer MoS_2. Reproduced with permission.[88] Copyright 2012, American Chemical Society. b) Responsivity of a MoS_2 phototransistor as a function of incident power. Inset shows the 3D schematic view of the single-layer MoS_2 photodetector. Reproduced with permission.[89] Copyright 2013, Nature Publishing Group. c) Photon energy-dependent ΔQ_{eff} plots indicate the approximate optical energy gaps to be 1.35, 1.65, and 1.82 eV for triple-, double-, and single-layer MoS_2 nanosheets, respectively. Reproduced with permission.[90] Copyright 2012, American Chemical Society. d) Power-dependent responsivity before and after HfO_2 encapsula- tion of a bilayer MoS_2 phototransistor. Reproduced with permission.[106] Copyright 2015, American Chemical Society. e) Responsivity of a P(VDF-TrFE) polarization-gating triple-layer MoS_2 photodetector as a function of light wavelength from 500 nm to 1550 nm at V_{sd}=1 V and P=100 μW. Inset shows the 3D schematic view of the polarization-gating triple-layer MoS_2 photodetector. Reproduced with permission.[107] Copyright 2015, Wiley-VCH. f) Dynamic photoswitching behavior of a MoS_2 phototransistor with MESFET configuration. Reproduced with permission.[108] Copyright 2015, American Chemical Society.

Photo-Thermoelectric Effect in MoS_2. In addition to the photoconductive effect and photogating effect, the photo-thermoelectric effect has been found to contribute to the photoresponse process in a single-layer MoS_2 FET.[115] In this study, the authors examined the photoresponse of the FET with no external bias via scanning photocurrent microscopy (SPCM) measurements and found a strong and tunable photo-thermoelectric effect. An AFM image of the studied device is shown in **Figure 3**a. During the test, electrode 3 was connected to a current-to-voltage amplifier and the other electrodes were grounded. Under above- bandgap illumination, remarkable photocurrent was observed, even when the laser spot was focused inside the area of the electrodes (Figure 3b). To further clarify the origin of the photocurrent, they performed measurements under sub-bandgap illumination and demonstrated qualitatively similar photoresponse behavior with lower photocurrent values. These results clearly indicate that the photoresponse process is dominated by the photo-thermoelectric effect. The Seebeck coefficient S was determined by dividing the measured photo-thermoelectric voltage V_{PTE} by the temperature gradient, which can be estimated via a finite elements analysis calculation. Figure 3c shows the calculated S as a function of the gate voltage. Note that a negative value of S is expected for an n-type semiconductor. Evidently, the S of the single-layer MoS_2 reaches its maximum $\approx 3\times10^5$ μV K^{-1} in the electron depletion region and rapidly decreases by two to three orders of magnitude in the electron accumulation region, which is significantly larger than that of graphene (±4 to 100 μV K^{-1}).[115] The large and tunable S makes single-layer MoS_2 a promising material for applications such as on-chip thermopower generation waste thermal energy harvesting. In another work, Zhang et al. also found that the hot-carrier-assisted-photo-thermoelectric effect dominates the photocurrent generation in the

electron depletion region in a multilayer MoS_2 transistor with external bias, while the photovoltaic effect at the MoS_2-metal interface plays a major role in the electron depletion region.[116]

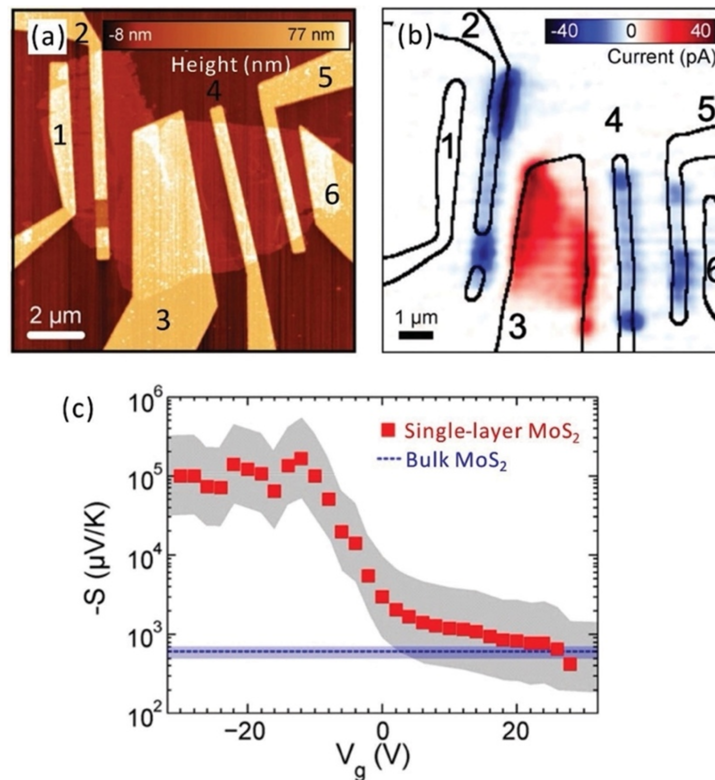

Figure 3. a) AFM image of phototransistors based on MoS2. b) SPCM map. The photocurrent (linear colorscale) is collected simultaneously with the intensity of the reflected light, which is used to detect the contour of the electrodes (solid black lines). c) Estimated Seebeck coefficient S versus gate voltage. The gray shaded area is the uncertainty in S due to the uncertainty in the estimation of the temperature gradient. (a–c) Reproduced with permission.[115] Copyright 2013, American Chemical Society.

3.1.2. Other TMDs

In addition to MoS_2, many other 2D layered TMDs have been explored for photodetection, including $MoSe_2$, WS_2, WSe_2, $MoTe_2$, HfS_2, ReS_2 and $ReSe_2$. In this section, we introduce photoconductors/phototransistors based on these 2D layered TMDs.

Single-layer $MoSe_2$ shows many appealing properties similar to those of single-layer MoS_2, such as a direct bandgap of ≈1.5 eV,[117] strong PL,[54] and a large exciton binding energy.[118] Rapid advances in preparing high-quality single- and few-layer $MoSe_2$ by mechanical exfoliation[119,120] or CVD techniques[121–123] have expanded the range of photodetection applications. For example, phototransistors based on CVD- grown monolayer $MoSe_2$ were reported by Chang et al.[124] and Xia et al.[125] with responsivities on the order of mA W^{-1}, several orders of magnitude lower than that of a device based on CVD-grown monolayer MoS_2.[95] However, fewer defects or charge impurity states within $MoSe_2$ compared to

MoS_2 give rise to much faster response times on the order of tens of milliseconds. The responsivity can be drastically increased to ≈93.7 A W^{-1} at the cost of reduced response speed by using CVD-grown multilayer $MoSe_2$ as a photoactive material, due to a large density of trap states within the bandgap of the $MoSe_2$.[126] Similarly, Abderrahmane et al. demonstrated a phototransistor made from exfoliated few-layer $MoSe_2$ with a thickness of ≈20 nm.[120] Their device reaches a maximum responsivity of up to 97.1 A W^{-1} near the threshold gate voltage and response times of tens of milliseconds.

Single- and few-layer WS_2 have been synthesized via various methods and employed in the field of photodetection.[127,128] Perea-López et al. have studied the photoresponse of CVD- grown few-layer WS_2, which is highly dependent on the photon energy from light excitation.[129] The device shows a low responsivity of ≈ 92 μA W^{-1} and a fast response speed of ≈5 ms. Afterwards, Huo and co-workers found that the photoresponse of exfoliated multilayer WS_2 is strongly dependent on the sur- rounding gaseous environment (**Figure 4**a).[130] The responsivity increases from tens of A W^{-1} in vacuum to a maximum of 884 A W^{-1} in an NH_3 atmosphere, which can be ascribed to the charge transfer between the physically absorbed gas molecules and the WS_2. This charge transfer modulates the WS_2 doping level and prolongs the lifetime of photocarriers, leading to an enhanced responsivity. A similar phenomenon in CVD-grown monolayer WS_2 was recently reported by Lan et al.[131] In this study, the device had a responsivity of 18.8 m A W^{-1} in vacuum, which is drastically reduced in air to 0.2 μA W^{-1}. Meanwhile, response times are on the order of subseconds in vacuum and less than 4.5 ms in air. More recently, centimeter-sized multi- layer WS_2 films tens of nanometers in thickness have been successfully prepared by pulsed-laser deposition[132] or magnetron sputtering techniques,[133] respectively. Photodetectors based on these films show decent responsivities between 0.51 A W^{-1} and 53.3 A W^{-1} with broadband photoresponses. Considering the facile and scalable fabrication processes, as well as the large- size, homogeneous, and transferable layered films obtained on various substrates, these preparation methods may open up new opportunities towards practical applications in the future.

Single- and few-layer WSe_2 have also demonstrated their potential in photodetection applications. Zhang et al. have studied the effect of metal contacts with different work functions on the photoresponse of CVD-grown monolayer WSe_2.[134] The device with Pd contacts reaches a maximum responsivity of up to ≈1.8×10^5 A W^{-1}, while the value decreases by several orders of magnitude for the device with Ti contacts in air. Interestingly, the response times for the device with Ti contacts are less than 23 ms, much faster than the Pt-contacted device (tens of seconds), as shown in Figure 4b. The significant variation in device performance is attributed to the large difference in Schottky barriers between the different metals and WSe_2, indicating the critical role of metal contacts in highly sensitive photodetectors. In another work, Pradhan and colleagues demonstrated a photodetector based on mechanically exfoliated tri-layer WSe_2 with responsivities of 7 A W^{-1} and fast response speed on the order of 10 μs.[135] Very recently, a WSe_2 photodetector with graphene electrodes that achieves a decent responsivity of ≈1.1

A W^{-1} was reported, suggesting good electrical contact between graphene and WSe_2.[136] Similarly, doping of few-layer WSe_2 can significantly affect its optoelectronic performance.[111,137] Specifically, Jo et al. demonstrated a high-performance WSe_2-based phototransistor, achieved by converting the conduction type from the p- to n-channel by triphenylphosphine (PPh_3) n-doping.[137] The responsivity of a device with Ti contacts increased by 160-fold, from 2.70×10^3 to 4.31×10^5 A W^{-1}, at a low light level upon doping. Further performance enhancement was attained by insertion of an h-BN layer underneath the WSe_2 channel, providing a charge-free environment that can greatly enhance the carrier mobility. Eventually, the device showed a responsivity as high as 1.27×10^6 A W^{-1} and fast response times of 2.8 ms.

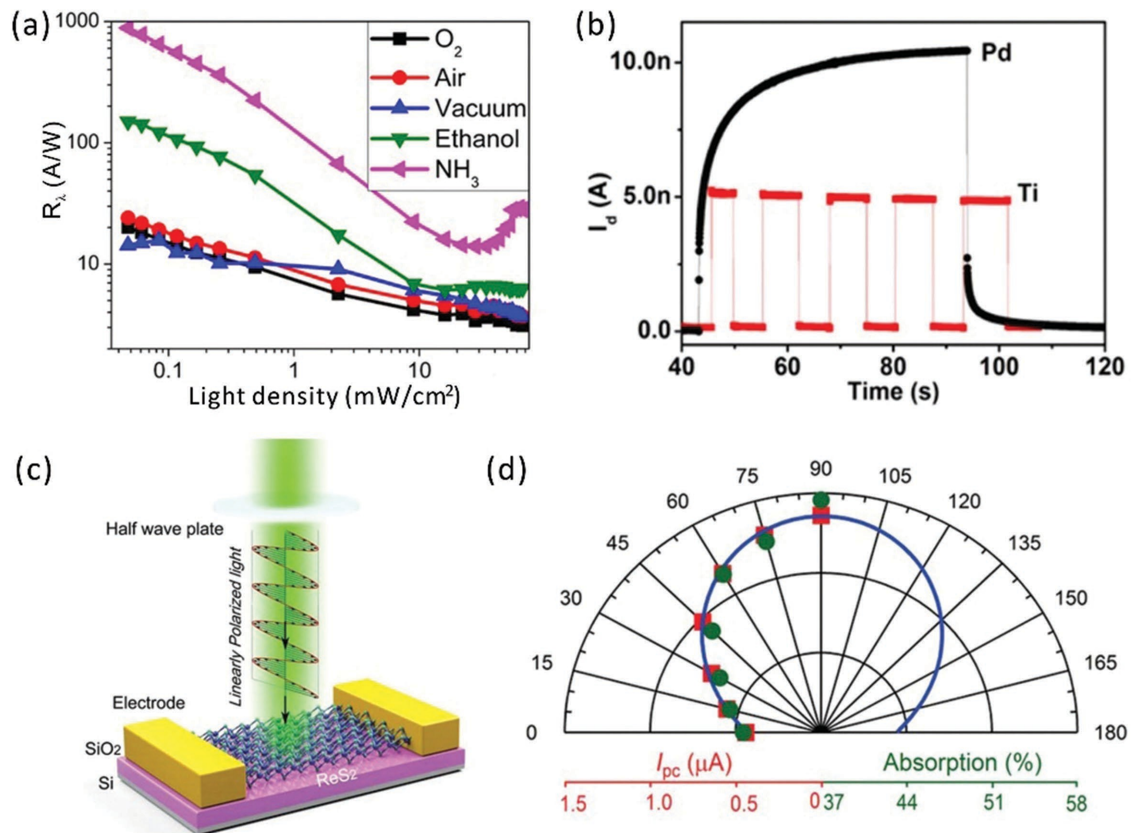

Figure 4. a) The responsivity R of a multilayer WS2 phototransistor as a function of light intensity under various gas atmospheres. Reproduced with permission.[130] Copyright 2014, Nature Publishing Group. b) Photoswitching behaviors of the Pd- and Ti-contacted WSe_2 photodetectors. Reproduced with permission.[134] Copyright 2014, American Chemical Society. c) 3D schematic view of an ReS_2 photodetection device. The light is illuminated on the ReS_2 channel, and the light polarization is controlled by the half wave plate. d) The photocurrent with drain bias of 1 V (red square) and absorption (green circle) measured under different polarization angle of green light and plotted in polar coordinates. The blue lines are the fitting results using sinusoidal function. The consistency between photocurrent and absorption indicates the intrinsic linear dichromic response of ReS_2. (c,d) Reproduced with permission.[147] Copyright 2016, Wiley-VCH.

Due to its outstanding optical and electrical properties, ultrathin $MoTe_2$, a recently introduced 2D material, has received much attention.[138–140] Yin et al. studied the influence of metal contacts on the electrical properties of a phototransistor based on mechanically exfoliated few-layer $MoTe_2$.[141] Under optimum conditions, the device reached a responsivity of up to 2560 A W^{-1}.

More recently, Xu and co-workers successfully isolated single- and few-layer HfS_2 flakes via mechanical exfoliation.[142] Experiments and theoretical simulations revealed that ultrathin HfS_2 is an indirect gap material with a bandgap of ≈2 eV. Moreover, they found that the electrical properties of the HfS_2-based phototransistors are greatly influenced by flake thickness and metal contacts. With optimized flake thickness, the responsivity reaches a maximum of ≈890 A W^{-1} in the transistor ON state with Au contacts and decreases tens of times with Ti contacts. Interestingly, the response times show strong back-gate dependence with distinct trends between the devices with different contacts. The different photoresponse behaviors are attributed to different Schottky barriers between the flake and the contacts, which are crucial to the separation and transportation of photocarriers.

Different from most layered TMDs with relatively high crystal symmetry, Re dichalcogenides, such as ReS_2 and $ReSe_2$, are anisotropic semiconductors crystallized in a distorted 1T in-plane structure.[143] Their extremely anisotropic electrical, optical, and mechanical properties render these compounds quite interesting for novel electronics and optoelectronics. Yang et al. found that the bandgap and carrier mobility of exfoliated $ReSe_2$ are highly modulated by their layer thickness, allowing the opportunity to engineer the electronic and optoelectronic properties of $ReSe_2$-based devices.[144] A phototransistor based on single-layer $ReSe_2$ shows a remarkable photoresponse with a responsivity reaching 95 A W^{-1} and fast response times on the order of tens of milliseconds. Similar to MoS_2 and WS_2 photodetectors,[94,95,130,131] the optoelectronic properties of the device are significantly influenced by the surrounding environment, which has also been found in a photodetector based on few-layer-Mo-doped $ReSe_2$ in another work.[145] This phenomenon is attributed to the charge transfer between $ReSe_2$ and gas molecules; this affects the doping level in $ReSe_2$ as well as the lifetimes of the photocarriers. A big disadvantage for the application of $ReSe_2$ in photodetectors is its poor air stability, which degrades its photodetecting performance. Therefore, passivation or encapsulation schemes for real-world applications are in high demand.

One particular case is illustrated by ReS_2, which maintains a direct bandgap of 1.5 eV irrespective of layer thickness. Both CVD-grown and exfoliated few-layer ReS_2 have been extensively explored as photodetectors, exhibiting responsivities ranging from 16.14 A W^{-1} to 8.86×10^5 A W^{-1}, and response times between several milliseconds to hundreds of seconds.[146–149] Such a huge variation in device performance can be attributed to three possible reasons: (i) different light absorption due to varied flake thicknesses, (ii) disparate gain enhancement depending on the density of trap states in the flakes prepared by different methods,

and (iii) diverse device architectures as well as different contact qualities. An obvious weakness of these devices is that the current normally cannot be recovered to their dark current levels after removing the illumination, due to a slow recombination rate of photocarriers. This issue can be addressed by the application of a short-gate voltage pulse, which actively purges the charge carriers to reset the device.[77] Specifically, the ReS_2 photodetector can be used to detect polarized light with high sensitivity, benefiting from the crystal structure anisotropy (Figure 4c and d).[147] Through electron doping by PPh_3 together with APTES, the responsivity of a ReS_2-based phototransistor can be drastically enhanced by several orders of magnitude, from 3.97×10^3 to 1.18×10^6 A W^{-1}.[150] The device also demonstrates broadband photodetection and fast response times on the order of tens of milliseconds. This improvement is explained by increased carrier mobility due to suppressed interfacial carrier scattering, in addition to reduced contact resistance at the metal-ReS_2 junction as a result of the n-doping effect and blocked charge puddle effect.

More recently, Shim et al. found that O_2 plasma treatment can significantly improve both the electronic and optoelectronic properties of a few-layer ReS_2 based transistor.[151] The maximum responsivity attained in this work is as high as 2.5 $\times10^7$ A W^{-1}, among the highest values achieved by 2D layered semiconductors with back-gated transistor geometry. The high responsivity is attributed to high absorption by the flakes due to their direct bandgap and relatively large thickness (≈30 nm). The response times are on the order of several to tens of seconds and decrease with prolonged plasma treatment duration, due to the trap states formed in the bandgap of ReS_2 at the surface region by the treatment. These trap states increase the photocarrier recombination rate and consequently reduce their lifetimes, leading to reduced response times.

In summary, photoconductors/phototransistors based on single- or few-layer TMDs show widely varied detection performances with responsivities ranging from $\approx10^{-7}$ A W^{-1} to $\approx10^7$ A W^{-1} and response times between 10^{-5} s to 10^3 s. Higher responsivities are obtained in devices where trap states exist in TMDs and/or at TMD/SiO_2 interfaces at the cost of slower response speeds. Moreover, performance is highly influenced by the TMD's layer number, preparation method, electrode contact qualities, and surrounding environment. Further improvement in device performance is achievable via various techniques, including the introduction of local- gated, ferroelectric-polarization-gated, or MESFET device geometries, encapsulation with an HfO_2 layer, or doping techniques

3.2. Group IIIA, IVA, IVB and Ternary Metal Chalcogenides

In addition to the TMDs discussed, other metal chalcogenides have been explored in the field of photodetection, including group IIIA metal (Ga, In) chalcogenides, group IVA metal (Ge, Sn) chalcogenides, group IVB metal (Ti, Zr, Ha) trichalcogenides, and ternary metal chalcogenides. In this section, photoconductors/phototransistors based on these metal chalcogenides are discussed and device performance is summarized in **Table 2**.

Table 2. Performance of photoconductors/phototransistors based on other 2D metal chalcogenides and few-layer BP. FL: Few-layer, ML: Multilayer, LN: liquid nitrogen, CVD: Chemical vapor deposition, NRs: Nanoribbons.

	Active layer	Spectral range	Responsivity [AW^{-1}]	Response times [ms]	Detectivity [Jones]	Ref.
GaS	Vapor-solid synthesized 3L	UV-visible	19.2	<30	10^{14}	[152]
	Mechanically exfoliated FL (in NH_3 atmosphere)	Visible	64.43	13	–	[156]
GaSe	Mechanically exfoliated FL	UV-visible	2.8	20	–	[153]
	Mechanically exfoliated ML (290 nm channel length)	Visible	5×10^3	10	–	[158]
	Vapor phase mass transport synthesized FL	Visible	1.7×10^{-2}	–	–	[159]
	Pulsed laser deposition synthesized ML	UV-Visible	1.4	10^4	–	[160]
	Vapor phase synthesized 1L	Visible	8.5	–	–	[161]
GaTe	Mechanically exfoliated 4L	UV-visible	274.4	48	10^{12}	[154]
	Mechanically exfoliated ML	Visible	$>10^4$	6	–	[155]
	Mechanically exfoliated ML (at LN temperature)	Visible	>800	300	–	[157]
	CVD-grown ML	UV-visible	0.03	54	–	[162]
In_2Se_3	Mechanically exfoliated 10L	UV-visible-NIR	3.95×10^2	18	2.26×10^{12}	[164]
	Physical vapor deposition-grown 1L	Visible	340	6	–	[165]
	Mechanically exfoliated ML	UV-visible-NIR	9.8×10^4	9×10^3	3.3×10^{13}	[166]
	Van der Waals epitaxy-grown ML	Visible	1.65×10^3	–	–	[167]
InSe	Mechanically exfoliated FL	Visible	3.47×10^{-2}	0.488	–	[168]
	Mechanically exfoliated FL	Visible-NIR	157	50	1.07×10^{11}	[169]
	Mechanically exfoliated ML	UV-visible-NIR	5.68×10^4	5	10^{13}	[170]
	Mechanically exfoliated FL (graphene electrodes)	Visible-NIR	60	0.1	–	[171]
	Mechanically exfoliated FL (avalanche photodetector)	Visible	–	8.7×10^{-2}	–	[172]
SnS_2	Mechanically exfoliated FL	Visible	100	44	–	[175]
	CVD-grown ML	Visible	8.8×10^{-3}	5×10^{-3}	2×10^9	[178]
	CVD-grown ML	Visible	100	22	–	[179]
	Van der Waals epitaxy-grown ML	Visible	1.19	<1	2.35×10^{11}	[180]
	Atmospheric pressure vapor deposition-grown ML	Visible	2	42	–	[181]
	Self-assembled synthesized FL	UV-visible-NIR	1.05×10^{-6}	400	–	[182]
$SnSe_2$	CVD-grown FL	Visible	1.1×10^3	14.5	1.01×10^{10}	[183]
	CVD-grown FL	NIR	1.9	$>10^5$	–	[184]
	Mechanically exfoliated 2L	Visible	0.5	2.1	–	[185]
GeS	Mechanically exfoliated ML	Visible	655	7	2.35×10^{13}	[187]
TiS_3	Mechanically exfoliated FL NRs	Visible-NIR	2.91×10^3	4	–	[196]
ZrS_3	Chemical vapor transport synthesized ML NRs	Visible-NIR	–	270	–	[197]
	Chemical vapor transport synthesized ML NRs network	Visible-NIR	7	<400	–	[198]
HfS_3	Chemical vapor transport synthesized ML NRs	Visible	0.11	<400	–	[199]
$ZrSe_3$	Chemical vapor transport synthesized ML NRs	Visible-NIR	0.53	<400	–	[200]
$HfSe_3$	Chemical vapor transport synthesized ML NRs	Visible	0.012	<400	–	[200]
$CuGaSe_2$	Solid-state reaction synthesized FL	UV-visible	103	100	8×10^{11}	[203]
$Pb_{1-x}Sn_xSe$	Van der Waals epitaxy-grown ML	UV-visible-NIR	5.95	740	–	[204]
$CuIn_7Se_{11}$	Mechanically exfoliated FL	Visible-NIR	0.38	24	–	[207]
$Sn(S_xSe_{1-x})_2$	Mechanically exfoliated FL	Visible	$>6 \times 10^3$	9	8.2×10^{12}	[208]
FL BP	Mechanically exfoliated FL	Visible-NIR	4.8×10^{-3}	1	–	[216]
	Mechanically exfoliated FL (in UV range)	UV-visible-NIR	9×10^4	$>10^5$	3×10^{13}	[218]
	Mechanically exfoliated FL (100 nm channel length, at low temperature)	Visible-NIR	4×10^7	<10	–	[219]
	Mechanically exfoliated ML	Visible-NIR	2×10^{-2}	–	–	[220]

3.2.1. Group IIIA (Ga, In) Metal Chalcogenides

Similar to TMDs, group IIIA metal chalcogenides are layered materials with weak van der Waals interactions between neighboring layers. In Ga chalcogenides with 1:1 stoichiometry suchas GaS, the atoms are arranged following the repeating unit S–Ga–Ga–S in the in-plane direction, which is different from single-layer TMDs. In the out-of-plane direction, the atoms are arranged in a graphene-like honeycomb

lattice.[152] The unique crystal structure leads to distinct band structures of the Ga chalcogenides, making them ideal candidates for photodetection.

Photodetectors based on exfoliated multilayer Ga chalcogenides, including GaSe,[153] GaS,[152] and GaTe,[154,155] have recently been realized on rigid or flexible substrates (**Figure 5**a). The GaSe-based device shows a responsivity of 2.8 A W^{-1} and a response speed of 0.02 s,[153] while the GaS-based devices made on SiO_2/Si and polyethylene terephthalate (PET) substrates show responsivities of up to 4.2 A W^{-1} and 19.2 A W^{-1} in the UV range, respectively (Figure 5b).[152] The detectivities achieved by the GaS-based devices are in the range of ≈10^{13}-10^{14} Jones (Figure 5b), surpassing commercial Si or InGaAs devices. Interestingly, the GaTe-based devices exhibit significantly increased responsivities between 274.3 A W^{-1} and 10^4 A W^{-1} and response speeds down to several milliseconds.[154,155] The much larger responsivities can be explained by the higher absorption coefficient and more efficient photoexcited electron–hole pair generation thanks to the direct bandgap of GaTe.[154,155] The photoresponse displays a sublinear dependence on the excitation intensity, indicating that the trap states presented in GaTe and/or at GaTe/substrate interfaces play a crucial role in the photocurrent response. Similar to TMDs,[94,95,130,131,144,145] the electronic/optoelectronic properties of 2D Ga chalcogenides are also sensitive to surface adsorbates such as moisture, oxygen molecules, and other gaseous molecules.[156] This offers the opportunity to improve the photoresponse in terms of responsivity, *EQE*, and response speed by employing the appropriate operating conditions. Moreover, Ga vacancies play a critical role in the electronic/optoelectronic properties of a phototransistor based on exfoliated GaTe.[157] By suppressing the thermally activated Ga vacancies at liquid nitrogen temperature in vacuum, the device exhibits an improved responsivity of as high as 800 A W^{-1} and a decreased response time. Recently, Cao et al. demonstrated significant enhancement in responsivity (up to 5000 A W^{-1}) by shrinking the electrode spacing distance to 290 nm in few-layer GaSe based photodetectors.[158] Their device shows response times on the order of tens of milliseconds, which can be further reduced to hundreds of micro-seconds by employing graphene electrodes. In addition, photo- detectors with regular responsivities between 0.017 A W^{-1} to 1.7 A W^{-1} have also been reported based on single- or few-layer Ga chalcogenides synthesized from other routes, including vapor phase mass transport (VMT),[159] PLD,[160] vapor phase deposition,[161] and CVD[162] methods.

Apart from Ga chalcogenides, In chalcogenides, including In_2Se_3[163–167] and InSe,[168–172] have also shown great promise in photodetection applications. The In_2Se_3 compounds have multiple structural phases (i.e., α, β, γ, δ, and κ) that affect their electronic and optoelectronic properties.[173] α-Phase In_2Se_3, one of the two common forms, has a direct bandgap of about 1.3 eV,[174,175] making it suitable for visible light harvesting in optoelectronics. Single- or few-layer α-In_2Se_3 flakes have been successfully synthesized on various substrates by van der Waals epitaxy.[163] A photodetector based on such a flake shows an efficient photoresponse with a responsivity of ≈2.5 A W^{-1}. Afterwards, Jacobs-Gedrim et al. demonstrated extraordinary photoresponse behavior from UV-visible to NIR regions in exfoliated α-In_2Se_3 with ≈10 nm thickness.[164] Their device has a responsivity as high as 3.95

$\times10^2$ A W^{-1}, fast response times on the order of tens of milliseconds, and a high specific detectivity of over 10^{12} Jones. The excellent photoresponse is believed to be attributed to the direct bandgap of In_2Se_3 and its large surface area-to-volume ratio, while the reduced carrier recombination as a result of the self-terminated/native-oxide-free surface leads to fast response. Zhou and colleagues have grown high- quality monolayer α-In_2Se_3 flakes via a physical vapor deposition (PVD) method and examined their optoelectronic properties.[165] A photodetector made from this flake demonstrates a similar photoresponse with the devices based on exfoliated ones, with a responsivity of 340 A W^{-1} and response times of ≈10 ms. Very recently, Island et al. have found that the photocurrent generation mechanism is a combination of the photoconductive effect and the photogating effect in isolated multilayer α-In_2Se_3.[166] The photoconduction is gate-independent, while photocurrent from the photogating effect can be strongly modulated with the back gate. Specifically, the dominant mechanism can be effectively tuned from fast conduction in the transistor OFF state to high gain photogating in the ON state via the back gate. The strong photogating effect is attributed to the long-lived states from intrinsic defects and native oxide at the In_2Se_3 flake surface, which trap photogenerated holes and effectively gate the flake with increased photocurrent. This strong photogating effect, along with the high absorption coefficient due to the direct bandgap of In_2Se_3, give rise to an extremely high responsivity of $\approx10^5$ A W^{-1} and an inferred detectivity of $\sim3.3\times10^{13}$ Jones in the In_2Se_3 phototransistor. Recently, Zheng et al. developed a method combining microintaglio printing with van der Waals epitaxy to efficiently pattern various 2D metal chalcogenides, including In_2Se_3 crystal arrays on mica substrates.[167] Precise control of the crystallization, thickness, position, orientation, and layout of patterned 2D crystals has been accomplished. In addition, the patterned In_2Se_3 crystal arrays can be integrated and packaged into flexible photodetectors with a prominent responsivity of ≈1650 A W^{-1}. This study has opened a new opportunity for batch fabrication and integration of photo-detectors, suggesting great promise for next-generation flexible, wearable, and integrated electronics and optoelectronics.

Different from other group IIIA metal chalcogenides, InSe has a direct bandgap of ≈1.3 eV in bulk form, while a direct-to-indirect transition occurs when reducing its thickness to a few nanometers.[176] Lei at al. demonstrated efficient photocurrent in exfoliated multilayer InSe with a varied number of layers under photoexcitation in the range of 400–800 nm.[168] The tail of the photocurrent vs wavelength spectra for a 10-layer InSe photodetector can be fit well with a parabola, suggesting the indirect nature of the bandgap in few-layer InSe. The device shows a responsivity of 34.7 mA W^{-1} and a fast response time of 488 μs. Subsequently, Tamalampudi and co-workers have fabricated phototransistors based on exfoliated few-layer InSe on both rigid SiO_2/Si and bendable PET substrates.[169] Their devices show broadband photoresponses from the visible to NIR region with responsivities of ≈10 A W^{-1} (Figure 5c), which can be improved significantly to 157 A W^{-1} with a back-gate voltage. The photocurrent increases sublinearly with the incident excitation (Figure 5c) while the response time is increased to several seconds. This indicates that long-lived trap states caused by the defects and/or charged impurities in InSe and the

adsorbed molecules at the $InSe/SiO_2$ interface play an important role in the photoresponse. Recently, Feng et al. discovered that multiple reflection interference at the interfaces in multilayer InSe phototransistors leads to a channel-thickness-dependent photoresponse based on both theoretical simulations and experimental results.[170] With an optimal InSe thickness of ≈30 nm, they demonstrated a high responsivity of up to $\approx 5.6\times 10^4$ A W^{-1} and a detectivity above 10^{13} Jones in spectra ranging from UV-visible to NIR. The device also showed fast response times on the order of several milliseconds. Specifically, the response times of few-layer-InSe-based photodetectors can be dramatically reduced from several milliseconds to 120 μs by using graphene electrodes, as reported by Luo and colleagues.[171] The much-improved response speed is attributed to the smaller Schottky barrier between InSe and graphene as well as the high mobility of graphene, which facilitates fast transportation of photocarriers. They also demonstrated effective modulation of the photocurrent and response times via the back-gate voltage because the work function of the two materials can be easily regulated by the gate voltage, leading to a tunable Schottky barrier. More recently, the avalanche effect, which can induce carrier multiplication to greatly enhance the photoresponse, has been realized in few-layer InSe. This effect was triggered by exploiting the large Schottky barrier between the InSe and Al contacts to enable the application of a large bias voltage.[172] Thanks to carrier multiplication, the device reaches an *EQE* of 334% with an avalanche gain of 47 at a moderate voltage range before reverse bias breakdown, while the values increase to 1110% and 152, respectively, at the voltage range where reverse bias breakdown occurs. The large Schottky barrier also reduces the dark current to picoamp scale, enabling a large single to noise ratio (*SNR*) on the order of tens of decibels. The photodetector shows a fast response time of 60 μs, about two orders of magnitude faster than a back-gated InSe photodetector with a similar photoresponse level. Further integration of plasmonic nanoantennas based on an Al disk can greatly enhance the photoresponse of the device to improve the *EQE* by approximately 8 times. The authors also found that the photocurrent increases significantly in the wavelength range of 650–750 nm beyond the scattering peak of Al nanodisks, which is associated with the electron emission from the Fermi level of the Al into InSe. Three different processes can account for this improvement: For one, the plasmonic nanodisks can provide a local electromagnetic field enhancement that contributes to carrier generation in InSe. On the other hand, the decay of the surface plasmons of the nanodisks produces hot electrons, and those with sufficient energy to overcome the Al–InSe Schottky barrier can provide additional photocarriers. Third, electrons emitted over the Schottky barrier can be accelerated to a high kinetic energy, further contributing to the avalanche process.

3.2.2. Group IVA (Ge, Sn) Metal Chalcogenides

In addition to the TMDs and group IIIA metal chalcogenides discussed, there is a growing interest in photodetection based on ultrathin group IVA metal chalcogenides, including SnS_2,[177–182] $SnSe_2$,[183–185] GeSe,[186] and GeS,[187] for their unique electronic structures and physical properties. In addition, this group

of semiconductors is made up of earth-abundant and environmental-friendly elements with prominent chemical stability, making them particularly attractive for practical applications.

Tin dichalcogenides SnS_2 and $SnSe_2$ are isostructural with the hexagonal cadmium iodide (CdI_2)-type structure and exhibit indirect bandgaps of ~2.2 eV and ~1.0 eV in bulk, respectively.[188,189] Both semiconductors have recently attracted much attention in the field of photodetection. For example, single- and few-layer SnS_2 flakes have been successfully exfoliated and employed in transistors and photodetectors.[177] Experiments and theoretical calculations show that the indirect bandgap nature remains in SnS_2 even with thickness down to a monolayer. A device with a flake of ≈10 nm thickness reaches a high responsivity of ≈100 A W^{-1}. Similar to MoS_2-based phototransistors,[92] the photoresponse contains two components, i.e., a slow component with response times on the order of several to tens of seconds and a fast component with response times on the scale of tens of milliseconds. The slow and fast components are likely due to a combination of long-lived extrinsic traps, such as adsorbates at the SnS_2 surface and SnS_2/SiO_2 interface, as well as defect states in SnS_2. Photodetectors based on ultrathin SnS_2 prepared by other methods, including CVD,[178–180] atmospheric pressure vapor deposition (APVD),[181] and self-assembled syn-thesis[182] have also been realized on rigid or flexible substrates and reach significantly varied responsivities from ≈0.2 mA W^{-1} to ≈100 A W^{-1}. Specifically, ultrathin SnS_2 crystal arrays can be grown by a CVD method via seed engineering, and photodetectors composed of these crystals have fast response times of 5 μs, as shown in Figure 5d.[178] Importantly, the performance of phototransistors is highly sensitive to the density of sulfur vacancies in SnS_2. Through temperature-dependent electrical transport measurements together with theoretical calculations, Huang et al. have verified that sulfur vacancies generated in the growth process can induce defect levels near the bottom of the conduction band of SnS_2.[179] Accordingly, the photoresponse of a SnS_2-based phototransistor can be significantly improved by diminishing the sulfur vacancies, as reported by Yang and co-workers recently.[180] Through sulfur annealing treatment, their device achieves an 30-fold improvement in the photoswitching ratio, with dark current suppressed by several orders of magnitude and response times reduced by more than 3 orders of magnitude to less than 1 ms.

Zhou et al. have recently synthesized single-crystalline $SnSe_2$ flakes with thicknesses down to ≈1.5 nm via an improved CVD method.[183] Their experiments revealed that few-layer $SnSe_2$ with a thickness of ≈10 nm exhibits an indirect bandgap of ≈1.73 eV. A photodetector composed of the flake reaches a high responsivity of ≈1.1×10^3 A W^{-1} and fast response times of ≈10 ms. Another work by Huang et al. demonstrated the synthesis of $SnSe_2$ nanosheets with diverse shapes and thicknesses varying from ≈10 nm to ≈150 nm.[184] Photoresponse measurements on a ≈20 nm-thick nanosheet showed a responsivity of ≈1.9 A W^{-1} and a current on/off ratio of ≈100. More recently, Yu and colleagues successfully exfoliated ultrathin 1T-phase $SnSe_2$ flakes with various layer numbers from bulk single crystals and probed their optoelectronic properties.[185] Their device gave an

evident photoresponse with a decent responsivity of 0.5 A W^{-1} and a fast response time of down to ≈2 ms.

Group IVA chalcogenides with 1:1 stoichiometry, such as GeS, GeSe, SnS, and SnSe, are important p-type semiconductors with a layered crystal structure and an atom arrangement resembling the distorted NaCl structure.[190] These compounds have both indirect and direct bandgaps in the range of 0.90–1.65 eV, rendering them promising absorbers in the visible to NIR spectral region.[191,192] Single-crystal GeSe nanosheets with thicknesses of ≈300 nm have been successfully synthesized via a solution-phase method and employed in photodetectors.[186] The device in this work shows a remarkable photo- response with an obvious anisotropic on/off switching ratio in directions parallel and perpendicular to the layer, attributed to the large bonding anisotropy of the layered crystal structure. Recently, Ulaganathan et al. have isolated multi-layered GeS flakes having ~28 nm thickness and applied them as channel materials in phototransistors.[187] Their device reached a responsivity of ≈206 A W^{-1}; this value was further increased to as high as ≈655 A W^{-1} when the transistor was operated in the ON state.

3.2.3. Group IVB (Ti, Zr, Hf) Metal Trichalcogenides

In this section, we review photodetectors based on ultrathin group IVB metal trichalcogenides, such as TiS_3, ZrS_3, HfS_3, $ZrSe_3$, and $HfSe_3$. These trichalcogenide compounds possess direct or indirect bandgaps between ~1.0 eV to ~3.1 eV, covering the UV to NIR region.[193–195] Island et al. have successfully isolated few-layer TiS_3 nanoribbons (NRs) with thicknesses down to 10–30 nm via mechanical exfoliation during the transfer process of NRs and probed their photoresponses.[196] Their device showed a broad photoresponse with a detection range up to 940 nm (Figure 5e), a high responsivity of 2910 A W^{-1}, and fast response times on the order of several milliseconds. The photocurrent increased sub- linearly with respect to incident power; together with decreased responsivity with increasing power, this suggests that long-lived trap states played a crucial role in the photoresponse.

In another work, Tao and co-workers transferred a network of ZrS_3 NRs onto a flexible substrate such as polypropylene or paper and used it in a photodetector.[197] The ZrS_3 NRs with thicknesses of ≈70 nm were synthesized via a chemical vapor transport (CVT) method. The fabricated devices exhibited a remarkable photoresponse in the range of visible to NIR and response times of tens of seconds. Afterwards, Tao et al. examined the photoresponse of phototransistors based on single or several ZrS_3 NRs.[198] Both devices exhibited responsivities on the order of tens of A W^{-1} and response times below 0.4 s, which were superior to those attained from the device based on the network of ZrS_3 NRs.[197] In addition, HfS_3, $ZrSe_3$, and $HfSe_3$ NRs have also been synthesized by CVT methods, as reported by Xiong and colleagues.[199,200] Photodetectors made from these single NRs demonstrated impressive photoresponses, with responsivities between 12 mA W^{-1} and 530 mA W^{-1} and response times of less than 0.4 s.

3.2.4. Ternary Metal Chalcogenides

Recently, ternary 2D semiconductors, which offer multiple degrees of freedom for

controlling their physical properties via stoichiometric alteration, have stimulated much research interest in many fields.[201,202] This emerging class of new 2D materials has also been employed in photodetection applications.[203–205] For example, ternary copper indium selenide (CuInSe) with a Cu:In ratio between 1:5 to 1:7 (i.e., γ-phase) is a layered compound.[206] Lei et al. reported successful exfoliation of few-layer $CuIn_7Se_{11}$ flakes and employed them in photodetection and photovoltaic applications.[207] Their photodetector with metal-semiconductor-metal (MSM) configuration gave a strong photoresponse throughout the visible range spectrum, with a responsivity of 380 mA W^{-1}. Fitting the tail of the photo-response vs incident photon energy spectra indicated that the $CuIn_7Se_{11}$ with 3-4 layers had an indirect bandgap of ~1.1 eV, while the value rose to ≈1.4 eV for those with 1-2 layers. Due to the Schottky barrier between the $CuIn_7Se_{11}$ and metal contacts, the device exhibited a low dark current of ≈1 pA, giving rise to a noise level down to $\approx 1.3\times10^{-29}$ A^2 and a high *SNR* of 95 dB.

In another work, Perumal and co-workers fabricated photo- transistors on both rigid and flexible substrates based on exfoliated few-layered $Sn(S_xSe_{1-x})_2$ flakes with thicknesses of ≈6 nm and examined their photoresponses.[208] The device on the rigid substrate showed a prominent photoresponse with a high responsivity of up to 6000 A W^{-1} (Figure 5f), fast response times of ≈9 ms, and a detectivity exceeding 8×10^{12} Jones. Notably, their flexible device demonstrated good optoelectronic properties and excellent bending stability. These studies emphasize ternary 2D layered semiconductors as highly promising platforms for novel photodetection applications.

In summary, photodetectors based on these metal chalcogenides show responsivities (0.2 mA W^{-1} to 5.6×10^4 A W^{-1}) and response times (5 μs to tens of seconds) comparable to those exhibited by TMD-based devices. Moreover, the wide range of bandgaps available from these metal chalcogenides enables their operation in a broad spectrum ranging from the UV-visible to NIR region. Element vacancies can significantly affect the photoresponses of detectors. Further improvement of the response speed is achievable by using graphene electrodes to reduce Schottky barriers at the contacts and facilitate fast photocarrier transportation. In addition, ternary metal chalcogenides can afford multiple degrees of freedom to regulate their optoelectronic properties, suggesting new platforms for novel photodetection applications.

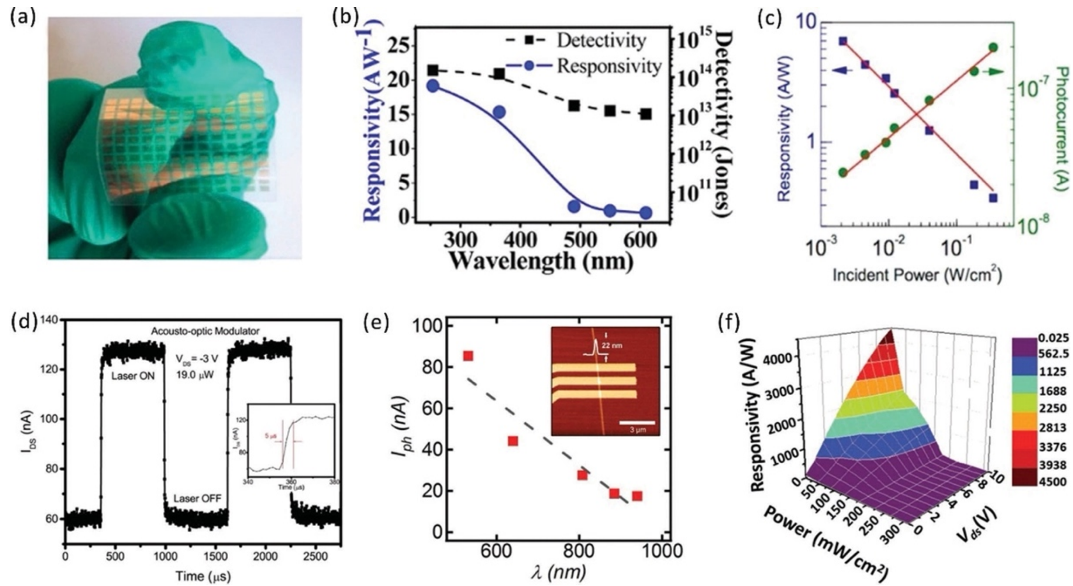

Figure 5. a) GaS nanosheet photodetectors on a flexible PET substrate. b) Wavelength-dependent responsivity and detectivity of the flexible GaS photodetector under 0.5 mW/cm^2 irradiance at a bias voltage of 2 V.) a,b) Reproduced with permission.[152] Copyright 2013, American Chemical Society. Photocurrent (green solid dots) and responsivity (blue solid squares) of an InSe phototransistor as a function of illumination intensity at V_{ds} = 10 V and V_g = 0 V. The power laws of $R \approx P^{-0.56}$ and $I_{ph} \approx P^{0.41}$ were determined from fitting the measured data. Reproduced with permission.[169] Copyright 2014, American Chemical Society. d) Drain-source current I_{DS} of an SnS_2 photodetector recorded as a function of time with a sampling rate of 660 kHz when the laser beam was modulated periodically at a frequency of ≈800 Hz via an acousto-optic modulator (with the laser beam only partially deflected). Reproduced with permission.[178] Copyright 2015, American Chemical Society. e) Photocurrent of a TiS_3 NR photodetector measured as a function of different laser wavelengths. By linearly extrapolating (dashed line) the photocurrent vs. excitation wavelength data, the bandgap energy is estimated to be 1.2 eV (1010 nm). Inset shows an AFM image of the device with electrodes spaced by 500 nm. The width of the TiS_3 NR is 195 nm. Reproduced with permission.[196] Copyright 2014, Wiley-VCH. f) 3D view of responsivity mapping of a few-layered $Sn(S_xSe_{1-x})_2$ phototransistor. Reproduced with permission.[208] Copyright 2016, Wiley-VCH.

3.3. Few-layer Black Phosphorus

Black phosphorus (BP), a stable layered allotrope of phosphorous, is an elemental p-type semiconductor with a direct bandgap of 0.35 eV and mobilities on the order of 10 000 cm^2 V^{-1} s^{-1} in bulk form, and has been studied from the 1980s.[209] At ambient conditions, orthorhombic BP forms puckered layers held together by weak interlayer forces with significant van der Waals character[210,211] and can be easily isolated into thin layers. Unlike its bulk form, few-layer BP shows ambipolar transport behavior with mobilities up to 1000 cm^2 V^{-1} s^{-1}.[25] Meanwhile, due to the reduced symmetry in the puckered-layer structure, few-layer BP has been found to possess remarkable in-plane anisotropic electronic, optical, and phonon properties.[25,212–215] Previous studies have predicted that the direct bandgap of few-layer BP depends strongly on the number of layers and the in-layer strain,

where the value increases to over 1 eV for a single layer.[33,34] Thus, the narrow bandgap renders few-layer BP an appealing candidate for NIR photodetection (Table 2), complementing the detection gap between zero-bandgap graphene and large-bandgap TMDs.

Buscema et al. studied the performance of detectors composed of few-layer BP having 3–8 nm thickness as a function of excitation wavelength, power, and frequency.[216] The device gave a remarkable photoresponse to excitation wavelengths from the visible region up to 940 nm (**Figure** 6a) and demonstrated a responsivity of 4.8 mA W^{-1} and fast response times of several milliseconds. Both the photovoltaic effect and photo thermoelectric effect have been found to contribute to photocurrent generation in ultrathin BP photodetectors.[217] In this study, the authors performed scanning photocurrent measurements on a transistor based on an 8 nm thick, few-layer BP as a function of polarization and gate voltages. They found that photogenerated electron–hole pairs were separated by a built-in electric field at Schottky barriers induced by the Fermi level alignment in the transistor OFF state. In addition to the photovoltaic effect, while in the ON state, the reduced contact resistance allowed the photo-thermoelectric effect to contribute to the photocurrent. The Seebeck coefficient of few-layer BP was estimated to be ≈100 V K^{-1} at 77 K, which reduces to ≈5 V K^{-1} with negative gate voltages. In addition, operating with the photovoltaic effect in the OFF state, the device showed a strong polarization-dependent photocurrent response, arising from the directional dependence of the interband transition in the anisotropic band structure of BP.

Recently, Wu et al. examined the optoelectronic properties of few-layer-BP-based photodetectors over a wide spectrum from UV to NIR (310 to 950 nm).[218] Interestingly, the device demonstrated two distinct photoresponse behaviors in the low-energy range (visible–NIR region, 400–950 nm) and high energy range (near-UV region, below 400 nm). As shown in Figure 6b, the responsivity reaches its highest value of 9×10^4 A W^{-1} in the near-UV region and decreases by several orders of magnitude, down to ≈1.82 A W^{-1}, in the visible–NIR region. The corresponding response speed changes from tens of seconds to several milliseconds in the high-energy and low-energy wavelength regions. The detectivity achieved by this device in the near-UV region is as high as ≈ 3×10^{13} Jones. This colossal UV responsivity is attributed to the resonant interband transition between two specially-nested valence and conduction bands, which provides an unusually high density of states for highly efficient UV absorption due to the singularity in the joint density of states.

The responsivity of few-layer BP phototransistors can be further improved by lowering the working temperature and scaling down the channel length. For example, Huang et al. have exfoliated few-layer BP flakes with thicknesses of ≈8 nm onto SiO_2/Si substrates and defined source/drain electrodes with various channel lengths, followed by the deposition of Ni/Au metal contacts.[219] The photocurrent of the BP transistor with a 1 μm channel increased significantly with decreasing working temperature from 300 K to 20 K in a broad wavelength range in the p-channel of the transistor, giving rise to the highest responsivity, ~7×10^6 A

W^{-1} at 20 K, and a much lower responsivity of ~6.7×10^5 A W^{-1} at 300 K (Figure 6c). The increased responsivity was attributed to the improved carrier generation-recombination rate and better carrier transport due to the freezing of interface and bulk traps, as well as the reduced phonon scattering. Further scaling of the channel length down to 100 nm led to a much-improved responsivity of up to $\approx4\times10^7$ A W^{-1} at 20 K and $\approx4.3\times10^6$ A W^{-1} at 300 K (Figure 6c) due to a larger transverse electric field and smaller carrier transit times in shorter channel devices.

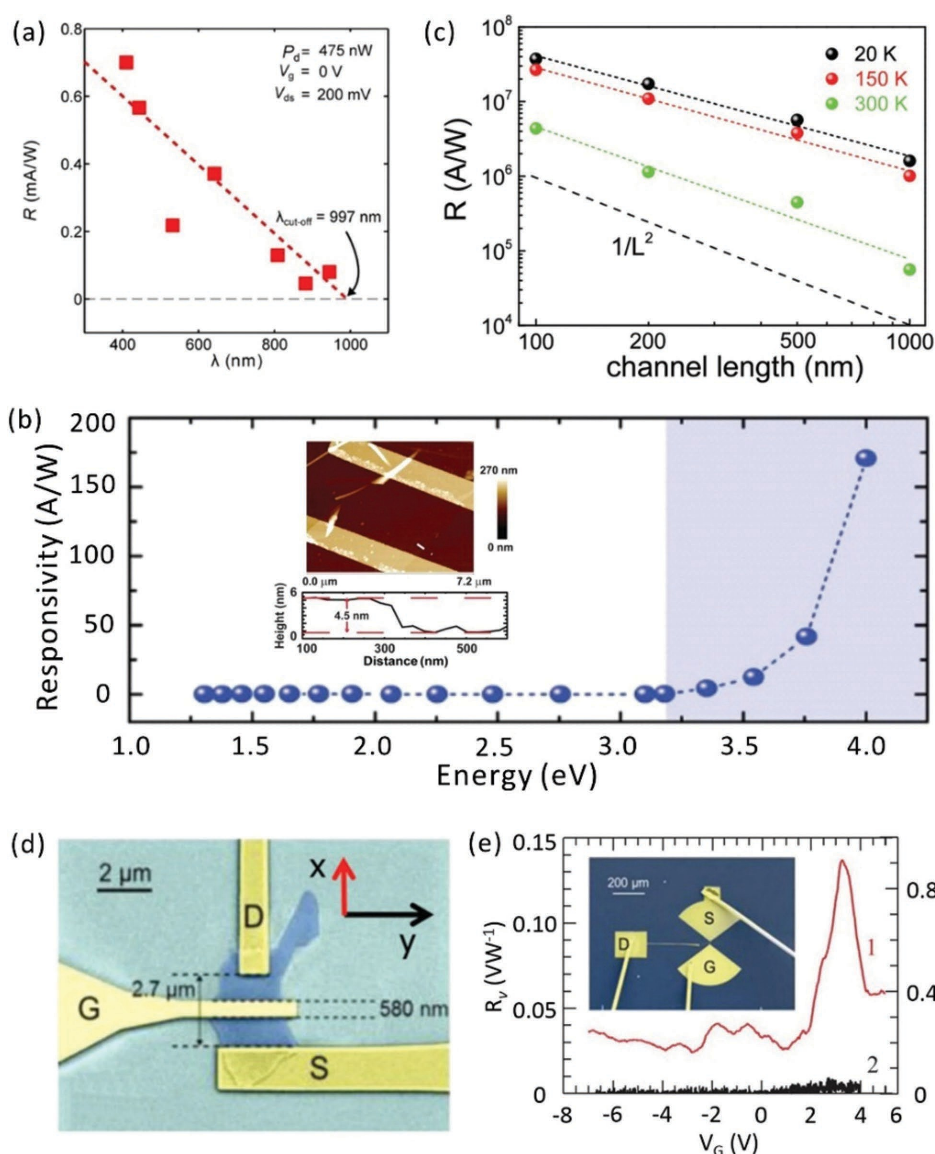

Figure 6. a) Responsivity of a few-layer BP photodetector versus excitation wavelength at a constant power (red squares). Reproduced with permission.[216] Copyright 2014, American Chemical Society. b) Responsivity of a few-layer BP phototransistor within the energy range 1–4 eV measured at V_{BG} = 80 V and V_{SD} = 0.1 V. Inset shows AFM scan across the channel area of the device showing the thickness of the black phosphorus flake to be ≈ 4.5 nm. Reproduced with permission.[218] Copyright 2015, American Chemical Society. c) Responsivity of few-layer BP phototransistors with different channel lengths under the same driving voltage (V_g = -20 V, V_d =1 V). Reproduced with permission.[219] Copyright

2016, Wiley-VCH. d) SEM image of a BP-based THz detector. e) Gate bias dependence of the responsivity (*RV*) and photovoltage (Δu) at room temperature for the BP THz detector. The red line (curve 1) was measured by impinging the THz beam on the detector surface; the black line (curve 2) was measured while blanking the beam with an absorber. Inset shows the antenna-coupled structure. (d,e) Reproduced with permission.[221] Copyright 2015, Wiley-VCH.

High-performance few-layer-BP-based photodetectors have been used for imaging applications. Engel et al. reported thata photodetector based on 120 nm few-layer BP could acquire images with high resolution both in the visible and IR spectral regions.[220] The device was operated with the photo-thermoelectric effect. The test object was raster scanned with respectto a tightly focused laser beam with a wavelength of 532 nmor 1550 nm, and the reflected light signals were received by the BP photodetector and converted into electrical currents for imaging formation.

Few-layer BP also shows great promise in THz detection. A room-temperature THz detector based on 10 nm thick few-layer BP was recently reported.[221] The device structure with asymmetric antennas-coupled few-layer BP FET is shown in Figure 6d. A few-layer BP flake was mechanically exfoliated onto a SiO_2/Si substrate as the active layer of the FET. Source- drain contacts patterned by e-beam lithography and metal deposition were oriented along the armchair (x) BP axis. The channel length was ≈2.7μm and the gate length was ~580 nm. An 80 nm-thick SiO_2 insulating layer was deposited on the sample by sputtering, followed by patterning of the gate electrode on the oxide. The source and gate electrodes were in the shape of two halves of a planar bow-tie antenna, with a total length of 500 μm and a flare angle of 90 ° for coupling THz radiation (inset in Figure 6e). By keeping the source electrode grounded, the photoresponse (voltage response) was recorded at the drain electrode in an open circuit configuration through a lock-in amplifier connected to a low-noise voltage preamplifier. The detection mechanism was attributed to the combination of the rectification of THz-induced overdamped plasma waves in the BP channel and the photo-thermoelectric effect. The generated voltage response was sensitive to boththe frequency of the impinging radiation and the gate voltage. The detector reached a maximum voltage response of ≈0.9μV, giving rise to the maximum responsivity of 0.15 V W^{-1} under 0.298 THz radiation at room temperature (Figure 6e). Moreover, a lower limit for NEP, ≈40 nW $Hz^{-1/2}$, has been achieved, which is comparable to that of the best bilayer graphene-based THz photodetectors.

However, despite these aforementioned achievements, a huge challenge that impedes the application of few-layer BP in electronics/optoelectronics is its environment-induced degradation.[26] Exfoliated flakes are highly hygroscopic and tend to condense moisture from the air on their surface, which likely leads to the degradation of BP. Therefore, it is necessary to develop passivation or encapsulation techniques in the future for practical applications.

3.4. Hybrid Phototransistors

Ultrasensitive photodetectors operating at very low light intensities require a gain mechanism by which one incident photon can induce multiple carriers to conduct the current in the devices. A promising strategy is based on hybrid phototransistors that function with the photogating effect, where light is efficiently absorbed by appropriate sensitizing centers while photogenerated electrons or holes can transfer into conducting channel and recirculate many times within the lifetimes of the opposite charges.[77,78] According to their work principles, hybrid phototransistors based on 2D layered semiconductors can be classified into two types. The first is based on devices in which 2D layered semiconductors only serve as light absorbing media. In these devices, graphene is normally employed as the conducting channel material for its high carrier mobility (hence a low carrier transit time) and strong sensitivity of its conductance to electrostatic perturbation by adjacent photocarriers. Another type of hybrid phototransistor contains active materials, i.e., 2D layered semiconductors serve as both light absorbers and conducting media while other sensitizers are used to enhance light absorbance or to extend the detection range. The performances of these devices are summarized in **Table 3**.

Table 3. Performance of hybrid phototransistors based on 2D layered semiconductors. ML: Multilayer, Gr: Graphene, FL: Few-layer, IGZO: Indium gallium zinc oxide, QDs: Quantum dots, CIS: Copper indium sulfide.

	Active layer	Spectral range	Responsivity [AW^{-1}]	Response times [s]	Detectivity [Jones]	Ref.
Type 1	ML MoS_2/1L Gr (at low temperature)	Visible	1×10^{10}	Tens of seconds	–	[222]
	1L MoS_2-1L Gr	Visible	1.2×10^{7}	Tens to hundreds of seconds	–	[223]
	FL MoS_2-1L Gr	Visible	10	0.28	–	[224]
	FL MoS_2-1L Gr (at zero bias)	Visible	3.0	1.3×10^{-4}	–	[225]
	1L MoS_2-1L Gr	Visible	1.3×10^{4}	–	–	[226]
	1L MoS_2-IGZO	UV-visible-NIR	1.7	Tens of seconds	–	[227]
	ML Bi_2Te_3-1L Gr	Visible-NIR	35	8.7×10^{-3}	–	[228]
	FL InSe-1L Gr	Visible	940	–	–	[229]
Type 2	FL MoS_2-PbS QDs	Visible-NIR	6×10^{5}	0.35	5×10^{11}	[230]
	FL MoS_2-PbSe QDs	NIR	1.9×10^{-6}	0.25	–	[231]
	ML MoS_2-Gr QDs	Visible	1.6×10^{4}	0.07	–	[232]
	FL SnS_2-CIS QDs	Visible	630	<0.1	–	[233]
	1LMoS_2-rhodamine 6G	Visible-NIR	1.17	5.1×10^{-6}	1.5×10^{7}	[234]
	ML MoS_2-rubrene	Visible	0.326	–	–	[235]
	WS_2-$CH_3NH_3PbI_3$ perovskite	Visible	17	2.7×10^{-3}	2×10^{12}	[236]
	APTES-doped FL MoS_2-$CH_3NH_3PbI_3$ perovskite	Visible	1.94×10^{6}	Several seconds	1.29×10^{12}	[237]

Examples of light-absorbing media in the first type of hybrid device are MoS_2,[222–227] Bi_2Te_3,[228] and InSe.[229] Due to their strong light absorption and tunable bandgaps, these devices are capable of achieving high gains with a detection range spanning from the UV to NIR region. In 2013, Roy et al. reported a hybrid phototransistor that consists of a monolayer graphene over a multilayer MoS_2, both of which were exfoliated from their bulk crystals, respectively.[222] A very high responsivity of 5×10^{8} A W^{-1} was obtained in the devices at room temperature and increased to 1×10^{10} A W^{-1} at 130 K (**Figure 7**a), while the response times were very slow (approximately tens of seconds). The device also demonstrated an ultrahigh gain of $\approx4\times10^{10}$. The high performance is attributed to several different processes. Under illumination, photoexcited holes generated inside the MoS_2 are trapped by

localized states in the MoS_2, while photoexcited electrons are transferred to the graphene channel under the influence of a gate electric field (Inset in Figure 7a, top-right panel). These electrons recombine with holes induced by the negative gate bias in the channel and increased channel resistance, giving rise to a large net photocurrent. Meanwhile, the trapped holes reside longer in the MoS_2 and act as a local gate, leading to strong photogating effect on the graphene channel through capacitive coupling. The long lifetimes of holes were also responsible for the large response times. Afterwards, Zhang and co-workers demonstrated a hybrid photodetector composed of a CVD-grown single-layer MoS_2 covered by a CVD-grown graphene monolayer, which also showed a high responsivity of $\approx 1.2\times10^7$ A W^{-1} and a gain up to 10^8.[223] Similarly, the device showed very slow response times ranging from tens to hundreds of seconds. Compared with the value reported by Roy et al.,[222] the relatively lower responsivity achieved in this work is likely due to the lower carrier mobility in CVD graphene. However, CVD graphene and MoS_2 are more conveniently prepared with large area and are therefore more suitable for practical applications. As shown in Figure 7b, the I_{ds}–V_g curves shift horizontally with increasing incident powers, which undoubtedly confirms that the sensing mechanism is dominated by the photogating effect. It is noteworthy that the device performance decreases significantly when measured in high vacuum, which is attributed to the decreased effective electric field at the graphene/MoS_2 interface due to the desorption of adsorbates and/or charged impurities in vacuum.

Graphene covered with other 2D layered materials such as Bi_2T_3[228] and InSe[229] also exhibited a pronounced photogating effect. However, the devices showed inferior responsivities between 35 A W^{-1} and 940 A W^{-1}. In particular, Qiao et al. reported a hybrid photodetector that consists of monolayer graphene covered with epitaxially-grown B that consists of monolayer graphene covered with epitaxially-grown Bi_2Te_3 nanoplates. The device shows an obvious photoresponse with a detection range extending to the NIR (980 nm) and a telecommunication band (1550 nm) (Figure 7c) due to the small bandgap of Bi_2Te_3.[228]

In the second type of hybrid device, the sensitizers that are employed to enhance light absorbance or to extend the detection range are normally quantum dots (QDs),[230–233] organic molecules,[234,235] and $CH_3NH_3PbI_3$ perovskite.[236,237] For example, Kufer et al. reported a hybrid photodetector composed of bilayer MoS_2 covered with 1,2-ethanedithiol ligands and (EDT)-capped colloidal PbS QDs.[230] The short ligands capped on the surface of the QDs are crucial to the photodetection performance due to the improved charge transport of the QDs' film and charge transfer between the QDs and MoS_2. Benefiting from the strong, size-tunable light absorption in the QDs and high carrier mobility in the MoS_2, the hybrid photodetector demonstrated a high responsivity of up to 10^6 A W^{-1}, which surpassed that of photodetectors based solely on MoS_2 or PbS by several orders of magnitude. Moreover, the detection range can be extended to the short-wave infrared (SWIR) region, which is far beyond the detection limit of pure MoS_2. Another advantage is its decreased *NEP* and consequently increased detectivity of up to 7×10^{14} Jones, achieved by suppressing its dark current by tuning the transistor in the OFF state (Figure 7d). The photodetection mechanism also relies on a strong photogating

effect. Light absorption in the PbS QDs generates electron–hole pairs, which are separated by the electric field at the PN interface between PbS and MoS_2. Holes are trapped within the QDs' layer and increase the carrier lifetimes. Meanwhile, electrons are transferred to the MoS_2 and circulate through the channel before recombination, leading to a high responsivity. More recently, Kang and co-workers demonstrated a hybrid phototransistor comprising a $CH_3NH_3PbI_3$ perovskite film on top of APTES-doped MoS_2.[237] Due to high absorption and long carrier diffusion lengths of the perovskite, a large number of photogenerated electrons and holes can be transferred to the MoS_2. This effect, combined with reduced photocarrier recombination and increased carrier mobility in MoS_2 induced by electron doping, gives rise to a significantly enhanced responsivity as high as 1.94×10^6 A W^{-1} and a detectivity of 1.29×10^{12} Jones.

In summary, hybrid phototransistors based on 2D layered semiconductors that make use of the photogating effect show large responsivities and gains that are normally several orders of magnitude higher than those of devices composed of 2D layered semiconductors alone (Table 3). Moreover, their operation can be extended to the NIR or even the SWIR region by sensitizing appropriate light absorbers. However, these devices usually show relatively long response times, making them more suitable for special applications where speed is not a necessity. Compared to hybrid devices with a graphene conducting channel, devices employing other 2D layered semiconductors with intrinsic bandgaps as conducting materials can generate a lower dark current and thus larger detectivities, which might be more suitable for practical applications.

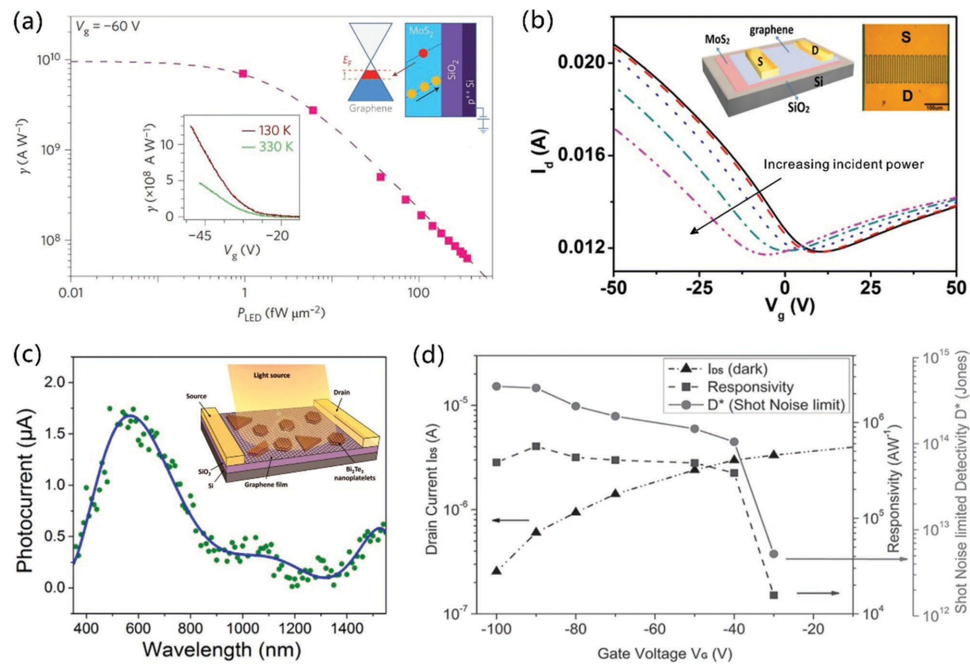

Figure 7. a) Responsivity of a graphene/MoS2 hybrid device as a function of illumination power. Dashed line is a fit of the form $A1/(A2+P_{LED})$, considering A1 and A2 as the fitting parameters. Top-right inset: schematic of charge exchange process for $V_g \ll V_T$. Bottom-left inset: comparison of low-temperature and room-

temperature responsivity. Reproduced with permission.[222] Copyright 2013, Nature Publishing Group. b) Transfer curves for a graphene/MoS_2 photodetector under the exposure of light with various powers. Inset shows the schematic illustration and an optical image of the photodetector based on graphene/MoS_2 stacked layers. Reproduced with permission.[223] Copyright 2014, Nature Publishing Group. c) Photocurrent of a graphene/Bi_2Te_3 heterostructure device as a function of photoexcitation wavelength (from 400 to 1550 nm). The green dots are experimental data, and the blue line is a visual guide. Inset shows schematic of the heterostructure phototransistor device. Reproduced with permission.[228] Copyright 2015, American Chemical Society. d) Drain current IDS (under dark conditions), responsivity R, and the shot-noise limited detectivity D* of a MoS_2/PbS QDs hybrid photodetector as a function of back-gate voltage VG measured at $V_{DS} = 1$ V. Reproduced with permission.[230] Copyright 2015, Wiley-VCH.

4. Photodiodes Based on 2D Layered Semiconductors

The photodiodes based on 2D layered semiconductors have been realized with different structures and principles. **Table 4** summarizes the figures of merit of some representative photodiodes based on 2D layered semiconductors and artificial heterostructures.

4.1. Local Electrostatically Defined PN Junctions

The ultimate thickness of 2D layered semiconductors allows tuning their carrier densities, band alignment, and polarities via electrostatic doping[25,48,49] or chemical doping.[50–52] There exists a variety of 2D layered semiconductors, such as WSe_2,[48] $MoSe_2$,[49] and few-layer BP,[25] that can readily exhibit ambipolar transport properties and enable PN junctions by local electrostatic gating. In this section, we introduce the studies related to photodiodes based on such PN junctions.

A typical schematic illustration of a local electrostatically defined PN junction is shown in **Figure 8**a. The fabrication ofsuch PN junctions usually begins with standard electron-beam lithography and metal deposition to define split gate electrodes on a cleaned SiO_2/Si substrate, followed by covering with a dielectric layer, which can be Si_3N_4,[238] HfO_2,[239] or layered h-BN.[240–243] Afterwards, single-layer WSe_2 or few-layer BP is mechanically exfoliated from their bulk crystals (multilayered $MoSe_2$ is synthesized by a CVT method[243]) and transferred onto the substrate, and source and drain contacts are defined by another electron-beam lithography and metal deposition process. In particular, metals with high and low work functions can be chosen to facilitate hole and electron injection, respectively.

Table 4. Performance of photodiodes based on 2D layered semiconductors and artificial heterostructures. FL: Few-layer, AuNPs: Au nanoparticles, ML: Multilayer, Gr: Graphene, C8-BTBT: Dioctylbenzothienobenzothiophene, SWNTs: Single-walled carbon nanotubes.

Device type	Active layer	Spectral range	Responsivity [mAW^{-1}]	EQE	Response times [ms]	Detectivity [Jones]	Ref.
	1L WSe_2	Visible	16	–	–	–	[238]
Electrostatically	1L WSe_2	Visible-NIR	210	0.2%	–	–	[239]
defined PN junctions	1L WSe_2	Visible	0.70	0.1%	10	–	[241]
	FL BP	Visible-NIR	28	0.1%	2	–	[242]
	FL WS_2 (with AuNPs)	Visible	10^{-1}	30%	–	–	[39]
Gr/2D semiconductor/Gr	ML MoS_2	Visible	–	27%	5×10^{-2}	–	[244]
heterostructures	FL WSe_2	Visible	–	7.3%	1.6×10^{-6}	–	[247]
	ML InSe (at forward bias)	Visible-NIR	10^5	–	1	10^{15}	[248]
	1L WSe_2/1L MoS_2	Visible	10	2.4%	–	–	[253]
	ML WSe_2/ML MoS_2	Visible	120	34%	–	–	[254]
	1L WSe_2/ML MoS_2	Visible		12%	<0.1	–	[255]
	ML WS_2/ML MoS_2	Visible	760	–	–	–	[257]
	FL WS_2/FL MoS_2	Visible	2.3×10^{-3}	–	$>10^3$	–	[258]
2D semiconductor/2D	ML WSe_2/ML WS_2	Visible	–	–	<20	–	[259]
semiconductor vertical	FL WSe_2/FL $MoSe_2$	Visible-NIR	–	10^{-2}%	–	–	[260]
heterostructures	FL α-$MoTe_2$/FL MoS_2	Visible-NIR	322	85%	25	–	[261]
	1L WSe_2/1L Gr/2L MoS_2	Visible-IR	10^7	–	5.36×10^{-2}	10^{15}	[263]
	FL BP/1L MoS_2 (at forward bias)	Visible	3.54×10^3	0.3%	–	–	[264]
	FL BP/FL MoS_2	Visible-NIR	170	–	–	–	[265]
	FL BP/FL MoS_2 (at forward bias)	Visible-NIR	2.23×10^4	–	1.5×10^{-2}	3.1×10^{11}	[266]
	FL GaTe/FL MoS_2	Visible	1.365×10^3	–	<10	–	[269]
	ML C8-BTBT/1L MoS_2	Visible	22	–	–	–	[270]
	1L MoS_2/n-Si	Visible	7.2	–	–	$>7 \times 10^9$	[286]
	1L MoS_2/p-Si	Visible	1.1	–	–	–	[286]
	Vertically standing MoS_2/p-Si	Visible-NIR	300	–	3×10^{-3}	10^{13}	[288]
	ML MoS_2/n-Si (at reverse bias)	Visible-NIR	1.19×10^4	–	3.05×10^{-2}	2.1×10^{10}	[289]
2D material/semiconductor	FL GaSe/n-Si	Visible	–	23.6%	6×10^{-2}	–	[291]
heterojunctions	FL $GaTe_xSe_{1-x}$/n-Si	Visible	–	60%	0.13	–	[292]
	ML Bi_2Se_3/n-Si (at reverse bias)	Visible-NIR	2.428×10^4	–	2.5×10^{-3}	4.39×10^{12}	[293]
	1L MoS_2/GaAs	Visible-NIR	419	–	1.7×10^{-2}	1.9×10^{14}	[296]
	ML MoS_2/ZnO thin film (at reverse bias)	UV-visible	–	52.7%	≈70	–	[297]
	FL MoS_2/rubrene single crystal	Visible	500	–	<5	–	[298]
Other artificial	1L Gr/ML h-BN/1L MoS_2	Visible	0.3	–	1×10^4	–	[301]
heterostructures	1L MoS_2/SWNTs (at reverse bias)	Visible-NIR	120	25%	1.5×10^{-2}	–	[302]

In 2014, three research groups reported local electrostatically-defined PN junctions based independently on single-layer WSe_2.[238–240] The local gates can effectively control the charge carrier types and concentrations in the WSe_2 channel. Thus gate biases with opposite polarity can induce different carrier types in the adjacent parts of the channel, which leads to a rectifying junction (PN or NP depending on gate bias polarities), as identified by the rectifying I_{ds}–V_{ds} curves in the dark, shown in Figure 8b. The curves all demonstrate high rectification factors with large shunt resistances and low reverse saturation cur- rent, indicating high-quality PN interfaces. It is important to note that the device can be operated as a resistor (PP or NN) by applying gate biases with the same polarity (Figure 8b). These PN junctions can be explored with diverse functionalities, such as photodiodes, photovoltaic devices, and light-emitting diodes. Here, we only focus on their application as photodiodes.

Under illumination, the I_{ds}–V_{ds} characteristics of a device introduced by Zaumseil et al.[238] are shifted down (or up) when biased in PN (or NP) diode configuration, giving rise to a short-circuit current I_{SC} and an open circuit voltage V_{OC} (Figure 8c). This is clear evidence for the photovoltaic effect expected in the PN junction. Figure 8d depicts a photocurrent map obtained with SPCM of another device in NP diode

configuration.[239] It is obvious that the photocurrent is symmetric and centered at the depletion region (separation between the gates), which strongly suggests that the photoresponse is dominated by the PN junction rather than the Schottky barriers at the contacts. The I_{ds}–V_{ds} curves under varied incident powers are shown in Figure 8e. The photocurrent at V_{ds} = -2.0 V increases linearly with incident power up to 8.0 μW (inset in Figure 8e), resulting in a responsivity of 210 mA W^{-1}. The maximum *EQE* is estimated to be 0.2% under 522 nm illumination.

The PN photodiode can also work at zero-biased V_{ds} condition with good performance, as demonstrated by Groenendijk et al.[241] The I_{SC} rises linearly while the V_{OC} increases logarithmically with increasing optical power when the device is biased in PN diode configuration, as shown in Figure 8f. This also confirms that the dominant photocurrent generation mechanism is the photovoltaic effect as well as ideal diode behavior. Figure 8g shows the comparison of the time-dependent photocurrent of this device at constant V_{ds} = 0 V or -1.0 V, from which a larger photocurrent of ≈0.43 nA at V_{ds} = -1.0 V is observed, corresponding to a maximum responsivity of 0.70 m A W^{-1}. At zero-biased V_{ds}, the response times are ≈12 ms, which decrease in reverse bias. The *EQE* estimated from I_{SC} reaches a maximum of ≈0.1%. It is interesting to note that when the device is biased in PP configuration, the photocurrent originates from the photo-thermoelectric effect, as identified by the 2D gate photocurrent maps obtained under above-bandgap and below bandgap illuminations. This can be explained by the presence of a temperature gradient, which induces a photo-thermoelectric voltage that can drive a current in the device due to strong light absorption in the local thicker part of the flake.

In addition to WSe_2, such PN junctions have also been realized with few-layer BP[242] or multilayered $MoSe_2$.[243] For example, Buscema et al. reported a few-layer-BP-based PN junction, employing a thin h-BN flake as an atomically-flat and disorder-free dielectric layer on two split gates.[242] Benefiting from the ambipolarity, local electrostatic gating can effectively control the charge carrier type and density in few-layer BP. As shown in the dark I_{ds}–V_{ds} curves (Figure 8h), the device readily demonstrates rectifying behavior when the two gates are biased with opposite polarity (PN or NP configuration), while the curves show almost linear behavior when the two gates are biased with the same polarity (PP or NN configuration). Under illumination, the photocurrent and photovoltage are only generated when the two gates are oppositely biased, indicating that the photoresponse generation mechanism relies on the photovoltaic effect originating from the PN or NP junction in the channel. With increasing incident power, the I_{ds}–V_{ds} curves shift down towards more negative current values in PN configuration, giving rise to increased I_{SC} and V_{OC}. Interestingly, the photoresponse can be extended to the NIR spectrum (Figure 8i) due to the narrow bandgap of few-layer BP. The device reaches a maximum responsivity of 28 mA W^{-1} and decreases to several mA W^{-1} as excitation wavelength increases. The maximum *EQE* is ≈0.1% at 640 nm illumination and the response times are ≈2 ms.

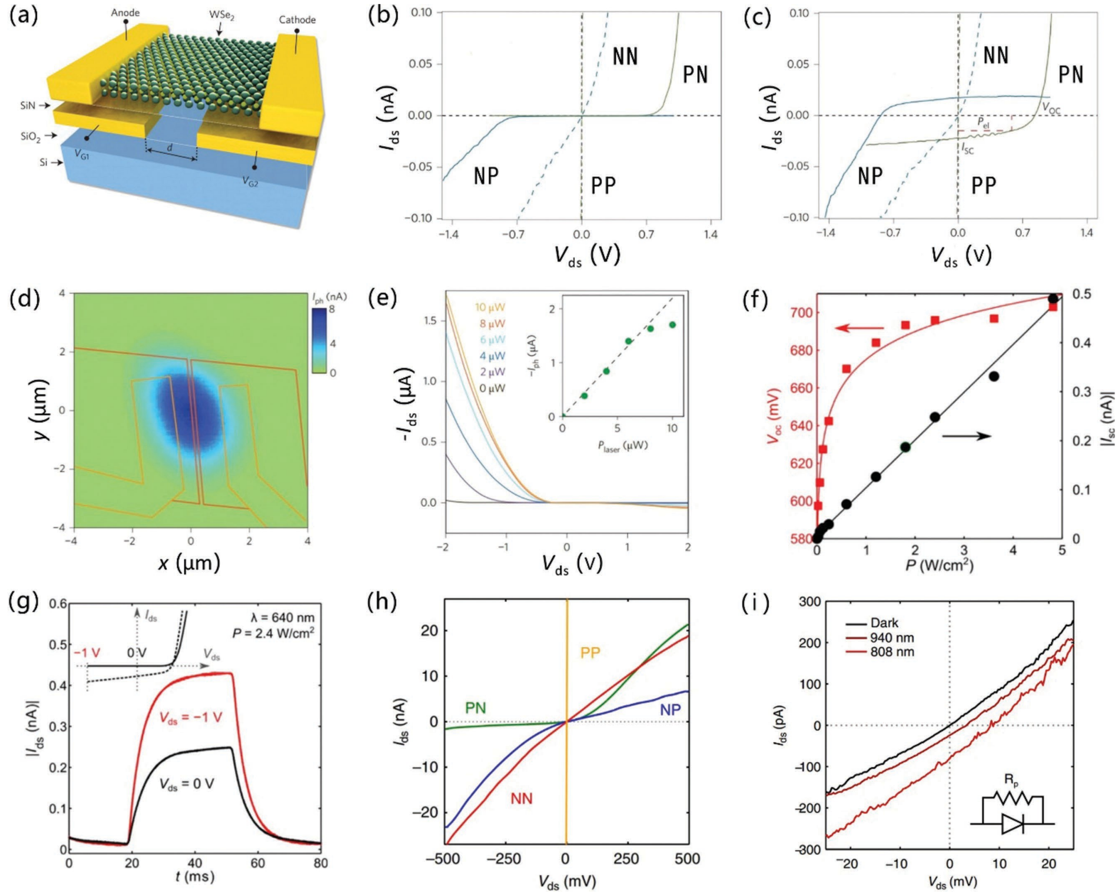

Figure 8. a) Schematic illustration of a local electrostatically defined PN junction based on single-layer WSe_2. I_{ds}–V_{ds} characteristics of the PN junction device measured in varied gate biasing configurations b) in darkness and c) under optical illumination, respectively. Reproduced with permission.[238] Copyright 2014, Nature Publishing Group. d) Photocurrent map of the PN junction device in NP configuration. e) I_{ds}–V_{ds} characteristics of the device in NP configuration under various laser powers. Inset shows I_{ph} at V_{ds} = -2 V as a function of laser power. (d,e) Reproduced with permission.[239] Copyright 2014, Nature Publishing Group. f) V_{oc} and J_{sc} of the PN junction device in PN configuration as a function of incident light power intensity. g) Time-dependent photocurrent of the device at V_{ds} = 0 V and –1 V in PN configuration, respectively. Inset shows I_{ds}–V_{ds} characteristics in darkness and under illumination. (f,g) Reproduced with permission.[241] Copyright 2014, American Chemical Society. h) I_{ds}–V_{ds} characteristics of the PN junction device measured in varied gate biasing configurations in dark. i) I_{ds}–V_{ds} characteristics of the device in PN configuration measured in darkness and under NIR illuminations. h,i) Reproduced with permission.[242] Copyright 2014, Nature Publishing Group.

In summary, thanks to their ambipolar property, some 2D layered semiconductors can form lateral PN junctions with local electrostatic gating. In the PN junctions, photocarrier generation, separation, and transport processes can be controlled by the external electric fields applied on the split gates. With their unique optical and electrical properties, PN junctions composed of single-layer WSe_2 or few-layer BP have been explored as photodiodes, showing responsivities between 0.70 mA W^{-1} to 270 mA W^{-1} and *EQE* values in the range of 0.1–0.2%. The response times

range between several to tens of milliseconds, which are comparable to the fastest phototransistors made from 2D TMDs or few-layer BP. The *NEPs* of these photodiodes are expected to be low due to the reduced dark current. Devices can be further optimized in their structure to increase light absorption or decrease contact resistance.

4.2. Graphene/2D Layered Semiconductor/Graphene Heterostructures

Rapid advancements in isolation and deterministic transfer of various 2D layered materials[244,245] allow the possibility of integrating them in vertical stacks for novel electronic and optoelectronic devices. In this section, we introduce the photodetection applications of graphene/2D layered semiconductor/graphene vertically stacked heterostructures. A schematic illustration of a typical heterostructure is shown in **Figure 9**a. In the device, carrier transport occurs in the 2D layered semiconductor in the out-of-plane direction, while the graphene layers serve as trans- parent charge extraction contacts. The finite density of states in graphene and weak electrostatic screening effect allow effective modulation of the Fermi level of graphene, and thus Schottky barrier height, between graphene and the semiconductor by electrostatic gating or chemical doping. Photocarrier generation, separation, and transport processes within the heterostructures can be modulated by the gate as well.

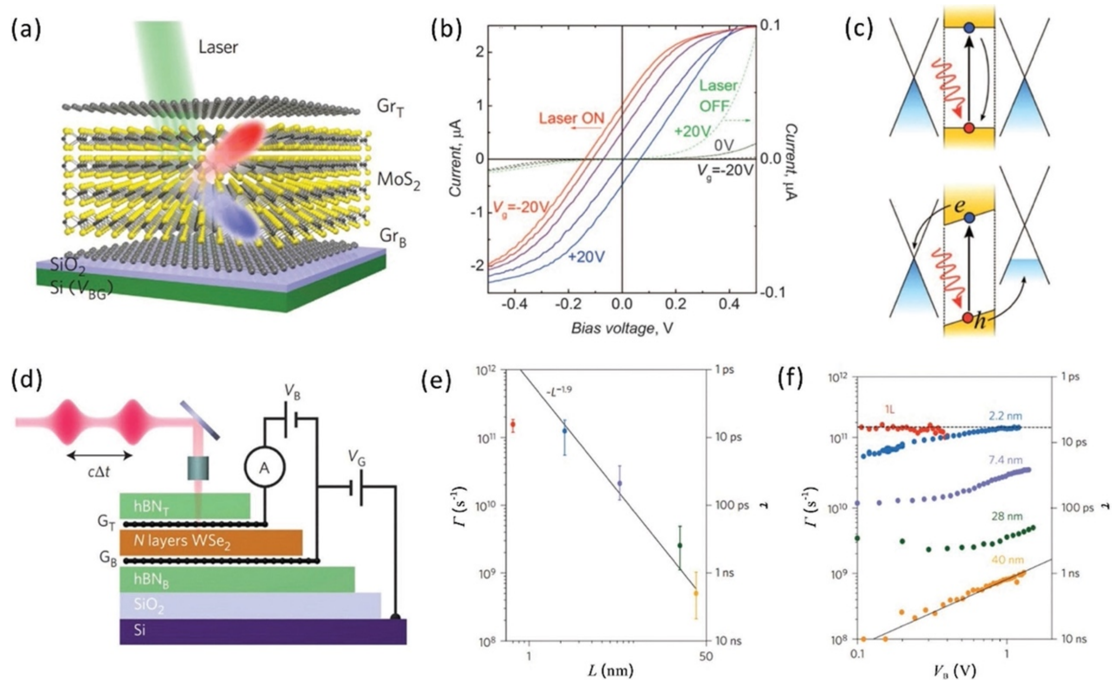

Figure 9. a) Schematic illustration of a graphene/MoS_2/graphene vertically stacked heterostructure. Reproduced with permission.[246] Copyright 2013, Nature Publishing Group. b) I_{ds}–V_{ds} characteristics of a graphene/WS_2/graphene vertical heterostructure as a function of gate bias. The right (left) y-axis gives the current magnitude for measurements: in darkness, green traces; under illumination, blue to red traces. c) Schematic band alignments in equilibrium (top panel) and under gate bias or chemical doping (bottom panel). (b,c) Reproduced with permission.[39] Copyright 2013, American Association for the Advancement of Science. d)

Schematic illustration of the experimental setup of the time-resolved photocurrent measurement. e) Photoresponse rate and time constant of the device as functions of layer thickness of the WSe2. f) Photoresponse rate and time constant of the device as functions of working bias. d-f) Reproduced with permission.[247] Copyright 2015, Nature Publishing Group.

In 2013, Britnell et al. reported a vertically stacked heterostructure composed of WS_2 with a thickness of 5-50 nm sandwiched between two graphene layers.[39] In the dark, the device acts as a tunnelling transistor where the current is modulated by the gate electric field, as shown in Figure 9b (the green traces). Under illumination, the device shows a pronounced photoresponse with strong gate-tunable photocurrent (Figure 9b, blue to red traces). The I–V characteristics show linear behavior at low bias and become non-linear (current saturation) at high bias due to the finite number of free carriers in the photoactive region. The photocurrent generation is based on the photovoltaic effect, which can be understood with the help of the band diagrams depicted in Figure 9c. Ideally, the band alignment between the graphene layers and WS_2 is symmetric; therefore, photogenerated electrons/holes in WS_2 have no preferred diffusion direction, giving rise to zero net photocurrent (Figure 9c, top panel). However, a built-in electric field across the WS_2 can be formed due to a difference in doping levels or electrostatic gating in graphene layers, which can rapidly separate photogenerated electrons and holes and results in net photocurrent (Figure 9c, bottom panel). The gate-tunable built-in electric field thus allows the heterostructure to function as a photodiode or a photovoltaic cell. The heterostructure reaches the highest *EQE* above 30% and decreases quickly with increasing incident power. This is likely due to the absorption saturation in WS_2 as well as the screening of the built-in electric field by excited electrons in the conduction band of WS_2. Further integration with plasmonic metal nanostructures can lead to a 10-fold improvement in the photocurrent (the responsivity increases from $\approx 10^{-2}$ A W^{-1} to $\approx 10^{-1}$ A W^{-1}).

Yu et al. demonstrated a similar heterostructure comprising 50 nm thick MoS_2 as the photoactive layer.[246] The heterostructure shows a strong photoresponse controllable by the gate voltage and fast response times on the order of ≈ 50 μs. Its *EQE* reaches a maximum value of $\approx 25\%$ and depends significantly on the incident light intensity and wavelength. Moreover, the polarity and amplitude of photocurrent can be modulated to an even higher extent by effectively changing the direction and strength of the built-in electric field in a dual-gated graphene/MoS_2/graphene heterostructure. A higher EQE of up to 55% has been achieved in an asymmetrical vertical structure of graphene/MoS_2/metal (Ti), where MoS_2-Ti forms nearly ohmic contact while graphene-MoS2 contacts form a Schottky junction, and the responsivity of the device reaches ≈ 0.22 A W^{-1}. In both studies, photocurrent maps via SPCM measurements reveal that the photocurrent is primarily generated in the regions of the heterostructures with asymmetric potentials.

Recently, Massicotte et al. have investigated the dynamics of the photoexcited charges in a vertically stacked graphene/WSe_2/graphene heterostructure via time-

resolved photocurrent measurements by exciting the device with a pair of ultrashort pulses (≈200 fs) separated by a variable time delay (Figure 9d).[247] They found that the fastest intrinsic response time can reach ≈5.5 ps in heterostructures based on mono-layer or tri-layer WSe_2. The response time increased to several nanoseconds for ≈40 nm thick WSe_2-based heterostructure (Figure 9e) and depends strongly on the working bias (Figure 9f). Limited by the instruments and their resistance- capacitance (RC) time, the heterostructure composed of WSe_2 with a thickness less than 10 nm shows a real-time photoresponse time less than ≈1.6 ns, which is significantly faster than other TMDs based photodetectors. More importantly, the *EQE* value of the device comprising tri-layer WSe_2 reaches 7.3%, corresponding to a high *IQE* value over 70%. In addition to TMDs, another 2D layered chalcogenide, InSe, has also been integrated with graphene in such a heterostructure.[248] Working at forward bias, the device shows a maximum responsivity of ≈10^5 A W^{-1} and a detectivity of ≈10^{15} Jones at low laser power; both decrease rapidly, however, with increasing laser power.

In summary, vertically stacked graphene/2D layered semiconductor/graphene heterostructures demonstrate tunable built-in electric fields across their heterostructures by electrostatic gating or chemical doping. This is a major advantage over conventional photodiodes. Consequently, photocarrier generation, separation, and transport processes can be readily manipulated. The photodetectors based on such heterostructures can reach responsivities between ≈10^{-2} A W^{-1} to ≈10^5 A W^{-1}, *EQE* values in the range of 7.3%–55%, and fast response times between ≈1.6 ns to ≈50 μs. Their performances are superior to those obtained from local electrostatically-defined PN junctions based on 2D layered semiconductors. This is likely due to the atomically thin carrier transient paths in their vertical heterostructures that facilitate efficient charge separation and collection.

4.3. 2D Layered Semiconductor/2D Layered Semiconductor Heterostructures

In the previous section, we discussed graphene/2D layered semiconductor/graphene vertically stacked heterostructures and their photodetection applications. In this section, we introduce the photodetection applications of 2D layered semiconductor/2D layered semiconductor heterostructures, including vertically stacked and laterally stitched ones. In general, vertically stacked heterostructures can be realized either by mechanical stacking, where the stacking order and the interface of the heterojunctions are critical to their electrical/optoelectronic properties, or by direct synthesis via CVD methods. On the other hand, laterally stitched heterostructures can only be grown by direct synthesis, since 2D layered materials are covalently bonded laterally. For more details about the preparation of 2D layered materials-based heterostructures, interested readers should refer to related perspectives and review papers.[44,45]

4.3.1 Vertically Stacked Heterostructures

A vertically stacked heterostructure based on single-layer 2D semiconductors with different conductive types can form a heterojunction usually with type II band alignment, which facilitates efficient electron–hole separation for light

detection or harvesting.[249,250] Compared to conventional heterostructures, these heterostructures should in principle possess many distinct advantages such as atomically sharp interfaces, no interdiffusion of atoms, digitally controlled layered components, and no lattice parameter constraints. Strong interlayer coupling of charge carriers[249] and ultrafast photoexcited charge transfer within 50 fs to sub-picosecond at the interface of single layers[250–252] have been observed in such heterostructures, enabling the design of novel devices for optoelectronics and light harvesting.

Recently, TMD/TMD vertical heterostructures, including WSe_2/MoS_2,[253–256] WS_2/MoS_2,[257,258] WSe_2/WS_2,[259] $WSe_2/MoSe_2$,[260] and α-$MoTe_2/MoS_2$[261] have been widely studied in the field of photodetection. For example, Lee et al. reported a vertical heterostructure composed of WSe_2 and MoS_2 single layers crossed on top of each other, as shown in **Figure 10**a.[253] Palladium and aluminum contacts were chosen for p-WSe_2 and n-MoS_2 to facilitate holes and electrons injection, respectively. In darkness, the heterostructure shows rectifying behavior, which can be tuned by gate voltages. Under illumination, the device shows a strong gatetunable photovoltaic response, as evidenced by the I_{ds}–V_{ds} characteristics in Figure 10b. A maximum photoresponse is observed at $V_g = 0$ V, the position where the heterostructure exhibits the strongest rectifying behavior. A spatial photocurrent map at $V_{ds} = 0$ V indicates that the photocurrent is generated primarily in the WSe_2/MoS_2 junction area (inset in Figure 10b). This result, combined with PL measurements, reveals that the photovoltaic response originates from the rapid separation of photocarriers between the two TMD layers. In particular, the strong gate-dependent photoresponse can be related to the interlayer tunnelling-mediated recombination of the majority carriers across the interface of the heterostructure, which can be tuned by gate voltages. A maximum responsivity of ≈2 mA W^{-1} can be further increased to ≈10 mA W^{-1} by using graphene electrodes, which allows carrier collection by direct vertical charge transfer and thus reduces interlayer recombination losses of photocarriers. The responsivity can be improved even further to ≈120 mA W^{-1} in the heterostructure consisting of two multilayer TMDs due to increased light absorption. The *EQE* also increases with increasing layer thickness and reaches the highest value of ≈34% in the multilayer heterostructure.

Very recently, Pezeshki and co-workers fabricated a vertical heterostructure consisting of few-layer α-$MoTe_2$ and MoS_2 and probed its electronic and optoelectronic properties.[261] Their results show that the heterostructure exhibits a strong photovoltaic response from the visible to NIR (800 nm) range. The responsivity and *EQE* reach the maximum values of 322 mA W^{-1} and 85% under visible light and decrease rapidly to 38 mA W^{-1} and 6% at 800 nm NIR light, respectively. The response times are on the order of ≈25 ms, and the obvious NIR response is likely attributed to the small bandgap of few-layer α-$MoTe_2$.[262]

In particular, broadband photodetection with a response range up to 2400 nm can be realized by sandwiching graphene with a gapless band structure that enables broadband light absorption in a WSe_2/MoS_2 vertical heterostructure (inset in Figure

10c).[263] Similarly, this heterostructure shows an apparently gate-tunable rectifying behavior and a photovoltaic response. The responsivity and detectivity are as high as 10^4 A W^{-1} and 10^{15} Jones at visible wavelength and decrease drastically to 10^{-1} A W^{-1} and 10^9 Jones at IR wavelength (2400 nm) at forward bias, respectively (Figure 10c). The response times are tens of microseconds, and the broadband wavelength-dependent photoresponse can be attributed to the energy band diagrams of the heterostructure. In the visible range where photon energy is larger than the bandgaps of the TMDs, all three layered materials (WSe_2, graphene, and MoS_2) can absorb light efficiently and produce abundant electron–hole pairs, resulting in a considerably larger photocurrent (Figure 10d, left panel). However, under IR light where photon energy is smaller than the bandgap of WSe_2, light can only be absorbed by graphene and generates electron–hole pairs (Figure 10d, right panel), which leads to a much smaller photocurrent in the IR range.

Moreover, vertical heterostructures consisting of few- layer BP and single- or few-layer MoS_2 have recently been explored.[264,265] As expected, these heterostructures show obvious current-rectifying behaviors and photovoltaic responses that are tunable by gate. The device reaches a maximum responsivity of 3.54 A W^{-1} at forward bias, which decreases to 418 mA W^{-1} at reverse bias.[264] Very recently, a broadband photodetector with a visible to NIR detection range has also been achieved in such a heterostructure.[266] The strong response in the NIR is attributed to the photocarrier excitation in the few-layer BP due to its narrow bandgap. The responsivity of the heterostructure is 22.3 A W^{-1} under 532 nm illumination and decreases to 153.4 mA W^{-1} under 1550 nm illumination.

In addition to the vertical heterostructures described, those comprising TMDs and/or other 2D materials, such as $InAs/WSe_2$,[267] SnS/SnS_2,[268] $GaTe/MoS_2$,[269] C8-BTBT/MoS_2,[270] and $CH_3NH_3PbI_3/WSe$ [271] have also demonstrated diodelike rectifying behaviors and pronounced gate-tunable photovoltaic responses. In particular, Cheng et al. reported vertically stacked heterostructures composed of organohalide perovskites ($CH_3NH_3PbI_3$) and 2D layered materials.[271] Two device architectures have been realized, including a graphene/$CH_3NH_3PbI_3$/graphene vertical stack and a graphene/WSe_2/ $CH_3NH_3PbI_3$/graphene vertical heterojunction. 2D $CH_3NH_3PbI_3$ is obtained by converting ultrathin PbI_2 layers exfoliated from a PbI_2 crystal via a vapor phase intercalation method. The first device reaches a maximum responsivity of ≈950 A W^{-1} and a photoconductive gain of ≈2200- much higher than those of perovskite photoconductors with lateral configuration.[272,273] Response times are on the order of several millimeters, and the high performance can be attributed to the extremely short vertical carrier transit path and thus a small carrier transit time. The second device shows diode-like rectifying behaviors within a positive VG range, whereas nearly symmetric *I–V* characteristics can be observed within the negative VG range (Figure 10e). This is attributed to the transition from the PN to PP junction at the perovskite/WSe_2 interface due to the ambipolar nature of WSe_2 under different gate biases. Under illumination, the heterostructure demonstrates a strong gate-modulated photovoltaic response, as evidenced by the *I–V* characteristics in Figure 10f.

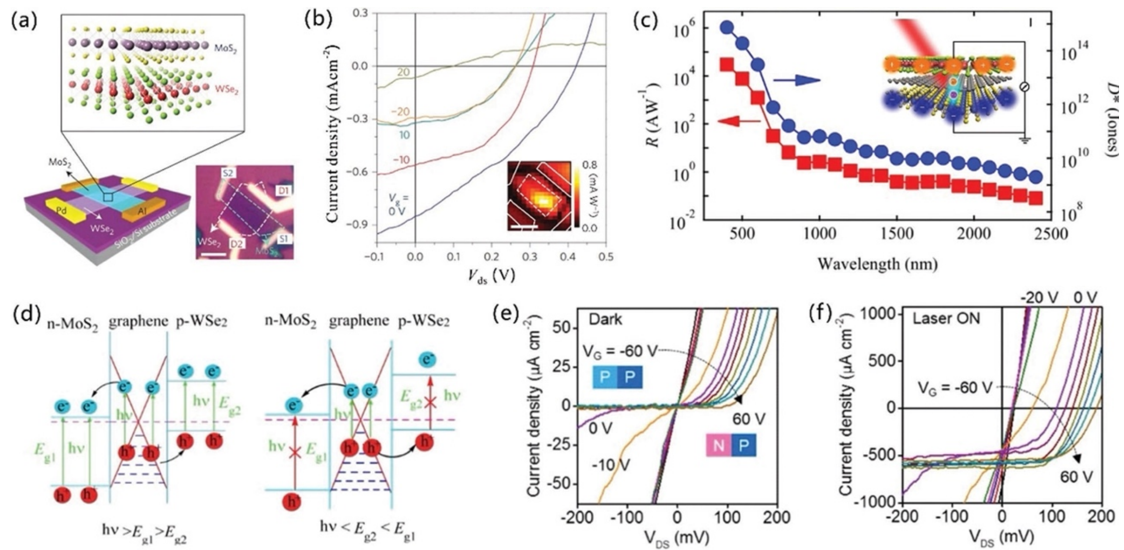

Figure 10. a) Bottom left: Schematic diagram of a van der Waals-stacked MoS_2/WSe_2 heterojunction device. Top: enlarged crystal structures of MoS_2 and WSe_2 single layers. Bottom right: Optical image of the fabricated device. b) Photoresponse characteristics of the heterostructure at various gate voltages under white-light illumination. Inset shows the photocurrent map of the heterostructure at V_{ds} = 0 V. (a,b) Reproduced with permission.[253] Copyright 2014, Nature Publishing Group. c) Responsivity R (left) and specific detectivity D^* (right) of a WSe_2/graphene/MoS_2 for wavelengths ranging from 400 to 2400 nm. Inset shows a schematic illustration of the heterostructure. d) Schematic band diagrams of the heterostructure in UV/visible range (left panel) and IR range (right panel). (c,d) Reproduced with permission.[263] Copyright 2016, American Chemical Society. I_{ds}–V_{ds} characteristics of the graphene/WSe_2/$CH_3NH_3PbI_3$/graphene vertical heterostructure e) in darkness and f) under illumination at varied V_G. Reproduced with permission.[271] Copyright 2016, American Chemical Society.

4.3.2. Laterally Stitched Heterostructures

Recently, TMD/TMD lateral heterostructures such as MoS_2/ $MoSe_2$,[274] WS_2/WSe_2,[274] $MoSe_2/WSe_2$,[275] WS_2/MoS_2,[276] WSe_2/MoS_2,[277] and WSe_2/MoS_2[278] have been successfully realized by one-pot or two-step CVD methods. These heterostructures exhibit diode-like behaviors such as gate-modulated current rectifying properties (**Figure 11**a) and photovoltaic responses (Figure 11b). For example, a WS_2/WSe_2 lateral heterostructure provides a pronounced photoresponse with response times less than 100 µs (inset in Figure 11b).[274] Photocurrent mapping reveals that the photocurrent is generated at the lightly-doped WS_2 and WS_2/WSe_2 interface regions (inset in Figure 11a), indicating that the photoresponse originates from photocarrier generation and separation at the heterojunction. In addition, Feng et al. reported a lateral heterostructure composed of $InSe/CuInSe_2$, where $CuInSe_2$ was prepared by partially transforming InSe through a simple solid-state reaction method.[279] Apparently, the heterostructure shows robust rectifying behavior with a small ideality factor. Due to its narrow bandgaps, the lateral diode can provide a broadband photoresponse (254-850 nm) with the maximum responsivity of 8.4

A W^{-1} under UV light. The responsivity depends strongly on the incident light wavelength and decreases with increased incident power.

In summary, 2D/2D layered semiconductor vertical and lateral heterostructures can be easily prepared by mechanical stacking or direct synthesis methods. The rich family of 2D layered semiconductors with different electrical and optical properties makes it possible to realize multifunctional devices. Photodetectors based on these heterostructures show broadband responsivities in a wide range from several mA W^{-1} to 10^4 A W^{-1} and response times between tens of microseconds to tens of milliseconds. Further work, especially on lateral heterostructures, is needed to both explore fundamental study and develop practical applications.

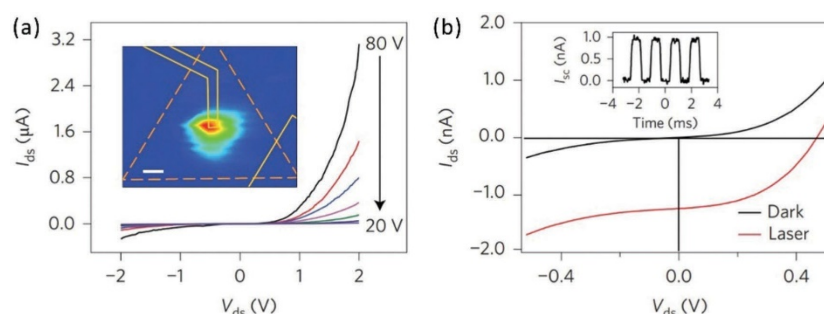

Figure 11. a) Gate-tunable I_{ds}–V_{ds} characteristics of a lateral WSe_2-WS_2 heterojunction PN diode. Inset shows the photocurrent map of the lateral heterojunction. b) I_{ds}–V_{ds} characteristics of the lateral heterojunction in darkness and under illumination. Inset shows the time- dependent photoresponse of the device. (a,b) Reproduced with permission.[274] Copyright 2014, Nature Publishing Group.

4.4. 2D Layered Semiconductor/2D Layered Semiconductor Homojunctions

4.4.1. Vertical Homojunctions

A homojunction with continuous band alignment possesses small carrier trap sites at the interface and can provide low contact resistance at the interface and high carrier transport efficiency through the interface, which is beneficial for optoelectronic applications. Vertically stacked PN homojunctions composed of 2D layered TMDs such as MoS_2 and $MoSe_2$ were introduced recently.[280,281] For example, Li et al. reported the realization of a vertical PN junction comprising ultrathin MoS_2 layers, where p-MoS_2 and n-MoS_2 were achieved via chemical doping with $AuCl_3$ and benzyl viologen as dopants, respectively.[280] **Figure 12**a shows schematic illustration of a typical vertical homojunction. When functioning as an FET, the device shows ambipolar carrier transport with an obvious current hysteresis (Figure 12b), contributed by electrons and holes with lateral in-plane transport along the MoS_2 layers, as well as vertical interlayer tunneling. The device can also be used as a phototransistor with a pronounced photoresponse under illumination (Figure 12b). Interestingly, the MoS_2 homojunction provides a clear gate-tunable current rectifying behavior via modulation of the potential barrier or a reversed current rectification via direct tunneling. Under illumination, such a homojunction exhibits a strong photoresponse and can function as a phototransistor at forward biases and a photodiode at zero bias. The responsivity

of the photodiode is 30 mA W^{-1}. In another work, Jin and co-workers realized a vertical homojunction consisting of few-layer p-type $MoSe_2$ by Nb-doping and few-layer intrinsic $MoSe_2$ with inherent n-type behavior.[281] The homojunction shows a typical gate-modulated rectifying characteristic with a large current ON/OFF ratio and a small ideality factor, implying ideal diode behavior. The homojunction exhibits a pronounced photovoltaic response, as shown in Figure 12c. The responsivity reaches a maximum of several amps per watt at forward bias and tens to hundreds of milliamps per watt at zero and reverse biases (Figure 12d).

4.4.2 Lateral Homojunction

A lateral homojunction has been realized in few-layer MoS_2 containing p-MoS_2 chemically doped with $AuCl_3$ and intrinsic n-type MoS_2. Partially stacked 2D h-BN was used as a protecting mask to isolate the underlying intrinsic MoS_2 from the dopant (Figure 12e).[282] Asymmetric contacts of Pd and Cr/Au were incorporated, respectively, in p-MoS_2 and n-MoS_2 to facilitate the injection of holes and electrons. The device exhibits a pronounced gate-modulated current rectifying behavior in the dark and a photovoltaic response under illumination as well. As depicted in Figure 12f, the transfer characteristics under illumination show two distinct photoresponse regions, which are attributed to the gate-induced accumulation of electrons (at positive V_G) or holes (at negative V_G) that reduces the barrier height between the conduction or valence band edge of MoS_2 and the contacts. At zero V_G, the device gave a responsivity and detectivity of 5.07 A W^{-1} and 3×10^{10} Jones at forward bias, respectively, and 0.33 A W^{-1} and 1.6×10^{10} Jones at reverse bias, respectively. The response times are in the order of 100–200 ms. More recently, Yu et al. reported a few-layer-BP-based lateral homo- junction with a similar device geometry, where benzyl viologen (BV) was introduced as an effective electron dopant in BP.[283] Due to the narrow bandgap of the few-layer BP, the device is capable of detecting NIR light (1.47 μm) with a responsivity of ≈180 mA W^{-1} and fast response times on the order of tens of milliseconds.

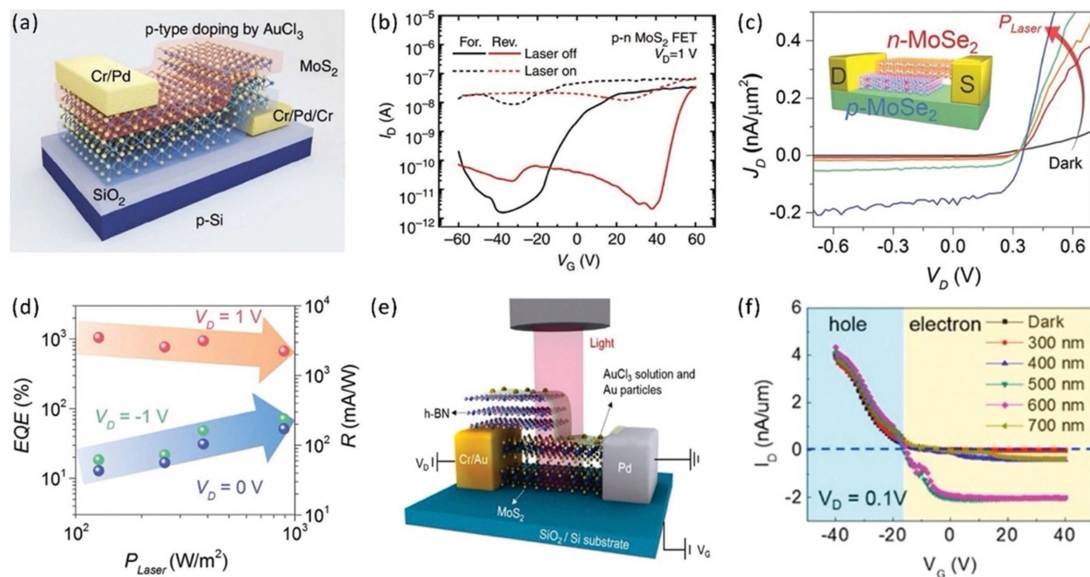

Figure 12. a) Schematic illustration of a MoS_2 vertical homojunction. b) The transfer characteristics of the homojunction measured in darkness and under illumination during both the forward and reverse sweeps. Reproduced with permission.[280] Copyright 2015, Nature Publishing Group. c) Current density–voltage (J_D–V_D) curves of the $MoSe_2$ homojunction PN diode in darkness and under light irradiation with various laser power densities for V_G = 0 V. Inset shows schematic illustration of the homojunction. d) Responsivity and *EQE* for various V_D as a function of light irradiation power. (c,d) Reproduced with permission.[281] Copyright 2015, Wiley-VCH. e) Schematic illustration of a MoS2 lateral homojunction. f) I_D–V_G curves of the lateral homojunction under light exposure with different wavelengths. e,f) Reproduced with permission.[282] Copyright 2014, American Chemical Society.

4.5. 2D Layered Material/Semiconductor Heterojunctions

Benefiting from deterministic transfer techniques[244,245] and advanced growth methods,[4,22,24,26] 2D layered materials can be readily integrated with conventional semiconductors to form van der Waals heterojunctions. This includes 3D bulk materials such as Si,[284–293] GaN,[294] GaAs,[295,296] or 2D thin films such as ZnO film,[297] CuPc film,[298] and rubrene single-crystal.[299] These heterojunctions with atomically sharp interfaces can be exploited as optoelectronic devices with versatile functionalities, including photodiodes, photovoltaic devices, and light-emitting diodes.

Heterojunctions composed of 2D MoS_2 and Si have been extensively studied as photodetectors.[286–290] Schematic illustration of a typical device geometry is shown in the inset of **Figure 13a**. A single-layer MoS_2 flake is transferred on top of a p-doped Si substrate, and a PN heterojunction forms at the Si/ MoS_2 interface. In darkness, the current–voltage (*I*–*V*) characteristic shows typical diode-like behavior with a good rectifying factor (Figure 13a). Li et al. have studied the photoresponse of both monolayer MoS_2/n-Si and monolayer MoS_2/p-Si heterojunctions.[286] Both heterojunctions show obvious photoresponses at reverse bias under illumination, which depend upon the incident light wavelength and power intensity. The highest responsivity reaches 7.2 A W^{-1} for the MoS_2/n-Si heterojunction, while the value decreases to ≈1 A W^{-1} for the MoS_2/p-Si heterojunction. The underlying mechanisms of the different photoresponse behaviors were further investigated by combining Kelvin probe microscope (KFM) studies and band alignment analyses. The results show that the photodiode behavior originates from the intrinsic built-in electric field at the MoS_2/p-Si interface, whereas the built-in electric field from a modulated barrier height and width induced by photogenerated excitons in the vicinity of the MoS_2/n-Si interface is responsible. Heterojunctions can also be constructed by directly depositing MoS_2 films on Si substrates via magnetron sputtering techniques[288] or a dip-coating method followed by an annealing process.[289] For example, Wang et al. demonstrated that molecular layers of MoS_2 can be deposited perpendicularly on an Si substrate to form a PN heterojunction via a scalable magnetron sputtering method, where the vertically standing layered structures offer high-speed paths for the separation and transportation of photocarriers.[288] The strong light absorption

of the relatively thick MoS_2 film in combination with the unique structure gives rise to an outstanding photoresponse in a broadband wavelength range and robust air stability. Working in photovoltaic mode (under zero-biased voltage), the device shows a responsivity of ≈300 mA W^{-1}, a detectivity as high as ≈10^{13} Jones due to a depressed dark current, and response times of ≈3 μs.

The band alignment between MoS_2 and Si unveils the working mechanism of the heterojunction photodetectors. Li et al. studied the 3D band diagrams of an n-type monolayer MoS_2/p-type bulk Si heterojunction, a prototype of the 2D–3D heterostructures.[290] The wavelength-dependent photocurrent measurements strongly suggest type I band alignment between the heterojunction (Figure 13b), where photocarriers can move along both the vertical (*z*) direction (e.g., flowing from bulk Si into the MoS_2) and in the lateral (*x*–*y*) direction (e.g., driven by an in-plane electrical field). Moreover, the performance of the heterojunction is mainly determined by the electron–hole pair excitation and collection in the MoS_2 monolayer in the heterojunction.

In addition to MoS_2, other 2D layered materials such as GaSe,[291] $GaTe_xSe_{1-x}$,[292] and Bi_2Se [293]³ have been integrated with Si to function as photodiodes. Xiu's group reported the realization of 2D GaSe/Si[291] and 2D $GaTe_xSe_{1-x}$/Si[292] PN heterojunctions via a layer-by-layer van der Waals epitaxial growth technique. These heterojunctions demonstrate steady rectifying characteristics in the dark and prominent photoresponse behaviors, which strongly depend on the incident laser power, as expected in photodiodes (Figure 13c). In particular, the 2D GaSe/Si heterojunction shows a maximum *EQE* of ≈23.6%, which rapidly decreases to ≈2% with decreasing GaSe layer number, presumably due to weakened light absorption in thinner layers and the band structure transition.[291] The response times are tens of microseconds. The fast response can be accounted for by the strong built-in electric field induced by the highly depleted region in the GaSe, which can efficiently separate photocarriers, as well as the short carrier transport distance arising from the vertical heterostructure. The *EQE*s for the 2D $GaTe_xSe_{1-x}$/Si heterojunction reach a maximum value around 60% and decrease with increasing Se composition, as shown in Figure 13d.[292]

More recently, Zhang et al. reported a 2D topological insulator Bi_2Se_3/Si heterojunction by van der Waals epitaxial growth of Bi_2Se_3 films tens of nanometers thick on a n-Si substrate via a PVD method.[293] The heterojunction routinely demonstrates obvious diode-like characteristics and a strong light-intensity-dependent photoresponse. The responsivity reaches 24.28 A W^{-1} at reverse bias, which decreases to 2.60 A W^{-1} at zero bias. Moreover, this device also shows fast response times on the order of several microseconds due to a built-in electric field at the junction. Interestingly, the heterojunction shows an extended photoresponse up to telecommunication wavelengths (1310 nm and 1550 nm), which is related to the small bulk bandgap and gapless character of topological surface states in Bi_2Se_3.

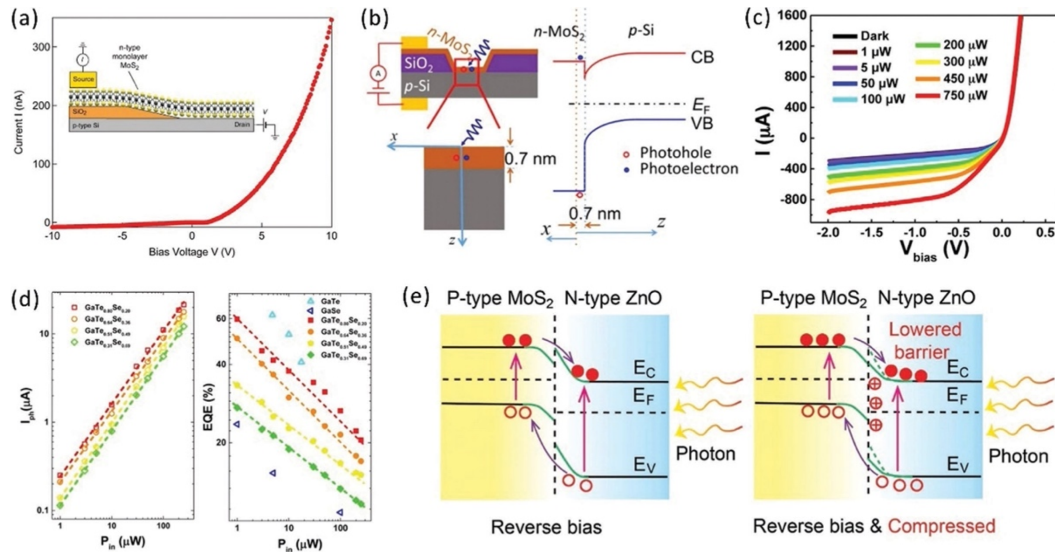

Figure 13. a) Current–voltage (*I–V*) characteristic of a p-Si/n-MoS_2 heterojunction. Inset shows schematic illustration of the heterojunction. Reproduced with permission.[285] Copyright 2014, American Chemical Society. b) A cross-sectional schematic (x-z plane) of the p-Si/n-MoS_2 heterojunction (left panel), together with a band diagram of the 2D-3D heterojunction along the x- and z-axes at zero bias under laser excitation. CB: conduction band, and VB: valence band. Reproduced with permission.[290] Copyright 2015, American Chemical Society. c) *I–V* characteristics of a 2D GaSe/Si heterojunction measured in darkness and under illumination with various powers. Reproduced with permission.[291] Copyright 2015, American Chemical Society. d) Composition-dependent photocurrent (left panel) and *EQE* (right panel) of a 2D $GaTe_xSe_{1-x}$/Si heterojunction under different laser intensities. Reproduced with permission.[292] Copyright 2015, American Chemical Society. e) Band diagrams of a 2D MoS2/ZnO heterojunction at reverse bias without and with an applied pressure, which illustrate the photogenerated carriers and the piezophototronic effect enhanced photocurrent. Reproduced with permission.[297] Copyright 2015, Wiley-VCH.

Apart from Si, monolayer MoS_2 has been combined with GaAs to form heterojunctions as photovoltaic-type detectors. In their recent study, Xu et al. demonstrated that a MoS_2/GaAs heterojunction shows a strong photoresponse in the range of UV to visible light with a responsivity of 321 mA W^{-1}, a detectivity of 3.5 $\times 10^{13}$ Jones, and response times of tens of microseconds.[296] It is notable that the responsivity can be increased by ≈30% to 419 mA W^{-1} via interface design by inserting a h-BN layer as well as photoinduced doping of MoS_2 by Si quantum dots. Moreover, the heterojunction displays an increased detectivity as high as 1.9×10^{14} Jones due to the depressed dark current of the MoS_2/h-BN/GaAs sandwich structure, where the presence of h-BN raises the barrier height, leading to increased shunt resistance and hence reduced thermal noise. More recently, Xue and co-workers reported the realization of a 2D MoS_2/ZnO film PN heterojunction, where p-type MoS_2 is achievable via a plasma-assisted doping method.[297] The heterojunction shows an obviously gate-tunable rectifying behavior. Under UV illumination, the device reaches the highest *EQE* of 52.7%, which can be enhanced by more than four times *via* the piezophototronic effect. The detailed mechanism for the enhanced photoresponse can be explained by the enlarged depletion region

within the ZnO film, which contributes to the generation and separation of photocarriers. With external pressure applied to the ZnO film, the positive piezoelectric charges yielded at the bottom surface of the ZnO lower the barrier at the heterojunction interface and reduce the up-bending of the energy bands of the ZnO, thus enlarging the depletion region within the ZnO film (Figure 13e). Inorganic-organic heterojunctions combine the novel properties of inorganic solids with those of organic materials, resulting in devices with diverse functionalities. Recently, Liu et al. reported an inorganic–organic heterojunction composed of 2D MoS_2 and a rubrene single crystal that shows a gate-tunable rectifying characteristic.[299] The heterojunction demonstrates a strong photoresponse with a responsivity of 510 mA W^{-1} at forward bias and response times of several milliseconds.

In summary, integration of 2D layered materials with conventional semiconductors can lead to novel van der Waals heterojunctions with atomically abrupt interfaces, harnessing the advantages of both materials. In general, photodetectors based on these heterojunctions show responsivities less than 1 A W^{-1} at zero bias, which can be increased to tens of amps per watt at reverse bias. The response times for heterojunctions based on 2D layered materials and bulk Si are typically several to tens of microseconds-much faster than PN junction photodetectors based on 2D layered materials via local electrostatic gating. Moreover, the fabrication processes are compatible with the mature Si technology, which might make such heterojunctions more amenable to practical applications.

4.6 Other Artificial Heterostructures

Integration of a 2D layered semiconductor with two metal (semi-metal) contacts possessing different work functions gives rise to differences in local doping of the layer, and therefore an asymmetry in the Schottky barriers at the two contacts. Such asymmetric Schottky barriers result in the formation of a built-in electric field, which is highly desirable in a photodiode. Fontana et al. reported a multi-layer MoS_2 flake-based Schottky barrier photodiode, where Au and Pd asymmetric contacts were chosen to achieve electron- and hole-doping, respectively (**Figure 14**a).[300] The diode demonstrates an obvious current rectifying behavior which is expected in darkness (Figure 14b). Under illumination, a strong photovoltaic response is observed, which is believed to originate from the photocarrier generation and separation by the built-in electric field, as shown in Figure 14b. The electronic and optoelectronic characteristics of such a heterostructure can be improved by inserting an insulating layer between the semiconductor and metal contact to form a metal-insulator-semiconductor (MIS) diode. In a recent study, Jeong and co-workers presented an MIS diode consisting of graphene, h-BN, and single-layer MoS_2. It demonstrated improved cur- rent rectification and much higher current flow over a metal-semiconductor (MS) diode and a PN junction made of 2D TMDs, due to carrier tunnelling at forward bias and depressed carrier tunnelling at reverse bias.[301] Moreover, the MIS diode exhibits a pronounced photoresponse with a responsivity of 0.3 mA W^{-1} and response times of $\approx$10 s.

Heterostructures composed of 2D layered semiconductors with other

nanomaterials have also shown great promise in the field of photodetection. By integrating p-type single- walled carbon nanotubes (SWCNTs) with n-type single-layer MoS_2, Jariwala et al. reported a vertically stacked PN junction diode with electrical characteristics that can be modulated by the gate bias to achieve a wide tunability of charge transport ranging from nearly insulating to highly rectifying.[302] Under illumination, a strong photovoltaic response in a wide range of irradiation wavelengths (500-1100 nm) is observed for the diode, indicating that exciton and/or free carrier generation in both materials contribute to the photocurrent. Photocurrent mapping via SPCM reveals that photocurrent generation lies in the overlapped area of the two components, confirming that the photocurrent is generated by the vertical heterojunction. Interestingly, as shown in Figure 14c, the relative photocurrent contribution from the SWCNTs decreases with decreased V_G, which is explained by the shortened depletion region in SWCNTs due to higher doping/majority carrier concentration induced by negative V_G on this side. The responsivity depends strongly on the gate bias and reaches a maximum value of 0.1 A W^{-1} under 650 nm illumination, decreasing rapidly under illuminations of longer or shorter wavelength. The diode shows fast response times with an upper limit of 15 μs, also due to the extremely short distance the photocarriers must traverse. Very recently, Lee and colleagues have demonstrated a nanocrystalline graphene-MoS_2 lateral interface heterostructure (Figure 14d), which shows a distinct diode-like current rectifying behavior.[303] The rectifying characteristic stems from built-in electric fields formed at the lateral interfaces and a potential shift in graphene induced by the metallic edge effect of the MoS_2. Under illumination, the heterostructure shows a photoresponse with a photocurrent ≈500 times stronger than a vertically stacked graphene/MoS_2 heterostructure. Moreover, the lateral interface device shows response times of ≈2.8 s, also making it faster than the vertical one (≈4.5 s). The improved photoresponse is attributed to the built-in electric field, which can efficiently separate the photocarriers.

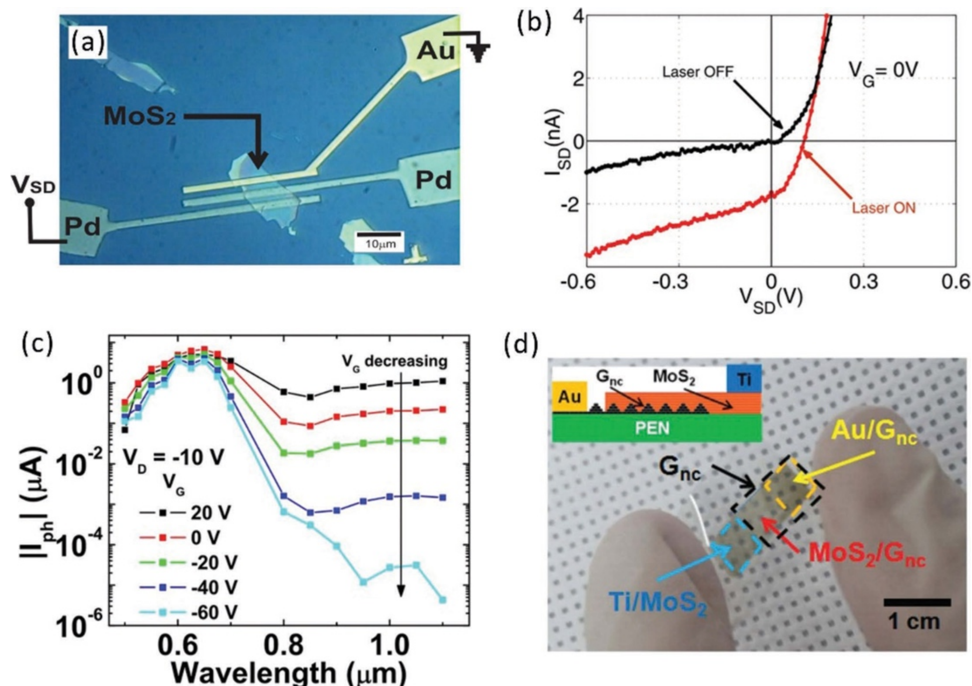

Figure 14. a) Optical image of an MoS_2 Schottky barrier diode with asymmetric electrodes. b) *I–V* characteristics of the Schottky diode in darkness and under illumination. Reproduced with permission.[300] Copyright 2013, Nature Publishing Group. c) Photocurrent spectral response of an SWCNTs/MoS_2 PN heterojunction at varied V_G. Reproduced with permission.[302] Copyright 2013, National Academy of Sciences, USA. d) Photo image of a nanocrystalline graphene/MoS_2 heterostructure on a transparent flexible substrate. Inset shows schematic illustration of the heterostructure. Reproduced with permission.[303] Copyright 2016, Wiley-VCH.

5. Light-Matter Interaction for Sensitive Enhancement

Although 2D layered semiconductors demonstrate strong light-matter interaction, the absolute light absorption is very low for such atomically thin layers. Further absorption enhancement is highly desirable in 2D-layered-semiconductors-based optoelectronic devices for some applications. Recently, several methods, including plasmonic techniques, integration of optical waveguides, and microcavities have been developed with the aim to increase light-matter interaction for light absorption enhancement. In this section, we discuss techniques that are relevant to 2D-layered-semiconductor-based photodetectors.

5.1. Plasmonic Nanostructures

Plasmonic metallic nanostructures can offer at least two ways to enhance light absorption in 2D layered semiconductors. First, localized surface plasmons (LSPs) in metallic nanostructures can lead to oscillation of conduction electrons in the nanostructures, which greatly enhances local electromagnetic fields that improve light absorption in semiconductors.[304,305] Moreover, the metallic nanostructures act as subwavelength scattering elements that can couple and trap freely propagating plane waves from the incident light into semiconductors.[305,306] In addition, plasmonic nanostructures can provide another way to boost the photoresponses of detectors based on 2D layered semiconductors via hot electrons injection that are generated by the decay of the resonantly excited surface plasmons of the nanostructures.[307–309]

Normally, integration with metallic nanostructures can lead to a several-fold improvement in responsivities for 2D-layered semiconductors-based photodetectors at the wavelength range where plasmonic resonance occurs.[39,172,304–306] For example, Miao et al. reported a two-fold enhancement of photocurrent upon depositing Au nanoparticles sparsely onto a few-layer MoS_2-based phototransistor under 632 nm illumination.[305] A three-fold increase in photocurrent can be further attained by utilizing periodic Au nanoarrays with stronger plasmonic resonance enhancement (**Figure 15**a and b). The detection range of the photodetectors can also be extended to wavelengths beyond the absorption edge of the 2D layered semiconductors with the help of plasmonic enhancement. Recently, Wang and co-workers presented a bilayer MoS2 photodetector with the photoresponse extended to NIR range by exploiting plasmonic resonators.[309] The below-bandgap photocurrent originates from the injection of hot electrons that are generated via the surface plasmon nonradiative decay

in the Au nanostructures. Consequently, the device demonstrates the highest hot-electron-based responsivity of 5.2 A W^{-1} at 1070 nm, owing to trap-induced photoamplification.

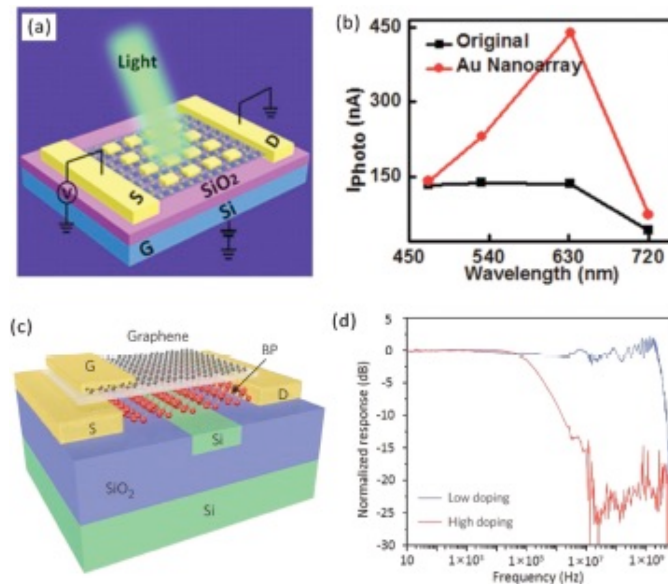

Figure 15. a) Schematic of a few-layer MoS_2 phototransistor decorated with Au nanoparticles. b) The photocurrent of the device as a function of illumination wavelength. Reproduced with permission.[305] Copyright 2015, Wiley-VCH. c) Three-dimensional illustration of a waveguide-integrated few-layer BP photodetector. d) The normalized photoresponse as a function of light modulation frequency when BP is gated to low and high doping, respectively. (c,d) Reproduced with permission.[313] Copyright 2015, Nature Publishing Group.

5.2. Optical Waveguides

Light-matter interaction enhancement can also be realized by integrating a 2D ultrathin flake with an optical waveguide, where an evanescent field at the boundaries of the waveguide can be absorbed by the flake to give rise to electron–hole pairs that contribute to the photocurrent. In addition to graphene based photodetectors,[310–312] this technique has been used to enhance the performance of a few-layer BP based detector.[313] In this study, a multilayer BP flake is integrated onto a silicon photonic waveguide with a few-layer graphene top gate (Figure 15c), which enables optimal interaction with light and tunability of the carrier type and concentration. The photocurrent generation mechanism is based on the photovoltaic effect for low-doped BP, while it changes to the bolometric effect for highly n-doped BP. When the flake is gated to be nearly intrinsic, the device with ≈11.5 nm BP reaches its optimal photoresponse with an intrinsic (extrinsic) responsivity of 135 mA W^{-1} (18.8 mA W^{-1}) at telecommunication band (≈1550 nm). Importantly, due to the finite bandgap of few-layer BP, the device exhibits a low dark current and gives rise to a depressed noise level, a significant advantage over its graphene counterparts. In addition, the detector shows a high response speed with a response roll-off frequency at 2.8 GHz for low doping, which decreases to 0.2 MHz for high doping due to the change of photocurrent

generation mechanism, as shown by the photoresponse as a function of light modulation frequency in Figure 15d.

5.3. Optical Microcavities

The integration of some 2D layered semiconductors with optical waveguides will not amount to obvious performance enhancement because of their relatively large bandgaps and thus negligible absorption in the telecommunication band. However, light-matter interaction enhancement is achievable by integrating these semiconductors with optical microcavities in the visible region. It has been recently reported that coupling MoS_2,[314] WSe_2,[315,316] and GaSe[317] with optical microcavities leads to greatly enhanced PL emitted in spectrally narrow and wavelength-tunable cavity modes and nanoscale, optically-pumped lasing with a very low threshold. This technique should be further developed to enhance device performance in broader wavelength regions for practical applications.

6. Conclusions and Outlook

In summary, the large family of 2D layered semiconductors that can absorb light over a broadband wavelengths from UV to NIR are ideal candidates for high-performance photodetectors. Various types of photodetectors, including photoconductors, phototransistors, and photodiodes, based on 2D layered semiconductors, have been systematically investigated by many groups focusing on device design, performance, and sensing mechanisms. More importantly, device performances have been successfully optimized by various approaches, paving the way for highly sensitive photodetectors with utility in many practical applications.

For photoconductors and phototransistors, devices based on 2D TMDs normally show very high responsivities and gains but slow response times, making them suitable for applications that only require high sensitivities. Devices based on other 2D layered semiconductors, including group IIIA, group IVA, and group IVB metal chalcogenides, generally show larger responsivities and faster response times than 2D MoS_2-based devices, rendering them promising candidates for sensitive photodetection in a broadband wavelength region. Few-layer-BP-based detectors show large responsivities in the UV-visible region and very fast responses at the telecommunication band, indicating that this material is potentially useful for sensitive photodetection and optical communication. Moreover, devices based on the hybrids of 2D layered semiconductors have shown ultra-high responsivities up to 108 A W^{-1} and an extended detectable wavelength range, providing an alternative means to realize high-performance devices.

Photodiodes based on 2D layered semiconductors have been realized with the following device designs: (1) PN junctions based on 2D materials, including WSe_2, $MoSe_2$ and few-layer BP, with properties controllable by local electrostatic gating; (2) Vertical or lateral heterostructures with 2D layered semi-conductors sandwiched between graphene layers or integrated with other 2D layered semiconductors by mechanical stacking or direct synthesis; (3) Vertical or lateral homojunctions based on 2D layered semiconductors with different doping regions;(4) van der Waal heterojunctions based

on the integration of a 2D layered semiconductor with other semiconductors such as bulk Si; and (5) Schottky barrier diodes formed between 2D layered semiconductors and metals. Although the responsivities of photodiodes are normally lower than those of phototransistors, the response times of the former are much faster than those of the latter devices. As evidenced by many examples, the 2D photodiodes have shown great promise in photodetection and light harvesting, especially for flexible or semitransparent systems. Moreover, manipulating photocarrier generation, separation, and transport in the photodiodes has enabled us to better understand the underlying working mechanisms and have pro-vided guidelines for device optimization.

In future work, there are many challenges left in this field. To realize high-performance photodetectors, we need to have rational device designs and suitable materials for the different parts of the device. We envision that 2D-material-based photodetectors can be further developed in several directions. Firstly, novel 2D materials should be synthesized and used in devices to meet some specific requirement for practical applications. Secondly, novel approaches for chemical doping and surface treatment of 2D materials should be investigated, which is a feasible strategy for improving or manipulating device performance. Thirdly, optical approaches, including plasmonic technologies, optical waveguides, and microcavities, are very useful in enhancing the light absorption of 2D materials and thus can be incorporated in the devices to increase the sensitivities. For practical applications, the uniformity, stability, large-scale production and cost of the devices are critical issues that must be tackled. More importantly, 2D photodetectors should find some commercial applications at this stage because their performances already exceed those of conventional semiconductor devices; however, this has never been achieved until now. One feasible step towards commercial applications is to integrate 2D materials with devices having the existing pho-tonic and microelectronic platforms, such as CMOS technologies. This remains a grand challenge to be solved in the future.

Acknowledgements

This work is financially supported by the Research Grants Council (RGC) of Hong Kong, China (Project No. C5015-15G), and The Hong Kong Polytechnic University (Project No. 1-BBA3, A-PL49).

Reference

[1] K. S. Novoselov, D. Jiang, F. Schedin, T. J. Booth, V. V Khotkevich, S. V Morozov, A. K. Geim, Proc. Natl. Acad. Sci. 2005, 102, 10451.

[2] B. Radisavljevic, A. Radenovic, J. Brivio, V. Giacometti, A. Kis, Nat. Nanotechnol. 2011, 6, 147.

[3] M. Xu, T. Liang, M. Shi, H. Chen, Chem. Rev. 2013, 113, 3766.

[4] S. Z. Butler, S. M. Hollen, L. Cao, Y. Cui, J. A. Gupta, H. R. Gutiérrez, T. F. Heinz, S. S. Hong, J. Huang, A. F. Ismach, E. Johnston-Halperin, M. Kuno, V. V. Plashnitsa, R. D. Robinson, R. S. Ruoff, S. Salahuddin, J. Shan, L. Shi, M. G. Spencer, M. Terrones, W. Windl, J. E. Goldberger, ACS Nano 2013, 7, 2898.

[5] H. Li, J. Wu, Z. Yin, H. Zhang, Acc. Chem. Res. 2014, 47, 1067.

[6] M. Chhowalla, H. S. Shin, G. Eda, L.-J. Li, K. P. Loh, H. Zhang, Nat. Chem. 2013, 5, 263.

[7] G. Eda, H. Yamaguchi, D. Voiry, T. Fujita, M. Chen, M. Chhowalla, Nano Lett. 2011, 11, 5111.

[8] J. N. Coleman, M. Lotya, A. O'Neill, S. D. Bergin, P. J. King, U. Khan, K. Young, A. Gaucher, S. De, R. J. Smith, I. V Shvets, S. K. Arora, G. Stanton, H.-Y. Kim, K. Lee, G. T. Kim, G. S. Duesberg, T. Hallam, J. J. Boland, J. J. Wang, J. F. Donegan, J. C. Grunlan, G. Moriarty, A. Shmeliov, R. J. Nicholls, J. M. Perkins, E. M. Grieveson, K. Theuwissen, D. W. McComb, P. D. Nellist, V. Nicolosi, Science 2011, 331, 568.

[9] K. S. Novoselov, Science 2004, 306, 666.

[10] M. J. Allen, V. C. Tung, R. B. Kaner, Chem. Rev. 2010, 110, 132.

[11] K. S. Novoselov, V. I. Fal ko, L. Colombo, P. R. Gellert, M. G. Schwab, K. Kim, Nature 2012, 490, 192.

[12] E. J. H. Lee, K. Balasubramanian, R. T. Weitz, M. Burghard, K. Kern, Nat. Nanotechnol. 2008, 3, 486.

[13] K. F. Mak, L. Ju, F. Wang, T. F. Heinz, Solid State Commun. 2012, 152, 1341.

[14] F. Xia, H. Yan, P. Avouris, Proc. IEEE 2013, 101, 1717.

[15] Z. Sun, H. Chang, ACS Nano 2014, 8, 4133.

[16] F. H. L. Koppens, T. Mueller, P. Avouris, A. C. Ferrari, M. S. Vitiello, M. Polini, Nat. Nanotechnol. 2014, 9, 780.

[17] J. Li, L. Niu, Z. Zheng, F. Yan, Adv. Mater. 2014, 26, 5239.

[18] F. Bonaccorso, Z. Sun, T. Hasan, A. C. Ferrari, Nat. Photonics 2010, 4, 611.

[19] F. Xia, T. Mueller, Y. Lin, A. Valdes-Garcia, P. Avouris, Nat. Nanotechnol. 2009, 4, 839.

[20] W. Bao, L. Jing, J. Velasco, Y. Lee, G. Liu, D. Tran, B. Standley, M. Aykol, S. B. Cronin, D. Smirnov, M. Koshino, E. McCann, M. Bockrath, C. N. Lau, Nat. Phys. 2011, 7, 948.

[21] A. Gupta, T. Sakthivel, S. Seal, Prog. Mater. Sci. 2015, 73, 44.

[22] Y. Shi, H. Li, L.-J. Li, Chem. Soc. Rev. 2015, 44, 2744.

[23] D. Jariwala, V. K. Sangwan, L. J. Lauhon, T. J. Marks, M. C. Hersam, ACS Nano 2014, 8, 1102.

[24] X. Duan, C. Wang, A. Pan, R. Yu, X. Duan, Chem. Soc. Rev. 2015, 44, 8859.

[25] L. Li, Y. Yu, G. J. Ye, Q. Ge, X. Ou, H. Wu, D. Feng, X. H. Chen, Y. Zhang,

Nat. Nanotechnol. 2014, 9, 372.

[26] H. Liu, Y. Du, Y. Deng, P. D. Ye, Chem. Soc. Rev. 2015, 44, 2732.

[27] F. Xia, H. Wang, D. Xiao, M. Dubey, A. Ramasubramaniam, Nat. Photonics 2014, 8, 899.

[28] K. F. Mak, J. Shan, Nat. Photonics 2016, 10, 216.

[29] K. F. Mak, C. Lee, J. Hone, J. Shan, T. F. Heinz, Phys. Rev. Lett. 2010, 105, 136805.

[30] W. Jin, P.-C. Yeh, N. Zaki, D. Zhang, J. T. Sadowski, A. Al-Mahboob, A. M. van der Zande, D. A. Chenet, J. I. Dadap, I. P. Herman, P. Sutter, J. Hone, R. M. Osgood, Phys. Rev. Lett. 2013, 111, 106801.

[31] A. Ayari, E. Cobas, O. Ogundadegbe, M. S. Fuhrer, J. Appl. Phys. 2007, 101, 014507.

[32] A. Splendiani, L. Sun, Y. Zhang, T. Li, J. Kim, C.-Y. Chim, G. Galli, F. Wang, Nano Lett. 2010, 10, 1271.

[33] H. Liu, A. T. Neal, Z. Zhu, Z. Luo, X. Xu, D. Tománek, P. D. Ye, ACS Nano 2014, 8, 4033.

[34] V. Tran, R. Soklaski, Y. Liang, L. Yang, Phys. Rev. B 2014, 89, 235319.

[35] K. F. Mak, K. He, J. Shan, T. F. Heinz, Nat. Nanotechnol. 2012, 7, 494.

[36] K. F. Mak, K. He, C. Lee, G. H. Lee, J. Hone, T. F. Heinz, J. Shan, Nat. Mater. 2012, 12, 207.

[37] M. Buscema, J. O. Island, D. J. Groenendijk, S. I. Blanter, G. A. Steele, H. S. J. van der Zant, A. Castellanos-Gomez, Chem. Soc. Rev. 2015, 44, 3691.

[38] D. Akinwande, N. Petrone, J. Hone, Nat. Commun. 2014, 5, 5678.

[39] L. Britnell, R. M. Ribeiro, A. Eckmann, R. Jalil, B. D. Belle, Mishchenko, Y.-J. Kim, R. V Gorbachev, T. Georgiou, S. V Morozov, A. N. Grigorenko, A. K. Geim, C. Casiraghi, A. H. C. Neto, K. S. Novoselov, Science 2013, 340, 1311.

[40] W. S. Yun, S. W. Han, S. C. Hong, I. G. Kim, J. D. Lee, Phys. Rev. B 2012, 85, 033305.

[41] A. Castellanos-Gomez, M. Poot, G. A. Steele, H. S. J. van der Zant, N. Agraït, G. Rubio-Bollinger, Adv. Mater. 2012, 24, 772.

[42] K. He, C. Poole, K. F. Mak, J. Shan, Nano Lett. 2013, 13, 2931.

[43] C. R. Zhu, G. Wang, B. L. Liu, X. Marie, X. F. Qiao, X. Zhang, X. X. Wu, H. Fan, P. H. Tan, T. Amand, B. Urbaszek, Phys. Rev. B 2013, 88, 121301.

[44] A. K. Geim, I. V Grigorieva, Nature 2013, 499, 419.

[45] M.-Y. Li, C.-H. Chen, Y. Shi, L.-J. Li, Mater. Today 2015.

[46] S. Das, M. Kim, J. Lee, W. Choi, Crit. Rev. Solid State Mater. Sci. 2014, 39, 231.

[47] Y.-H. Lee, X.-Q. Zhang, W. Zhang, M.-T. Chang, C.-T. Lin, K.-D. Chang, Y.-C. Yu, J. T.-W. Wang, C.-S. Chang, L.-J. Li, T.-W. Lin, Adv. Mater. 2012, 24, 2320.

[48] S. Das, J. Appenzeller, Appl. Phys. Lett. 2013, 103, 103501.

[49] N. R. Pradhan, D. Rhodes, Y. Xin, S. Memaran, L. Bhaskaran, M. Siddiq, S. Hill, P. M. Ajayan, L. Balicas, ACS Nano 2014, 8, 7923.

[50] D. Kiriya, M. Tosun, P. Zhao, J. S. Kang, A. Javey, J. Am. Chem. Soc. 2014, 136, 7853.

[51] H. Fang, M. Tosun, G. Seol, T. C. Chang, K. Takei, J. Guo, A. Javey, Nano Lett. 2013, 13, 1991.

[52] D. Xiang, C. Han, J. Wu, S. Zhong, Y. Liu, J. Lin, X.-A. Zhang, W. Ping Hu, B. Özyilmaz, A. H. C. Neto, A. T. S. Wee, W. Chen, Nat. Commun. 2015, 6, 6485.

[53] S. Das, J. A. Robinson, M. Dubey, H. Terrones, M. Terrones, Annu. Rev. Mater. Res. 2015, 45, 1.

[54] S. Tongay, J. Zhou, C. Ataca, K. Lo, T. S. Matthews, J. Li, J. C. Grossman, J. Wu, Nano Lett. 2012, 12, 5576.

[55] T. Georgiou, R. Jalil, B. D. Belle, L. Britnell, R. V Gorbachev, S. V Morozov, Y.-J. Kim, A. Gholinia, S. J. Haigh, O. Makarovsky, L. Eaves, L. A. Ponomarenko, A. K. Geim, K. S. Novoselov, Mishchenko, Nat. Nanotechnol. 2012, 8, 100.

[56] A. M. Jones, H. Yu, N. J. Ghimire, S. Wu, G. Aivazian, J. S. Ross, Zhao, J. Yan, D. G. Mandrus, D. Xiao, W. Yao, X. Xu, Nat. Nano- technol. 2013, 8, 634.

[57] Y. Li, Y. Rao, K. F. Mak, Y. You, S. Wang, C. R. Dean, T. F. Heinz, Nano Lett. 2013, 13, 3329.

[58] G. Cunningham, M. Lotya, C. S. Cucinotta, S. Sanvito, S. D. Bergin, R. Menzel, M. S. P. Shaffer, J. N. Coleman, ACS Nano 2012, 6, 3468.

[59] R. J. Smith, P. J. King, M. Lotya, C. Wirtz, U. Khan, S. De, A. O'Neill, G. S. Duesberg, J. C. Grunlan, G. Moriarty, J. Chen, J. Wang, A. I. Minett, V. Nicolosi, J. N. Coleman, Adv. Mater. 2011, 23, 3944.

[60] C. Zhi, Y. Bando, C. Tang, H. Kuwahara, D. Golberg, Adv. Mater. 2009, 21, 2889.

[61] Q. Tang, Z. Zhou, Prog. Mater. Sci. 2013, 58, 1244.

[62] J. Feng, L. Peng, C. Wu, X. Sun, S. Hu, C. Lin, J. Dai, J. Yang, Y. Xie, Adv. Mater. 2012, 24, 1969.

[63] A. A. Green, M. C. Hersam, Nano Lett. 2009, 9, 4031.

[64] R. F. Frindt, A. S. Arrott, A. E. Curzon, B. Heinrich, S. R. Morrison, T. L. Templeton, R. Divigalpitiya, M. A. Gee, P. Joensen, P. J. Schurer, J. L. LaCombe, J. Appl. Phys. 1991, 70, 6224.

[65] H.-L. Tsai, J. Heising, J. L. Schindler, C. R. Kannewurf, M. G. Kanatzidis, Chem. Mater. 1997, 9, 879.

[66] Z. Zeng, Z. Yin, X. Huang, H. Li, Q. He, G. Lu, F. Boey, H. Zhang, Angew. Chemie Int. Ed. 2011, 50, 11093.

[67] Z. Zeng, T. Sun, J. Zhu, X. Huang, Z. Yin, G. Lu, Z. Fan, Q. Yan, H. H. Hng, H. Zhang, Angew. Chemie Int. Ed. 2012, 51, 9052.

[68] J. Zhang, H. Yu, W. Chen, X. Tian, D. Liu, M. Cheng, G. Xie, W. Yang, R. Yang, X. Bai, D. Shi, G. Zhang, ACS Nano 2014, 8, 6024.

[69] Y. H. Lee, L. Yu, H. Wang, W. Fang, X. Ling, Y. Shi, C. Te Lin, J. K. Huang, M. T. Chang, C. S. Chang, M. Dresselhaus, T. Palacios, L. J. Li, J. Kong, Nano Lett. 2013, 13, 1852.

[70] Y.-C. Lin, W. Zhang, J.-K. Huang, K.-K. Liu, Y.-H. Lee, C.-T. Liang, C.-W. Chu, L.-J. Li, Nanoscale 2012, 4, 6637.

[71] Y. Zhan, Z. Liu, S. Najmaei, P. M. Ajayan, J. Lou, Small 2012, 8, 966.

[72] K. K. Liu, W. Zhang, Y. H. Lee, Y. C. Lin, M. T. Chang, C. Y. Su, C. S. Chang, H. Li, Y. Shi, H. Zhang, C. S. Lai, L. J. Li, Nano Lett. 2012, 12, 1538.

[73] K. Kang, S. Xie, L. Huang, Y. Han, P. Y. Huang, K. F. Mak, C.-J. Kim, D. Muller, J. Park, Nature 2015, 520, 656.

[74] R. H. Bube, Photoelectronic Properties of Semiconductors, Cam- bridge University Press, Cambridge 1992.

[75] J. Watson, Opt. Laser Technol. 1992, 24, 177.

[76] G. Konstantatos, E. H. Sargent, Nat. Nanotechnol. 2010, 5, 391.

[77] G. Konstantatos, M. Badioli, L. Gaudreau, J. Osmond, M. Bernechea, F. P. G. de Arquer, F. Gatti, F. H. L. Koppens, Nat. Nanotechnol. 2012, 7, 363.

[78] Z. Sun, Z. Liu, J. Li, G. Tai, S.-P. Lau, F. Yan, Adv. Mater. 2012, 24, 5878.

[79] S. M. Sze, K. K. Ng, Physics of Semiconductor Devices, 2nd Edition, Wiley, New York 1981.

[80] X. Xu, N. M. Gabor, J. S. Alden, A. M. van der Zande, P. L. McEuen, Nano Lett. 2010, 10, 562.

[81] J. C. W. Song, M. S. Rudner, C. M. Marcus, L. S. Levitov, Nano Lett. 2011, 11, 4688.

[82] R. W. Boyd, Radiometry and the Detection of Optical Radiation, John Wiley & Sons, Hoboken, NJ 1983.

[83] P. L. Richards, J. Appl. Phys. 1994, 76, 1.

[84] M. Freitag, T. Low, F. Xia, P. Avouris, Nat. Photonics 2012, 7, 53.

[85] L. Vicarelli, M. S. Vitiello, D. Coquillat, A. Lombardo, A. C. Ferrari, W. Knap, M. Polini, V. Pellegrini, A. Tredicucci, Nat. Mater. 2012, 11, 865.

[86] T. Low, A. S. Rodin, A. Carvalho, Y. Jiang, H. Wang, F. Xia, A. H. Castro Neto, Phys. Rev. B 2014, 90, 075434.

[87] J. Liu, Photonic Devices, Cambridge University Press, Cambridge 2005.

[88] Z. Yin, H. H. Li, H. H. Li, L. Jiang, Y. Shi, Y. Sun, G. Lu, Q. Zhang, X. Chen, H. Zhang, ACS Nano 2012, 6, 74.

[89] O. Lopez-Sanchez, D. Lembke, M. Kayci, A. Radenovic, A. Kis, Nat. Nanotechnol. 2013, 8, 497.

[90] H. S. Lee, S.-W. Min, Y.-G. Chang, M. K. Park, T. Nam, H. Kim, J. H. Kim, S. Ryu, S. Im, Nano Lett. 2012, 12, 3695.

[91] W. Choi, M. Y. Cho, A. Konar, J. H. Lee, G.-B. Cha, S. C. Hong, S. Kim, J. Kim, D. Jena, J. Joo, S. Kim, Adv. Mater. 2012, 24, 5832.

[92] M. M. Furchi, D. K. Polyushkin, A. Pospischil, T. Mueller, Nano Lett. 2014, 14, 6165.

[93] D.-S. Tsai, D.-H. Lien, M.-L. Tsai, S.-H. Su, K.-M. Chen, J.-J. Ke, Y.-C. Yu, L.-J. Li, J.-H. He, IEEE J. Sel. Top. Quantum Electron. 2014, 20, 30.

[94] M. F. Khan, M. W. Iqbal, M. Z. Iqbal, M. A. Shehzad, Y. Seo, J. Eom, ACS Appl. Mater. Interfaces 2014, 6, 21645.

[95] W. Zhang, J.-K. Huang, C.-H. Chen, Y.-H. Chang, Y.-J. Cheng, L.-J. Li, Adv. Mater. 2013, 25, 3456.

[96] F. Schedin, A. K. Geim, S. V. Morozov, E. W. Hill, P. Blake, M. I. Katsnelson, K. S. Novoselov, Nat. Mater. 2007, 6, 652.

[97] S. Tongay, J. Zhou, C. Ataca, J. Liu, J. S. Kang, T. S. Matthews, L. You, J. Li, J. C. Grossman, J. Wu, Nano Lett. 2013, 13, 2831.

[98] N. Perea-López, Z. Lin, N. R. Pradhan, A. Iñiguez-Rábago, A. Laura Elías, A. McCreary, J. Lou, P. M. Ajayan, H. Terrones, L. Balicas, M. Terrones, 2D Mater. 2014, 1, 011004.

[99] D.-S. Tsai, K.-K. Liu, D.-H. Lien, M.-L. Tsai, C.-F. Kang, C.-A. Lin, L.-J. Li, J.-H. He, ACS Nano 2013, 7, 3905.

[100] J. Li, M. M. Naiini, S. Vaziri, M. C. Lemme, M. Östling, Adv. Funct. Mater. 2014, 24, 6524.

[101] G. Cunningham, U. Khan, C. Backes, D. Hanlon, D. McCloskey, J. F. Donegan, J. N. Coleman, J. Mater. Chem. C 2013, 1, 6899.

[102] Z. P. Ling, R. Yang, J. W. Chai, S. J. Wang, W. S. Leong, Y. Tong, D. Lei, Q. Zhou, X. Gong, D. Z. Chi, K.-W. Ang, Opt. Express 2015, 23, 13580.

[103] Y. Lee, J. Yang, D. Lee, Y.-H. Kim, J.-H. Park, H. Kim, J. H. Cho, Nanoscale 2016, 8, 9193.

[104] J. Lu, J. H. Lu, H. Liu, B. Liu, K. X. Chan, J. Lin, W. Chen, K. P. Loh, C. H. Sow, ACS Nano 2014, 8, 6334.

[105] J. Kwon, Y. K. Hong, G. Han, I. Omkaram, W. Choi, S. Kim, Y. Yoon, Adv. Mater. 2015, 27, 2224.

[106] D. Kufer, G. Konstantatos, Nano Lett. 2015, 15, 7307.

[107] X. Wang, P. Wang, J. Wang, W. Hu, X. Zhou, N. Guo, H. Huang, S. Sun, H. Shen, T. Lin, M. Tang, L. Liao, A. Jiang, J. Sun, X. Meng, X. Chen, W. Lu, J. Chu, Adv. Mater. 2015, 27, 6575.

[108] H. S. Lee, S. S. Baik, K. Lee, S. Min, P. J. Jeon, J. S. Kim, K. Choi, H. J. Choi, J. H. Kim, S. Im, ACS Nano 2015, 9, 8312.

[109] Y. Pang, F. Xue, L. Wang, J. Chen, J. Luo, T. Jiang, C. Zhang, Z. L. Wang, Adv. Sci. 2016, 3, 1500419.

[110] J. D. Lin, C. Han, F. Wang, R. Wang, D. Xiang, S. Qin, X. A. Zhang, L. Wang, H. Zhang, A. T. S. Wee, W. Chen, ACS Nano 2014, 8, 5323.

[111] D. H. Kang, M. S. Kim, J. Shim, J. Jeon, H. Y. Park, W. S. Jung, H. Y. Yu, C. H. Pang, S. Lee, J. H. Park, Adv. Funct. Mater. 2015, 25, 4219.

[112] A. Ramasubramaniam, D. Naveh, E. Towe, Phys. Rev. B 2011, 84, 205325.

[113] N. Zibouche, P. Philipsen, A. Kuc, T. Heine, Phys. Rev. B 2014, 90, 125440.

[114] H. Wang, C. Zhang, W. Chan, S. Tiwari, F. Rana, Nat. Commun. 2015, 6, 8831.

[115] M. Buscema, M. Barkelid, V. Zwiller, H. S. J. van der Zant, G. A. Steele, A. Castellanos-Gomez, Nano Lett. 2013, 13, 358.

[116] Y. Zhang, H. Li, L. Wang, H. Wang, X. Xie, S.-L. Zhang, R. Liu, Z.-J. Qiu, Sci. Rep. 2015, 5, 7938.

[117] Y. Zhang, T.-R. Chang, B. Zhou, Y.-T. Cui, H. Yan, Z. Liu, F. Schmitt, J. Lee, R. Moore, Y. Chen, H. Lin, H.-T. Jeng, S.-K. Mo, Z. Hussain, A. Bansil, Z.-X. Shen, Nat. Nanotechnol. 2013, 9, 111.

[118] J. S. Ross, S. Wu, H. Yu, N. J. Ghimire, A. M. Jones, G. Aivazian, J. Yan, D. G. Mandrus, D. Xiao, W. Yao, X. Xu, Nat. Commun. 2013, 4, 1474.

[119] S. Larentis, B. Fallahazad, E. Tutuc, Appl. Phys. Lett. 2012, 101, 223104.

[120] A. Abderrahmane, P. J. Ko, T. V Thu, S. Ishizawa, T. Takamura, A. Sandhu, Nanotechnology 2014, 25, 365202.

[121] X. Lu, M. I. B. Utama, J. Lin, X. Gong, J. Zhang, Y. Zhao, S. T. Pantelides, J. Wang, Z. Dong, Z. Liu, W. Zhou, Q. Xiong, Nano Lett. 2014, 14, 2419.

[122] X. Wang, Y. Gong, G. Shi, W. L. Chow, K. Keyshar, G. Ye, R. Vajtai, J. Lou, Z. Liu, E. Ringe, B. K. Tay, P. M. Ajayan, ACS Nano 2014, 8, 5125.

[123] G. W. Shim, K. Yoo, S.-B. Seo, J. Shin, D. Y. Jung, I.-S. Kang, C. W. Ahn, B. J. Cho, S.-Y. Choi, ACS Nano 2014, 8, 6655.

[124] Y.-H. Chang, W. Zhang, Y. Zhu, Y. Han, J. Pu, J.-K. Chang, W.-T. Hsu, J.-K. Huang, C.-L. Hsu, M.-H. Chiu, T. Takenobu, H. Li, C.-I. Wu, W.-H. Chang, A.

T. S. Wee, L.-J. Li, ACS Nano 2014, 8, 8582.

[125] J. Xia, X. Huang, L.-Z. Liu, M. Wang, L. Wang, B. Huang, D.-D. Zhu, J.-J. Li, C.-Z. Gu, X.-M. Meng, Nanoscale 2014, 6, 8949.

[126] C. Jung, S. M. Kim, H. Moon, G. Han, J. Kwon, Y. K. Hong, I. Omkaram, Y. Yoon, S. Kim, J. Park, Sci. Rep. 2015, 5, 15313.

[127] W. Sik Hwang, M. Remskar, R. Yan, V. Protasenko, K. Tahy, S. Doo Chae, P. Zhao, A. Konar, H. (Grace) Xing, A. Seabaugh, D. Jena, Appl. Phys. Lett. 2012, 101, 013107.

[128] S. Hwan Lee, D. Lee, W. Sik Hwang, E. Hwang, D. Jena, W. Jong Yoo, Appl. Phys. Lett. 2014, 104, 193113.

[129] N. Perea-López, A. L. Elías, A. Berkdemir, A. Castro-Beltran, H. R. Gutiérrez, S. Feng, R. Lv, T. Hayashi, F. López-Urías, S. Ghosh, B. Muchharla, S. Talapatra, H. Terrones, M. Terrones, Adv. Funct. Mater. 2013, 23, 5511.

[130] N. Huo, S. Yang, Z. Wei, S.-S. Li, J.-B. Xia, J. Li, Sci. Rep. 2014, 4, 5209.

[131] C. Lan, C. Li, Y. Yin, Y. Liu, Nanoscale 2015, 7, 5974.

[132] J. D. Yao, Z. Q. Zheng, J. M. Shao, G. W. Yang, Nanoscale 2015, 7, 14974.

[133] L. Zeng, L. Tao, C. Tang, B. Zhou, H. Long, Y. Chai, S. P. Lau, Y. H. Tsang, Sci. Rep. 2016, 6, 20343.

[134] W. Zhang, M.-H. Chiu, C.-H. Chen, W. Chen, L.-J. Li, A. T. S. Wee, ACS Nano 2014, 8, 8653.

[135] N. R. Pradhan, J. Ludwig, Z. Lu, D. Rhodes, M. M. Bishop, K. Thirunavukkuarasu, S. A. McGill, D. Smirnov, L. Balicas, ACS Appl. Mater. Interfaces 2015, 7, 12080.

[136] J. Chen, B. Liu, Y. Liu, W. Tang, C. T. Nai, L. Li, J. Zheng, L. Gao, Y. Zheng, H. S. Shin, H. Y. Jeong, K. P. Loh, Adv. Mater. 2015, 27, 6722.

[137] S.-H. Jo, D.-H. Kang, J. Shim, J. Jeon, M. H. Jeon, G. Yoo, J. Kim, J. Lee, G. Y. Yeom, S. Lee, H.-Y. Yu, C. Choi, J.-H. Park, Adv. Mater. 2016, 28, 4824.

[138] Y.-F. Lin, Y. Xu, S.-T. Wang, S.-L. Li, M. Yamamoto, A. Aparecido-Ferreira, W. Li, H. Sun, S. Nakaharai, W.-B. Jian, K. Ueno, K. Tsukagoshi, Adv. Mater. 2014, 26, 3263.

[139] C. Ruppert, O. B. Aslan, T. F. Heinz, Nano Lett. 2014, 14, 6231.

[140] N. R. Pradhan, D. Rhodes, S. Feng, Y. Xin, S. Memaran, B.-H. Moon, H. Terrones, M. Terrones, L. Balicas, ACS Nano 2014, 8, 5911.

[141] L. Yin, X. Zhan, K. Xu, F. Wang, Z. Wang, Y. Huang, Q. Wang, C. Jiang, J. He, Appl. Phys. Lett. 2016, 108, 043503.

[142] K. Xu, Z. Wang, F. Wang, Y. Huang, F. Wang, L. Yin, C. Jiang, J. He, Adv. Mater. 2015, 27, 7881.

[143] J. A. Wilson, A. D. Yoffe, Adv. Phys. 1969, 18, 193.

[144] S. Yang, S. Tongay, Y. Li, Q. Yue, J.-B. Xia, S.-S. Li, J. Li, S.-H. Wei, Nanoscale 2014, 6, 7226.

[145] S. Yang, S. Tongay, Q. Yue, Y. Li, B. Li, F. Lu, Sci. Rep. 2014, 4, 5442.

[146] E. Zhang, Y. Jin, X. Yuan, W. Wang, C. Zhang, L. Tang, S. Liu, P. Zhou, W. Hu, F. Xiu, Adv. Funct. Mater. 2015, 25, 4076.

[147] F. Liu, S. Zheng, X. He, A. Chaturvedi, J. He, W. L. Chow, T. R. Mion, X. Wang, J. Zhou, Q. Fu, H. J. Fan, B. K. Tay, L. Song, R.-H. He, C. Kloc, P. M. Ajayan, Z. Liu, Adv. Funct. Mater. 2016, 26, 1169.

[148] M. Hafeez, L. Gan, H. Li, Y. Ma, T. Zhai, Adv. Funct. Mater. 2016, 26, 4551.

[149] E. Liu, M. Long, J. Zeng, W. Luo, Y. Wang, Y. Pan, W. Zhou, B. Wang, W. Hu, Z. Ni, Y. You, X. Zhang, S. Qin, Y. Shi, K. Watanabe, T. Taniguchi, H. Yuan, H. Y. Hwang, Y. Cui, F. Miao, D. Xing, Adv. Funct. Mater. 2016, 26, 1938.

[150] S. Jo, H.-Y. Park, D. Kang, J. Shim, J. Jeon, S. Choi, M. Kim, Y. Park, J. Lee, Y. J. Song, S. Lee, J. Park, Adv. Mater. 2016, 28, 6711.

[151] J. Shim, A. Oh, D.-H. Kang, S. Oh, S. K. Jang, J. Jeon, M. H. Jeon, M. Kim, C. Choi, J. Lee, S. Lee, G. Y. Yeom, Y. J. Song, J.-H. Park, Adv. Mater. 2016, 28, 6985.

[152] P. Hu, L. Wang, M. Yoon, J. Zhang, W. Feng, X. Wang, Z. Wen, J. C. Idrobo, Y. Miyamoto, D. B. Geohegan, K. Xiao, Nano Lett. 2013, 13, 1649.

[153] P. Hu, Z. Wen, L. Wang, P. Tan, K. Xiao, ACS Nano 2012, 6, 5988.

[154] P. Hu, J. Zhang, M. Yoon, X.-F. Qiao, X. Zhang, W. Feng, P. Tan, W. Zheng, J. Liu, X. Wang, J. C. Idrobo, D. B. Geohegan, K. Xiao, Nano Res. 2014, 7, 694.

[155] F. Liu, H. Shimotani, H. Shang, T. Kanagasekaran, V. Zólyomi, N. Drummond, V. I. Fal'ko, K. Tanigaki, ACS Nano 2014, 8, 752.

[156] S. Yang, Y. Li, X. Wang, N. Huo, J.-B. Xia, S.-S. Li, J. Li, Nanoscale 2014, 6, 2582.

[157] Z. Wang, K. Xu, Y. Li, X. Zhan, M. Safdar, Q. Wang, F. Wang, J. He, ACS Nano 2014, 8, 4859.

[158] Y. Cao, K. Cai, P. Hu, L. Zhao, T. Yan, W. Luo, X. Zhang, X. Wu, K. Wang, H. Zheng, Sci. Rep. 2015, 5, 8130.

[159] S. Lei, L. Ge, Z. Liu, S. Najmaei, G. Shi, G. You, J. Lou, R. Vajtai, P. M. Ajayan, Nano Lett. 2013, 13, 2777.

[160] M. Mahjouri-Samani, R. Gresback, M. Tian, K. Wang, A. A. Puretzky, C. M. Rouleau, G. Eres, I. N. Ivanov, K. Xiao, M. A. McGuire, G. Duscher, D. B. Geohegan, Adv. Funct. Mater. 2014, 24, 6365.

[161] X. Li, M.-W. Lin, A. A. Puretzky, J. C. Idrobo, C. Ma, M. Chi, M. Yoon, C. M. Rouleau, I. I. Kravchenko, D. B. Geohegan, K. Xiao, Sci. Rep. 2014, 4, 5497.

[162] Z. Wang, M. Safdar, M. Mirza, K. Xu, Q. Wang, Y. Huang, F. Wang, X. Zhan, J. He, Nanoscale 2015, 7, 7252.

[163] M. Lin, D. Wu, Y. Zhou, W. Huang, W. Jiang, W. Zheng, S. Zhao, C. Jin, Y. Guo, H. Peng, Z. Liu, J. Am. Chem. Soc. 2013, 135, 13274.

[164] R. B. Jacobs-Gedrim, M. Shanmugam, N. Jain, C. A. Durcan, M. T. Murphy, T. M. Murray, R. J. Matyi, R. L. Moore, B. Yu, ACS Nano 2014, 8, 514.

[165] J. Zhou, Q. Zeng, D. Lv, L. Sun, L. Niu, W. Fu, F. Liu, Z. Shen, C. Jin, Z. Liu, Nano Lett. 2015, 15, 6400.

[166] J. O. Island, S. I. Blanter, M. Buscema, H. S. J. van der Zant, A. Castellanos-Gomez, Nano Lett. 2015, 15, 7853.

[167] W. Zheng, T. Xie, Y. Zhou, Y. L. Chen, W. Jiang, S. Zhao, J. Wu, Y. Jing, Y. Wu, G. Chen, Y. Guo, J. Yin, S. Huang, H. Q. Xu, Z. Liu, H. Peng, Nat. Commun. 2015, 6, 6972.

[168] S. Lei, L. Ge, S. Najmaei, A. George, R. Kappera, J. Lou, M. Chhowalla, H. Yamaguchi, G. Gupta, R. Vajtai, A. D. Mohite, P. M. Ajayan, ACS Nano 2014, 8, 1263.

[169] S. R. Tamalampudi, Y.-Y. Lu, U. R. Kumar, R. Sankar, C.-D. Liao, B. K. Moorthy, C.-H. Cheng, F. C. Chou, Y.-T. Chen, Nano Lett. 2014, 14, 2800.

[170] W. Feng, J.-B. Wu, X. Li, W. Zheng, X. Zhou, K. Xiao, W. Cao, B. Yang, J.-C. Idrobo, L. Basile, W. Tian, P. Tan, P. Hu, J. Mater. Chem. C 2015, 3, 7022.

[171] W. Luo, Y. Cao, P. Hu, K. Cai, Q. Feng, F. Yan, T. Yan, X. Zhang, K. Wang, Adv. Opt. Mater. 2015, 3, 1418.

[172] S. Lei, F. Wen, L. Ge, S. Najmaei, A. George, Y. Gong, W. Gao, Z. Jin, B. Li, J. Lou, J. Kono, R. Vajtai, P. Ajayan, N. J. Halas, Nano Lett. 2015, 15, 3048.

[173] J. Jasinski, W. Swider, J. Washburn, Z. Liliental-Weber, A. Chaiken, K. Nauka, G. A. Gibson, C. C. Yang, Appl. Phys. Lett. 2002, 81, 4356.

[174] T. Zhai, X. Fang, M. Liao, X. Xu, L. Li, B. Liu, Y. Koide, Y. Ma, J. Yao, Y. Bando, D. Golberg, ACS Nano 2010, 4, 1596.

[175] K. Lai, H. Peng, W. Kundhikanjana, D. T. Schoen, C. Xie, S. Meister, Y. Cui, M. A. Kelly, Z.-X. Shen, Nano Lett. 2009, 9, 1265.

[176] G. W. Mudd, S. A. Svatek, T. Ren, A. Patanè, O. Makarovsky, L. Eaves, P. H. Beton, Z. D. Kovalyuk, G. V. Lashkarev, Z. R. Kudrynskyi, A. I. Dmitriev, Adv. Mater. 2013, 25, 5714.

[177] Y. Huang, E. Sutter, J. T. Sadowski, M. Cotlet, O. L. A. Monti, D. A. Racke, M. R. Neupane, D. Wickramaratne, R. K. Lake, B. A. Parkinson, P. Sutter, ACS Nano 2014, 8, 10743.

[178] G. Su, V. G. Hadjiev, P. E. Loya, J. Zhang, S. Lei, S. Maharjan, P. Dong, P. M. Ajayan, J. Lou, H. Peng, Nano Lett. 2015, 15, 506.

[179] Y. Huang, H.-X. Deng, K. Xu, Z.-X. Wang, Q.-S. Wang, F.-M. Wang, F.

Wang, X.-Y. Zhan, S.-S. Li, J.-W. Luo, J. He, Nanoscale 2015, 7, 14093.

[180] D. Yang, B. Li, C. Hu, H. Deng, D. Dong, X. Yang, K. Qiao, S. Yuan, H. Song, Adv. Opt. Mater. 2016, 4, 419.

[181] J. Xia, D. Zhu, L. Wang, B. Huang, X. Huang, X.-M. Meng, Adv. Funct. Mater. 2015, 25, 4255.

[182] Y. Tao, X. Wu, W. Wang, J. Wang, J. Mater. Chem. C 2015, 3, 1347.

[183] X. Zhou, L. Gan, W. Tian, Q. Zhang, S. Jin, H. Li, Y. Bando, D. Golberg, T. Zhai, Adv. Mater. 2015, 27, 8035.

[184] Y. Huang, K. Xu, Z. Wang, T. A. Shifa, Q. Wang, F. Wang, C. Jiang, J. He, Nanoscale 2015, 7, 17375.

[185] P. Yu, X. Yu, W. Lu, H. Lin, L. Sun, K. Du, F. Liu, W. Fu, Q. Zeng, Z. Shen, C. Jin, Q. J. Wang, Z. Liu, Adv. Funct. Mater. 2016, 26, 137.

[186] D.-J. Xue, J. Tan, J.-S. Hu, W. Hu, Y.-G. Guo, L.-J. Wan, Adv. Mater. 2012, 24, 4528.

[187] R. K. Ulaganathan, Y.-Y. Lu, C.-J. Kuo, S. R. Tamalampudi, R. Sankar, K. M. Boopathi, A. Anand, K. Yadav, R. J. Mathew, C.-R. Liu, F. C. Chou, Y.-T. Chen, Nanoscale 2016, 8, 2284.

[188] R. Schlaf, N. Armstrong, B. Parkinson, C. Pettenkofer, W. Jaegermann, Surf. Sci. 1997, 385, 1.

[189] Y. Sun, H. Cheng, S. Gao, Z. Sun, Q. Liu, Q. Liu, F. Lei, T. Yao, J. He, S. Wei, Y. Xie, Angew. Chemie Int. Ed. 2012, 51, 8727.

[190] S. G. Hickey, C. Waurisch, B. Rellinghaus, A. Eychmüller, J. Am. Chem. Soc. 2008, 130, 14978.

[191] D. D. VaughnII, R. J. Patel, M. A. Hickner, R. E. Schaak, J. Am. Chem. Soc. 2010, 132, 15170.

[192] L. Li, Z. Chen, Y. Hu, X. Wang, T. Zhang, W. Chen, Q. Wang, J. Am. Chem. Soc. 2013, 135, 1213.

[193] J. Kang, H. Sahin, H. D. Ozaydin, R. T. Senger, F. M. Peeters, Phys. Rev. B 2015, 92, 075413.

[194] W. Schairer, M. W. Shafer, Phys. Status Solidi 1973, 17, 181.

[195] D. Pacilé, M. Papagno, M. Lavagnini, H. Berger, L. Degiorgi, M. Grioni, Phys. Rev. B 2007, 76, 155406.

[196] J. O. Island, M. Buscema, M. Barawi, J. M. Clamagirand, J. R. Ares, C. Sánchez, I. J. Ferrer, G. A. Steele, H. S. J. van der Zant, A. Castellanos-Gomez, Adv. Opt. Mater. 2014, 2, 641.

[197] Y.-R. Tao, X.-C. Wu, W.-W. Xiong, Small 2014, 10, 4905.

[198] Y.-R. Tao, J.-J. Wu, X.-C. Wu, Nanoscale 2015, 7, 14292.

[199] W.-W. Xiong, J.-Q. Chen, X.-C. Wu, J.-J. Zhu, J. Mater. Chem. C 2014, 2, 7392.

[200] W.-W. Xiong, J.-Q. Chen, X.-C. Wu, J.-J. Zhu, J. Mater. Chem. C 2015, 3, 1929.

[201] L. M. Xie, Nanoscale 2015, 7, 18392.

[202] C. Tan, P. Yu, Y. Hu, J. Chen, Y. Huang, Y. Cai, Z. Luo, B. Li, Q. Lu, L. Wang, Z. Liu, H. Zhang, J. Am. Chem. Soc. 2015, 137, 10430.

[203] W. Feng, W. Zheng, P. Hu, Phys. Chem. Chem. Phys. 2014, 16, 19340.

[204] Q. Wang, K. Xu, Z. Wang, F. Wang, Y. Huang, M. Safdar, X. Zhan, F. Wang, Z. Cheng, J. He, Nano Lett. 2015, 15, 1183.

[205] V. Klee, E. Preciado, D. Barroso, A. E. Nguyen, C. Lee, K. J. Erickson, M. Triplett, B. Davis, I. H. Lu, S. Bobek, J. McKinley, J. P. Martinez, J. Mann, A. A. Talin, L. Bartels, F. Léonard, Nano Lett. 2015, 15, 2612.

[206] N. Kohara, S. Nishiawaki, T. Negami, T. Wada, Jpn. J. Appl. Phys. 2000, 39, 6316.

[207] S. Lei, A. Sobhani, F. Wen, A. George, Q. Wang, Y. Huang, P. Dong, B. Li, S. Najmaei, J. Bellah, G. Gupta, A. D. Mohite, L. Ge, J. Lou, N. J. Halas, R. Vajtai, P. Ajayan, Adv. Mater. 2014, 26, 7666.

[208] P. Perumal, R. K. Ulaganathan, R. Sankar, Y.-M. Liao, T.-M. Sun, M.-W. Chu, F. C. Chou, Y.-T. Chen, M.-H. Shih, Y.-F. Chen, Adv. Funct. Mater. 2016, 26, 3630.

[209] Y. Akahama, S. Endo, S. Narita, J. Phys. Soc. Japan 1983, 52, 2148.

[210] S. Narita, Y. Akahama, Y. Tsukiyama, K. Muro, S. Mori, S. Endo, M. Taniguchi, M. Seki, S. Suga, A. Mikuni, H. Kanzaki, Phys. B C 1983, 117–118, 422.

[211] Y. Maruyama, S. Suzuki, K. Kobayashi, S. Tanuma, Phys. B+C 1981, 105, 99.

[212] F. Xia, H. Wang, Y. Jia, Nat. Commun. 2014, 5, 4458.

[213] A. S. Rodin, A. Carvalho, A. H. Castro Neto, Phys. Rev. Lett. 2014, 112, 176801.

[214] J. Qiao, X. Kong, Z.-X. Hu, F. Yang, W. Ji, Nat. Commun. 2014, 5, 4475.

[215] X. Wang, A. M. Jones, K. L. Seyler, V. Tran, Y. Jia, H. Zhao, H. Wang, L. Yang, X. Xu, F. Xia, Nat. Nanotechnol. 2015, 10, 517.

[216] M. Buscema, D. J. Groenendijk, S. I. Blanter, G. A. Steele, H. S. J. van der Zant, A. Castellanos-Gomez, Nano Lett. 2014, 14, 3347.

[217] T. Hong, B. Chamlagain, W. Lin, H.-J. Chuang, M. Pan, Z. Zhou, Y.-Q. Xu, Nanoscale 2014, 6, 8978.

[218] J. Wu, G. K. W. Koon, D. Xiang, C. Han, C. T. Toh, E. S. Kulkarni,

Verzhbitskiy, A. Carvalho, A. S. Rodin, S. P. Koenig, G. Eda, Chen, A. H. C. Neto, B. Özyilmaz, ACS Nano 2015, 9, 8070.

[219] M. Huang, M. Wang, C. Chen, Z. Ma, X. Li, J. Han, Y. Wu, Adv. Mater. 2016, 28, 3481.

[220] M. Engel, M. Steiner, P. Avouris, Nano Lett. 2014, 14, 6414.

[221] L. Viti, J. Hu, D. Coquillat, W. Knap, A. Tredicucci, A. Politano, M. S. Vitiello, Adv. Mater. 2015, 27, 5567.

[222] K. Roy, M. Padmanabhan, S. Goswami, T. P. Sai, G. Ramalingam, S. Raghavan, A. Ghosh, Nat. Nanotechnol. 2013, 8, 826.

[223] W. Zhang, C.-P. Chuu, J.-K. Huang, C.-H. Chen, M.-L. Tsai, Y.-H. Chang, C.-T. Liang, Y.-Z. Chen, Y.-L. Chueh, J.-H. He, M.-Y. Chou, L.-J. Li, Sci. Rep. 2014, 4, 3826.

[224] H. Xu, J. Wu, Q. Feng, N. Mao, C. Wang, J. Zhang, Small 2014, 10, 2300.

[225] X. Li, J. Wu, N. Mao, J. Zhang, Z. Lei, Z. Liu, H. Xu, Carbon 2015, 92, 126.

[226] D. Ma, J. Shi, Q. Ji, K. Chen, J. Yin, Y. Lin, Y. Zhang, M. Liu, Q. Feng, X. Song, X. Guo, J. Zhang, Y. Zhang, Z. Liu, Nano Res. 2015, 8, 3662.

[227] J. Yang, H. Kwak, Y. Lee, Y.-S. Kang, M.-H. Cho, J. H. Cho, Y.-H. Kim, S.-J. Jeong, S. Park, H.-J. Lee, H. Kim, ACS Appl. Mater. Interfaces 2016, 8, 8576.

[228] H. Qiao, J. Yuan, Z. Xu, C. Chen, S. Lin, Y. Wang, J. Song, Y. Liu, Q. Khan, H. Y. Hoh, C.-X. Pan, S. Li, Q. Bao, ACS Nano 2015, 9, 1886.

[229] Z. Chen, J. Biscaras, A. Shukla, Nanoscale 2015, 7, 5981.

[230] D. Kufer, I. Nikitskiy, T. Lasanta, G. Navickaite, F. H. L. Koppens, G. Konstantatos, Adv. Mater. 2015, 27, 176.

[231] J. Schornbaum, B. Winter, S. P. Schießl, F. Gannott, G. Katsukis, D. M. Guldi, E. Spiecker, J. Zaumseil, Adv. Funct. Mater. 2014, 24, 5798.

[232] C. Chen, H. Qiao, S. Lin, C. Man Luk, Y. Liu, Z. Xu, J. Song, Y. Xue, D. Li, J. Yuan, W. Yu, C. Pan, S. Ping Lau, Q. Bao, Sci. Rep. 2015, 5, 11830.

[233] Y. Huang, X. Zhan, K. Xu, L. Yin, Z. Cheng, C. Jiang, Z. Wang, J. He, Appl. Phys. Lett. 2016, 108, 013101.

[234] S. H. Yu, Y. Lee, S. K. Jang, J. Kang, J. Jeon, C. Lee, J. Y. Lee, H. Kim, E. Hwang, S. Lee, J. H. Cho, ACS Nano 2014, 8, 8285.

[235] E. H. Cho, W. G. Song, C. J. Park, J. Kim, S. Kim, J. Joo, Nano Res. 2015, 8, 790.

[236] C. Ma, Y. Shi, W. Hu, M. H. Chiu, Z. Liu, A. Bera, F. Li, H. Wang, L. J. Li, T. Wu,. Adv. Mater. 2016, 28, 3683.

[237] D. Kang, S. R. Pae, J. Shim, G. Yoo, J. Jeon, J. W. Leem, J. S. Yu, S. Lee, B. Shin, J.-H. Park, Adv. Mater. 2016, DOI: 10.1002/ adma.201600992.

[238] A. Pospischil, M. M. Furchi, T. Mueller, Nat. Nanotechnol. 2014, 9, 257.

[239] B. W. H. Baugher, H. O. H. Churchill, Y. Yang, P. Jarillo-Herrero, Nat. Nanotechnol. 2014, 9, 262.

[240] J. S. Ross, P. Klement, A. M. Jones, N. J. Ghimire, J. Yan, D. G. Mandrus, T. Taniguchi, K. Watanabe, K. Kitamura, W. Yao, D. H. Cobden, X. Xu, Nat. Nanotechnol. 2014, 9, 268.

[241] D. J. Groenendijk, M. Buscema, G. A. Steele, S. Michaelis de Vasconcellos, R. Bratschitsch, H. S. J. van der Zant, A. Castellanos- Gomez, Nano Lett. 2014, 14, 5846.

[242] M. Buscema, D. J. Groenendijk, G. a Steele, H. S. J. van der Zant, A. Castellanos-Gomez, Nat. Commun. 2014, 5, 4651.

[243] S. Memaran, N. R. Pradhan, Z. Lu, D. Rhodes, J. Ludwig, Q. Zhou, O. Ogunsolu, P. M. Ajayan, D. Smirnov, A. I. Fernández- Domínguez, F. J. García-Vidal, L. Balicas, Nano Lett. 2015, 15, 7532.

[244] C. R. Dean, A. F. Young, I. Meric, C. Lee, L. Wang, S. Sorgenfrei, K. Watanabe, T. Taniguchi, P. Kim, K. L. Shepard, J. Hone, Nat. Nanotechnol. 2010, 5, 722.

[245] F. Bonaccorso, A. Lombardo, T. Hasan, Z. Sun, L. Colombo, A. C. Ferrari, Mater. Today 2012, 15, 564.

[246] W. J. Yu, Y. Liu, H. Zhou, A. Yin, Z. Li, Y. Huang, X. Duan, Nat. Nanotechnol. 2013, 8, 952.

[247] M. Massicotte, P. Schmidt, F. Vialla, K. G. Schädler, A. Reserbat- Plantey, K. Watanabe, T. Taniguchi, K. J. Tielrooij, F. H. L. Koppens, Nat. Nanotechnol. 2015, 11, 42.

[248] G. W. Mudd, S. A. Svatek, L. Hague, O. Makarovsky, Z. R. Kudrynskyi, C. J. Mellor, P. H. Beton, L. Eaves, K. S. Novoselov, Z. D. Kovalyuk, E. E. Vdovin, A. J. Marsden, N. R. Wilson, A. Patanè, Adv. Mater. 2015, 27, 3760.

[249] H. Fang, C. Battaglia, C. Carraro, S. Nemsak, B. Ozdol, J. S. Kang, H. A. Bechtel, S. B. Desai, F. Kronast, A. A. Unal, G. Conti, C. Conlon, G. K. Palsson, M. C. Martin, A. M. Minor, C. S. Fadley, E. Yablonovitch, R. Maboudian, A. Javey, Proc. Natl. Acad. Sci. 2014, 111, 6198.

[250] X. Hong, J. Kim, S.-F. Shi, Y. Zhang, C. Jin, Y. Sun, S. Tongay, J. Wu, Y. Zhang, F. Wang, Nat. Nanotechnol. 2014, 9, 682.

[251] F. Ceballos, M. Z. Bellus, H.-Y. Chiu, H. Zhao, ACS Nano 2014, 8, 12717.

[252] R. Long, O. V. Prezhdo, Nano Lett. 2016, 16, 1996.

[253] C.-H. Lee, G. Lee, A. M. van der Zande, W. Chen, Y. Li, M. Han, Cui, G. Arefe, C. Nuckolls, T. F. Heinz, J. Guo, J. Hone, P. Kim, Nat. Nanotechnol. 2014, 9, 676.

[254] M. M. Furchi, A. Pospischil, F. Libisch, J. Burgdörfer, T. Mueller, Nano

Lett. 2014, 14, 4785.

[255] R. Cheng, D. Li, H. Zhou, C. Wang, A. Yin, S. Jiang, Y. Liu, Y. Chen, Huang, X. Duan, Nano Lett. 2014, 14, 5590.

[256] G.-H. Lee, C.-H. Lee, A. M. van der Zande, M. Han, X. Cui, G. Arefe, C. Nuckolls, T. F. Heinz, J. Hone, P. Kim, APL Mater. 2014, 2, 092511.

[257] N. Huo, J. Kang, Z. Wei, S.-S. Li, J. Li, S.-H. Wei, Adv. Funct. Mater. 2014, 24, 7025.

[258] Y. Xue, Y. Zhang, Y. Liu, H. Liu, J. Song, J. Sophia, J. Liu, Z. Xu, Q. Xu, Z. Wang, J. Zheng, Y. Liu, S. Li, Q. Bao, ACS Nano 2016, 10, 573.

[259] N. Huo, J. Yang, L. Huang, Z. Wei, S.-S. Li, S.-H. Wei, J. Li, Small 2015, 11, 5430.

[260] N. Flöry, A. Jain, P. Bharadwaj, M. Parzefall, T. Taniguchi, K. Watanabe, L. Novotny, Appl. Phys. Lett. 2015, 107, 123106.

[261] A. Pezeshki, S. H. H. Shokouh, T. Nazari, K. Oh, S. Im, Adv. Mater. 2016, 28, 3216.

[262] I. G. Lezama, A. Arora, A. Ubaldini, C. Barreteau, E. Giannini, M. Potemski, A. F. Morpurgo, Nano Lett. 2015, 15, 2336.

[263] M. Long, E. Liu, P. Wang, A. Gao, H. Xia, W. Luo, B. Wang, J. Zeng, Y. Fu, K. Xu, W. Zhou, Y. Lv, S. Yao, M. Lu, Y. Chen, Z. Ni, Y. You, X. Zhang, S. Qin, Y. Shi, W. Hu, D. Xing, F. Miao, Nano Lett. 2016, 16, 2254.

[264] Y. Deng, Z. Luo, N. J. Conrad, H. Liu, Y. Gong, S. Najmaei, P. M. Ajayan, J. Lou, X. Xu, P. D. Ye, ACS Nano 2014, 8, 8292.

[265] T. Hong, B. Chamlagain, T. Wang, H.-J. Chuang, Z. Zhou, Y. Xu, Nanoscale 2015, 7, 18537.

[266] L. Ye, H. Li, Z. Chen, J. Xu, ACS Photonics 2016, 3, 692.

[267] S. Chuang, R. Kapadia, H. Fang, T. Chia Chang, W.-C. Yen, Y.-L. Chueh, A. Javey, Appl. Phys. Lett. 2013, 102, 242101.

[268] J.-H. Ahn, M.-J. Lee, H. Heo, J. H. Sung, K. Kim, H. Hwang, M.-H. Jo, Nano Lett. 2015, 15, 3703.

[269] S. Yang, C. Wang, C. Ataca, Y. Li, H. Chen, H. Cai, A. Suslu, J. C. Grossman, C. Jiang, Q. Liu, S. Tongay, ACS Appl. Mater. Inter- faces 2016, 8, 2533.

[270] D. He, Y. Pan, H. Nan, S. Gu, Z. Yang, B. Wu, X. Luo, B. Xu, Y. Zhang, Y. Li, Z. Ni, B. Wang, J. Zhu, Y. Chai, Y. Shi, X. Wang, Appl. Phys. Lett. 2015, 107, 183103.

[271] H.-C. Cheng, G. Wang, D. Li, Q. He, A. Yin, Y. Liu, H. Wu, M. Ding, Y. Huang, X. Duan, Nano Lett. 2016, 16, 367.

[272] X. Hu, X. Zhang, L. Liang, J. Bao, S. Li, W. Yang, Y. Xie, Adv. Funct.

Mater. 2014, 24, 7373.

[273] Y. Guo, C. Liu, H. Tanaka, E. Nakamura, J. Phys. Chem. Lett. 2015, 6, 535.

[274] X. Duan, C. Wang, J. C. Shaw, R. Cheng, Y. Chen, H. Li, X. Wu, Y. Tang, Q. Zhang, A. Pan, J. Jiang, R. Yu, Y. Huang, X. Duan, Nat. Nanotechnol. 2014, 9, 1024.

[275] C. Huang, S. Wu, A. M. Sanchez, J. J. P. Peters, R. Beanland, J. S. Ross, P. Rivera, W. Yao, D. H. Cobden, X. Xu, Nat. Mater. 2014, 13, 1096.

[276] Y. Gong, J. Lin, X. Wang, G. Shi, S. Lei, Z. Lin, X. Zou, G. Ye, R. Vajtai, B. I. Yakobson, H. Terrones, M. Terrones, B. K. Tay, J. Lou, S. T. Pantelides, Z. Liu, W. Zhou, P. M. Ajayan, Nat. Mater. 2014, 13, 1135.

[277] M.-Y. Li, Y. Shi, C.-C. Cheng, L.-S. Lu, Y.-C. Lin, H.-L. Tang, M.-L. Tsai, C.-W. Chu, K.-H. Wei, J.-H. He, W.-H. Chang, K. Suenaga, L.-J. Li, Science 2015, 349, 524.

[278] Y. Gong, S. Lei, G. Ye, B. Li, Y. He, K. Keyshar, X. Zhang, Q. Wang, J. Lou, Z. Liu, R. Vajtai, W. Zhou, P. M. Ajayan, Nano Lett. 2015, 15, 6135.

[279] W. Feng, W. Zheng, X. Chen, G. Liu, W. Cao, P. Hu, Chem. Mater. 2015, 27, 983.

[280] H.-M. Li, D. Lee, D. Qu, X. Liu, J. Ryu, A. Seabaugh, W. J. Yoo, Nat. Commun. 2015, 6, 6564.

[281] Y. Jin, D. H. Keum, S.-J. An, J. Kim, H. S. Lee, Y. H. Lee, Adv. Mater. 2015, 27, 5534.

[282] M. S. Choi, D. Qu, D. Lee, X. Liu, K. Watanabe, T. Taniguchi, W. J. Yoo, ACS Nano 2014, 8, 9332.

[283] X. Yu, S. Zhang, H. Zeng, Q. J. Wang, Nano Energy 2016, 25, 34.

[284] M.-L. Tsai, S.-H. Su, J.-K. Chang, D.-S. Tsai, C.-H. Chen, C.-I. Wu, L.-J. Li, L.-J. Chen, J.-H. He, ACS Nano 2014, 8, 8317.

[285] O. Lopez-Sanchez, E. Alarcon Llado, V. Koman, A. Fontcuberta i Morral, A. Radenovic, A. Kis, ACS Nano 2014, 8, 3042.

[286] Y. Li, C.-Y. Xu, J.-Y. Wang, L. Zhen, Sci. Rep. 2014, 4, 7186.

[287] L. Hao, Y. Liu, W. Gao, Z. Han, Q. Xue, H. Zeng, Z. Wu, J. Zhu, W. Zhang, J. Appl. Phys. 2015, 117, 114502.

[288] L. Wang, J. Jie, Z. Shao, Q. Zhang, X. Zhang, Y. Wang, Z. Sun, S.-T. Lee, Adv. Funct. Mater. 2015, 25, 2910.

[289] Y. Zhang, Y. Yu, L. Mi, H. Wang, Z. Zhu, Q. Wu, Y. Zhang, Y. Jiang, Small 2016, 12, 1062.

[290] B. Li, G. Shi, S. Lei, Y. He, W. Gao, Y. Gong, G. Ye, W. Zhou, K. Keyshar, J. Hao, P. Dong, L. Ge, J. Lou, J. Kono, R. Vajtai, P. M. Ajayan, Nano Lett. 2015, 15, 5919.

[291] X. Yuan, L. Tang, S. Liu, P. Wang, Z. Chen, C. Zhang, Y. Liu, W. Wang, Y. Zou, C. Liu, N. Guo, J. Zou, P. Zhou, W. Hu, F. Xiu, Nano Lett. 2015, 15, 3571.

[292] S. Liu, X. Yuan, P. Wang, Z.-G. Chen, L. Tang, E. Zhang, C. Zhang, Y. Liu, W. Wang, C. Liu, C. Chen, J. Zou, W. Hu, F. Xiu, ACS Nano 2015, 9, 8592.

[293] H. Zhang, X. Zhang, C. Liu, S.-T. Lee, J. Jie, ACS Nano 2016, 10, 5113.

[294] D. Li, R. Cheng, H. Zhou, C. Wang, A. Yin, Y. Chen, N. O. Weiss, Y. Huang, X. Duan, Nat. Commun. 2015, 6, 7509.

[295] P. Gehring, R. Urcuyo, D. L. Duong, M. Burghard, K. Kern, Appl. Phys. Lett. 2015, 106, 233110.

[296] Z. Xu, S. Lin, X. Li, S. Zhang, Z. Wu, W. Xu, Y. Lu, S. Xu, Nano Energy 2016, 23, 89.

[297] F. Xue, L. Chen, J. Chen, J. Liu, L. Wang, M. Chen, Y. Pang, X. Yang, G. Gao, J. Zhai, Z. L. Wang, Adv. Mater. 2016, 28, 3391.

[298] S. Vélez, D. Ciudad, J. Island, M. Buscema, O. Txoperena, S. Parui, G. A. Steele, F. Casanova, H. S. J. van der Zant, A. Castellanos- Gomez, L. E. Hueso, Nanoscale 2015, 7, 15442.

[299] F. Liu, W. L. Chow, X. He, P. Hu, S. Zheng, X. Wang, J. Zhou, Q. Fu, W. Fu, P. Yu, Q. Zeng, H. J. Fan, B. K. Tay, C. Kloc, Z. Liu, Adv. Funct. Mater. 2015, 25, 5865.

[300] M. Fontana, T. Deppe, A. K. Boyd, M. Rinzan, A. Y. Liu, M. Paranjape, P. Barbara, Sci. Rep. 2013, 3, 1634.

[301] H. Jeong, H. M. Oh, S. Bang, H. J. Jeong, S.-J. An, G. H. Han, H. Kim, S. J. Yun, K. K. Kim, J. C. Park, Y. H. Lee, G. Lerondel, M. S. Jeong, Nano Lett. 2016, 16, 1858.

[302] D. Jariwala, V. K. Sangwan, C.-C. Wu, P. L. Prabhumirashi, M. L. Geier, T. J. Marks, L. J. Lauhon, M. C. Hersam, Proc. Natl. Acad. Sci. 2013, 110, 18076.

[303] K. H. Lee, T.-H. Kim, H.-J. Shin, S.-W. Kim, Adv. Mater. 2016, 28, 1793.

[304] J. Lin, H. Li, H. Zhang, W. Chen, Appl. Phys. Lett. 2013, 102, 203109.

[305] J. Miao, W. Hu, Y. Jing, W. Luo, L. Liao, A. Pan, S. Wu, J. Cheng, X. Chen, W. Lu, Small 2015, 11, 2392.

[306] A. Sobhani, A. Lauchner, S. Najmaei, C. Ayala-Orozco, F. Wen, J. Lou, N. J. Halas, Appl. Phys. Lett. 2014, 104, 031112.

[307] S. Najmaei, A. Mlayah, A. Arbouet, C. Girard, J. Léotin, J. Lou, ACS Nano 2014, 8, 12682.

[308] T. Hong, B. Chamlagain, S. Hu, S. M. Weiss, Z. Zhou, Y.-Q. Xu, ACS Nano 2015, 9, 5357.

[309] W. Wang, A. Klots, D. Prasai, Y. Yang, K. I. Bolotin, J. Valentine, Nano Lett. 2015, 15, 7440.

[310] H. Li, Y. Anugrah, S. J. Koester, M. Li, Appl. Phys. Lett. 2012, 101.

[311] X. Gan, R.-J. Shiue, Y. Gao, I. Meric, T. F. Heinz, K. Shepard, J. Hone, S. Assefa, D. Englund, Nat. Photonics 2013, 7, 883.

[312] X. Wang, Z. Cheng, K. Xu, H. K. Tsang, J.-B. Xu, Nat. Photonics 2013, 7, 888.

[313] N. Youngblood, C. Chen, S. J. Koester, M. Li, Nat. Photonics 2015, 9, 249.

[314] X. Liu, T. Galfsky, Z. Sun, F. Xia, E. Lin, Nat. Photonics 2015, 9, 30.

[315] S. Wu, S. Buckley, A. M. Jones, J. S. Ross, N. J. Ghimire, J. Yan, D. G. Mandrus, W. Yao, F. Hatami, J. Vuckovic, A. Majumdar, X. Xu, 2D Mater. 2014, 1, 011001.

[316] S. Wu, S. Buckley, J. R. Schaibley, L. Feng, J. Yan, D. G. Mandrus, F. Hatami, W. Yao, J. Vucˇkovic´, A. Majumdar, X. Xu, Nature 2015, 520, 69.

[317] S. Schwarz, S. Dufferwiel, P. M. Walker, F. Withers, A. A. P. Trichet, M. Sich, F. Li, E. A. Chekhovich, D. N. Borisenko, N. N. Kolesnikov, K. S. Novoselov, M. S. Skolnick, J. M. Smith, D. N. Krizhanovskii, A. I. Tartakovskii, Nano Lett. 2014, 14, 7003.